Near-Field Dispersion of a Turbidity Current on a Slope

The Influence of a Gentle Slope on the Near-Field Sideways Dispersion of a Turbidity Current Generated during Deep-Sea Mining Operations

A. Visser

Delft University of Technology

Allseas Engineering B.V.

Near-Field Dispersion of a Turbidity Current on a Slope

The Influence of a Gentle Slope on the Near-Field Sideways Dispersion of a Turbidity Current Generated during Deep-Sea Mining Operations

by

A. Visser

to obtain a degree of Master of Science
at the Delft University of Technology.

Student Number	4667913	
Graduation Duration	November, 2023 - November, 2024	
Faculty	ME, TU Delft	
Thesis committee	Dr.ir. R.L.J. Helmons (chair),	(TU Delft)
	Dr.ir. G.H. Keetels,	(TU Delft)
	Ir. S.A. Wahab,	(TU Delft)
	Ir. B.K. Blankenaar,	(Allseas)
	Ir. F. van Grunsven,	(Allseas)

Style	Modified TU Delft Report Style
Language Check	Grammarly and ChatGPT [14, 29]

This thesis is confidential and cannot be made public until November 20, 2024.
An electronic version of this thesis is available at the TU Delft repository.

Preface

This thesis marks the end of my Master of Science in Offshore and Dredging Engineering at the Delft University of Technology. This report describes my findings through experiments on the influence of a sloping bed on plume dispersion during deep-sea mining operations.

First of all, I would like to thank my supervisors at the TU Delft, Dr.ir. Rudy Helmons and Ir. Shaheen Wahab, for the support and advice that they have given me during the many meetings and discussion sessions and for their help and patience during my time in the lab. I also want to thank Ed Stok, Andre van den Bosch and Huib Zuurmond for their advice and for helping me build the experimental setup and perform the experiments.

I also want to sincerely thank my supervisors at Allseas, Ir. Britt Blankenaar and Ir. Frans van Grunsven, for sharing their knowledge and devoting their time to in-depth discussions, as well as providing a motivating and fun working place whenever I was not in the laboratory.

Lastly, I gratefully and sincerely would like to thank my family, my dear friends and my roommates from Kings on Queens (KonQ) for their support, discussions and proofreading.

A. Visser
Delft, November 2024

Summary

This research investigates how slope angles and directions affect the near-field dispersion of turbidity currents discharged from a moving source during deep-sea mining (DSM). The study focuses on the Clarion-Clipperton Zone (CCZ), rich in polymetallic nodules. Sediment plumes from nodule collection can negatively impact marine ecosystems and hinder mining operations. Previous studies have mainly researched the dispersion of turbidity currents on flat surfaces, discharged from a stationary source, creating a knowledge gap regarding how slopes influence the dispersion of a turbidity current, when discharged from a moving source. This research addresses this gap by examining this to improve environmental impact assessments and optimize nodule collection methods.

Experiments were conducted at TU Delft's offshore and dredging laboratory using a modular flume tank with an experimental setup scaled at 1:20. The setup included a moving cart and diffuser system on a sloping seabed, with precise control over slope angles and velocity ratio. Glass beads, used instead of CCZ sediment, were suspended in a mixing tank and discharged into the flume to simulate a turbidity current. Measurement techniques involved the acoustic Doppler velocimeter (ADV) and ultrasonic velocity profiler (UVP) sensors for mixture concentration and velocity data, complemented by multi-angle camera footage for visual analysis. Various slope angles (-5° to 5°) and velocity ratios (source velocity over discharge velocity, $\zeta = 1.00$ and 1.25) were tested to observe their effects on the behaviour of a turbidity current, with device calibration and consistent experimental parameters ensuring accurate and comparable results.

A notable phenomenon is observed during the experiments, namely the formation of a bulge directed towards the diffuser. A higher velocity ratio and steeper slopes led to more significant bulges, with the bulge length and impingement angle increasing with slope steepness. Regarding velocity ratios, higher ratios resulted in larger dispersion angles and larger turbidity current heights in downhill driving experiments, while uphill conditions showed an inverse trend. The slope angles influence the dispersion by reducing the dispersion angle for steeper slopes in downhill driving experiments, with inconsistent results for uphill conditions. Data analysis from the UVP, camera footage, and concentration measurements supported these findings.

Future research should focus on identifying parameter ranges for floating plumes, investigating bulge formation further, assessing the influence of the concentration on the dispersion of a turbidity current, conducting experiments with reduced source velocities, scaling down experiments, and using real CCZ sediment in saltwater. For full-scale deep-sea mining, equalising source and discharge velocities ($\zeta = 1$) is recommended to mitigate floating plumes and bulge formation (as much as possible). Additionally, path planning should avoid slopes steeper than -3° to prevent excessive bulge formation and auto-suspension of sediment.

Contents

List of Figures

List of Tables

Nomenclature

Abbreviations

Abbreviation	Definition
ADV	Acoustic Doppler Velocimeter
APEI	Area of Particular Environmental Interest
BM	Box Model
CCZ	Clarion-Clipperton Zone
DNC	Deep-sea Nodule Collection
DNS	Direct Numerical Simulation
DSM	Deep-Sea Mining
FPS	Frame rate Per Second
ISA	International Seabed Authority
KonQ	Kings on Queens
MBES	MultiBeam EchoSounder
PNMT	Polymetallic Nodule Mining Tool
PSD	Particle Size Distribution
PSV	Production Support Vessel
SMT	Seabed Mining Tool
SNR	Signal to Noise Ratio
SWE	Shallow-Water Equations
TUD	Technical University Delft
UV	UltraViolet
UVP	Ultrasonic Velocity Profiling
VTS	Vertical Transport System

Symbols

Symbol	Definition	Unit
B_o	Buoyancy flux	$[\frac{m^3}{kg}]$
C	Speed of sound	$[\frac{m}{s}]$
c	Concentration	$[\frac{g}{L}]$
c_{vs}	Volume concentration	[-]
d	Particle diameter	$[m]$
d_f	Fractal dimension	[-]
E_b	Breakage coefficient	[-]
f	Coriolis parameter	$[Hz]$
f_d	Doppler frequency shift	$[Hz]$
f_s	Stationary frequency	$[Hz]$
Fr	Froude number	[-]
g	Gravitational acceleration	$[\frac{m}{s^2}]$
g'	Reduced gravity	$[\frac{m}{s^2}]$
H	Diffuser height	$[m]$
h	Flow depth	$[m]$
h_d	Height of the diffuser above the table	$[m]$
L	Length	$[m]$

Symbol	Definition	Unit
L_r	Length in reality	$[m]$
L_s	Source length	$[m]$
$L_{s,B}$	Boussinesq source length	$[m]$
L_j	Jet length	$[m]$
$L_{j,B}$	Boussinesq jet length	$[m]$
L_m	Length in the model	$[m]$
$M_{o,B}$	Boussinesq momentum flux	$[\frac{N \cdot s}{m^2 \cdot s}]$
M_o	Momentum flux	$[\frac{N \cdot s}{m^2 \cdot s}]$
P	Rouse number	[-]
Q_o	Volume flux	$[\frac{m^3}{s \cdot m^2}]$
R_{sd}	Relative submerged density of a particle	[-]
Re	Reynolds number	[-]
Ri	Richardson number	[-]
Ro	Rossby number	[-]
t	Time	$[s]$
$\bar{u}$	Depth-average velocity	$[\frac{m}{s}]$
u_*	Shear velocity	$[\frac{m}{s}]$
u_0	Representative velocity	$[\frac{m}{s}]$
u_p	Vertical bed slope velocity	$[\frac{m}{s}]$
v	Molecular kinematic viscosity	$[\frac{m^2}{s}]$
v_d	Discharge velocity	$[\frac{m}{s}]$
v_d*	Relative discharge velocity	$[\frac{m}{s}]$
v_{rel}	Relative velocity between transmitter and receiver	$[\frac{m}{s}]$
v_s	Source velocity	$[\frac{m}{s}]$
v_t	Settling velocity	$[\frac{m}{s}]$
$v_{t,Bud}$	Settling velocity according to Budryck	$[\frac{mm}{s}]$
$v_{t,h}$	Hindered settling velocity	$[\frac{m}{s}]$
$v_{t,Rit}$	Settling velocity according to Rittinger	$[\frac{mm}{s}]$
$v_{t,St}$	Settling velocity according to stokes	$[\frac{mm}{s}]$
$v_{t,Za}$	Settling velocity according to Zanke	$[\frac{mm}{s}]$
α	Entrainment coefficient	[-]
α_s	Scaling factor	[-]
β	Hindered settling coefficient	[-]
$\Gamma_{o,B}$	Boussinesq flux balance parameter	[-]
Γ_o	Flux balance parameter	[-]
ζ	Source-to-discharge velocity ratio	[-]
θ	Latitude of the earth	[°]
κ	Von Karman constant	[-]
λ	Mixing length scale	[-]
ρ_l	Density of a liquid	$[\frac{kg}{m^3}]$
ρ_s	Density of a solid	$[\frac{kg}{m^3}]$
ω	Variance deviation	[%]
Ω	Rotational velocity of the earth	$[\frac{1}{s}]$

1 | Introduction

Governments worldwide commit themselves to a decarbonised energy mix by 2050. The renewable energy market is growing rapidly, partly due to the rising prices of fossil fuels, boosting the price-competitiveness of clean energy technologies [13, 38]. However, a low carbon economy is a materials economy, but the current supply of many critical materials falls short of keeping up with the required pace to comply with the commitment. Critical materials, including Cobalt (Co), Nickel (Ni), Tellurium (Te), Titanium (Ti), Platinum (Pt), and other rare earth metals, are geographically concentrated, increasing price and therefore scarcity [2, 13, 23, 37]. To avoid too much dependency on large suppliers, lower the pressure on land mining expansion and still meet the metal demand of the rapidly growing green economy, more companies turn their focus towards the deep-sea, where these critical metals are present in the form of nodules.

1.1. Deep-sea Mining

In this section, some background information is given on the matter of deep-sea mining (DSM). The nodule collection location is illustrated in Section 1.1.1 and the working principle is explained in Section 1.1.2.

1.1.1. The Clarion-Clipperton Zone

Location

The Clarion-Clipperton zone (CCZ) is located in the eastern part of the Pacific Ocean, just above the equator [21]. The CCZ is an area of approximately $4.5 * 10^6\ km^2$ and is known for its large stretched flat areas [61, 73]. The location is known for its high nodule abundance and is therefore chosen as an exploration and possible exploitation site for DSM [4, 41]. The CCZ is practically under the administration of the International Seabed Authority (ISA), they grant licenses for exploration and possibly for exploitation in the future (when there is a stronger regulatory framework for deep-sea nodule collection (DNC)) [8, 39]. The CCZ is divided into areas of approximately 75,000 km^2 by the ISA, on which states can apply for a license. These areas are shown in blocks in Figure 1.1, where some of these areas are reserved, shown in yellow, and some are licenced by different countries. In addition to that, the different areas of particular environmental interest (APEIs) can be seen. The ISA is working to finalize legislation on exploitation in the CCZ, since Nauru submitted an exploitation request, triggering the two-year timeline to finish elaborating the rules, regulations, and procedures related to exploitation. [8, 34].

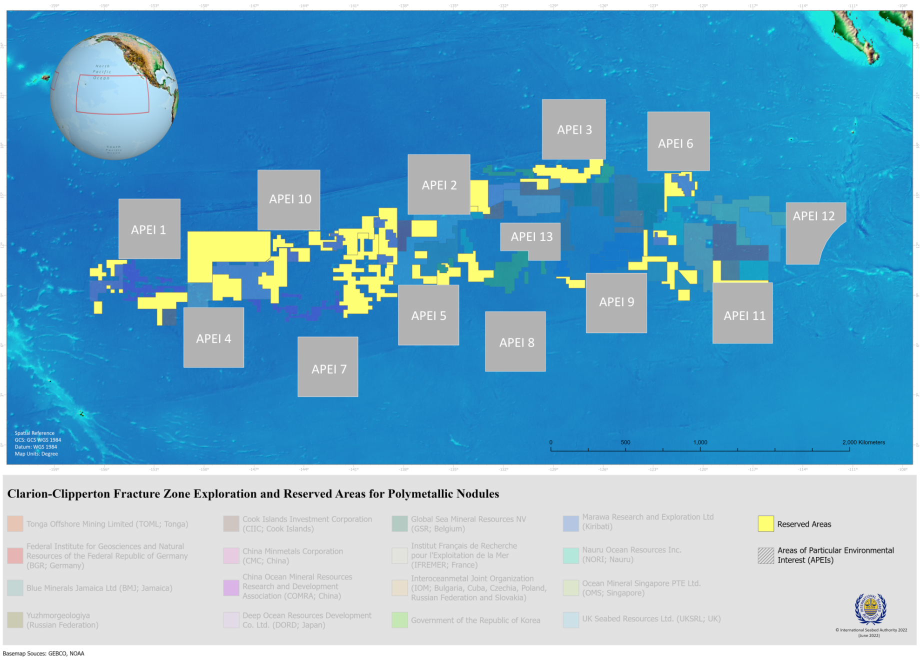

Figure 1.1: CCZ area with the different license areas and the APEIs [40]

Bathymetry

The CCZ is a vast area and therefore has a lot of different seabed throughout. The bathymetry of the CCZ has been extensively researched with multibeam echosounders (MBES), which are used to map most of the area [61, 73]. The average depth in the eastern CCZ is ~4600 m deepening to ~5200 m in the western CCZ [45]. The majority of the CCZ area consists of wide stretched plains with very gentle to no slopes ($< 3°$) with a nodule abundance of around 8-12 $\frac{kg}{m^2}$ [5, 61].

Zooming in on a specific area, APEI 6, as can be seen in Figure 1.2, it can be seen that even though the seabed looks flat, there is still some roughness. The local depth differences over a distance of 10 km can be up to 200 meters, meaning that there are slopes, abyssal hills and seamounts [5, 61].

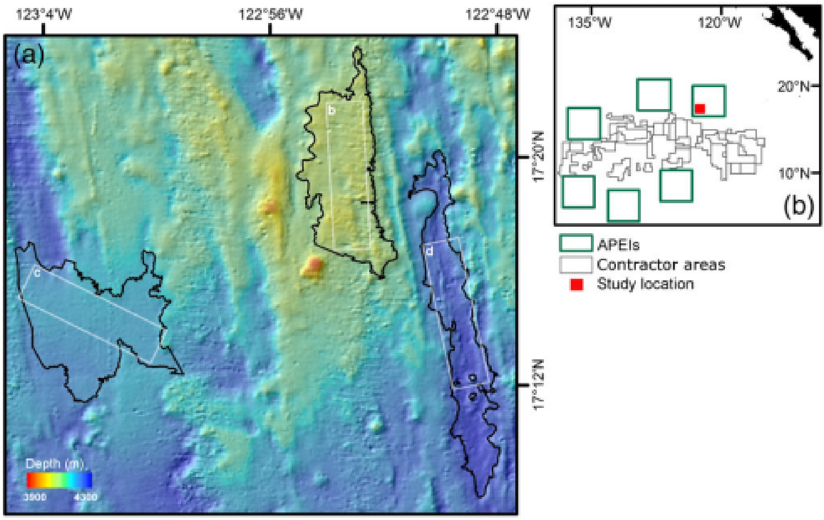

Figure 1.2: Study area within APEI 6 in the CCZ [74]

1.1.2. Working Principle

DSM can be applied to multiple resource areas, like polymetallic sulfides, cobalt-rich crusts and polymetallic nodules (or nodules in short) [52]. The latter distinguishes itself from the others, because no actual excavation is required to collect the nodules and is therefore indicated as DNC. DNC is challenging, combining multiple high-tech processes to collect polymetallic nodules from the seabed in the deep-sea as effectively and with the least environmental impact as possible. The process consists of three main components, namely the seabed mining tool (SMT) or polymetallic nodule mining tool (PNMT), the vertical transport system (VTS) and a production support vessel (PSV) [23, 72], which is depicted in Figure 1.3. In the figure, two types of VTS can be seen: air injection and lifting pump.

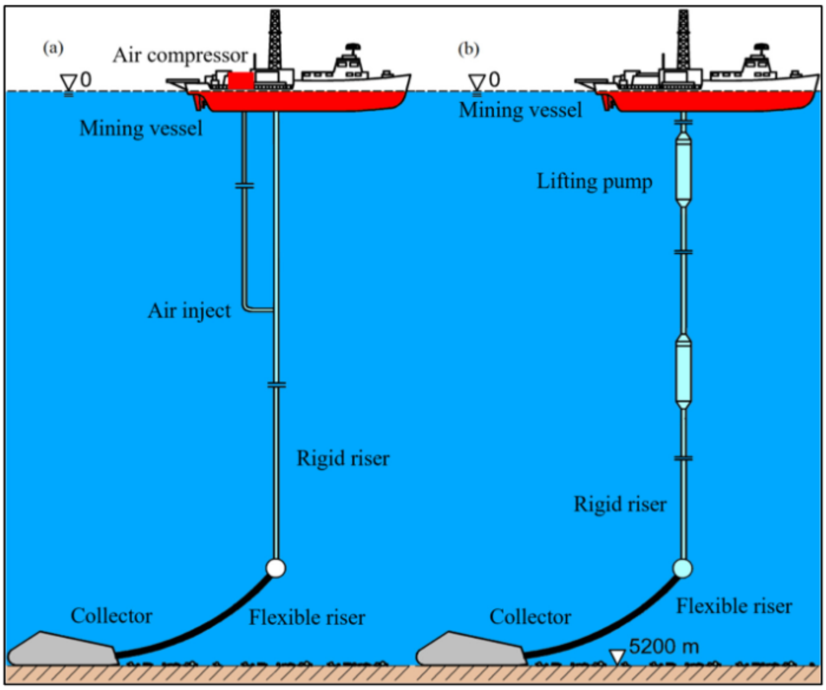

Figure 1.3: Deep-sea mining components [42]

The SMT is a nodule collection vehicle, driving over the seabed on tracks, with a typical velocity range of 0.25 up to 0.75 $\frac{m}{s}$, with a maximum of 1 $\frac{m}{s}$ [1, 2, 42]. The collector is either mechanically, hydraulically or, with a combination of both, hybrid [2]. At this moment, the focus lies mainly on a hydraulic collector, with a working principle depending on the Coandă effect, to collect the nodules [2]. The average nodule composition is 25-30 % manganese, 15 % iron, 0.6 - 1.4 % copper, 1 - 1.5 % nickel and 0.2 - 0.4 % cobalt [42, 60, 65] and they have a growth rate of several mm to several cm per million year [52].

1.2. Problem Statement

During the DNC process, not only nodules are collected, but also sediment. Most of the sediment and excess water after picking up is discharged through the diffuser of the collector, leaving a sediment plume in its wake. The sediment plume transforms into a turbidity current, flowing out over the seabed (Section 2.3) [33]. This results in several different impacts:

- Burial of organisms and change of top layer - The turbidity current deposits its sediment on the seabed, causing the burial of organisms and change of the top layer of the seabed, possibly reducing the pick-up efficiency of the DNC operation and thus reducing resource utilization.
- Spreading into APEIs - The spreading of the turbidity current might extend beyond the designated mining areas into the APEI areas, as depicted in Figure 1.2, which are designated to preserve marine life and habitats within the CCZ.
- Suffocate filter-feeders - The turbidity current will suffocate filter-feeders, as they are used to clear water and not a clay suspension [52].

Slopes might enhance all the effects as mentioned above by increasing the dispersion of the turbidity current and the turbulence within the turbidity current, increasing the erosion of the seabed and potentially affecting a larger area [30, 58, 69, 77].

1.3. Research Objective

The dispersion of a turbidity current on a flat seabed is not a new topic to literature and has already been experimentally researched by Vásquez (2020) [78] and numerically by Wells and Dorrell (2021) [79]. As described in Section 1.1.1, the CCZ also contains (gentle) slopes, which possibly have a negative influence on the dispersion of a turbidity current. The influence of a slope on the dispersion of a turbidity current is experimentally researched by Sequeiros *et al.* (2009) and Van Grunsven *et al.* (2018) [30, 69] and numerically by Steenhauer *et al.* (2017) and Ouillon *et al.* (2019) [58, 77]. However, DNC is no stationary process, the SMT is driving while discharging the sediment plume, meaning that the turbidity current has a moving source. The dispersion of a turbidity current on a flat surface discharged by a moving source has been experimentally researched by Van Pelt (2023) [63] and numerically by Blanchette (2022) and Ouillon *et al.* (2021) [9, 59]. The experimental setup from Van Pelt can be seen in Figure 1.4. However, the combination of having a slope and a moving source has not been experimentally researched before. The objective of this research is therefore:

*"Determine the influence of a **slope angle and slope direction** on the **near-field sideways dispersion of a turbidity current**, discharged from a **moving source**.*

This will be done by varying the slope angle and velocity ratio (ζ), calculated as per Equation (1.1).

$$\zeta = \frac{v_s}{v_d}, \tag{1.1}$$

where v_s is the source velocity and v_d is the discharge velocity.

Knowing the influence of a slope angle and direction on the spread of a turbidity current discharged from a moving source helps future research to make better assumptions and have more accurate (model) input on the matter. In addition to that, it is the next step in the direction of reducing the environmental impact of DNC and it also benefits resource utilization and DNC planning, because with the conclusions from this research, companies can better optimize the nodule collection from their contract areas and their collector path planning and both companies and legislators can make a more accurate impact assessment.

Furthermore, this research also taps into the environmental concerns on laying and trenching pipelines and dredging operations, where sediment plumes are generated due to operations that disturb the seabed.

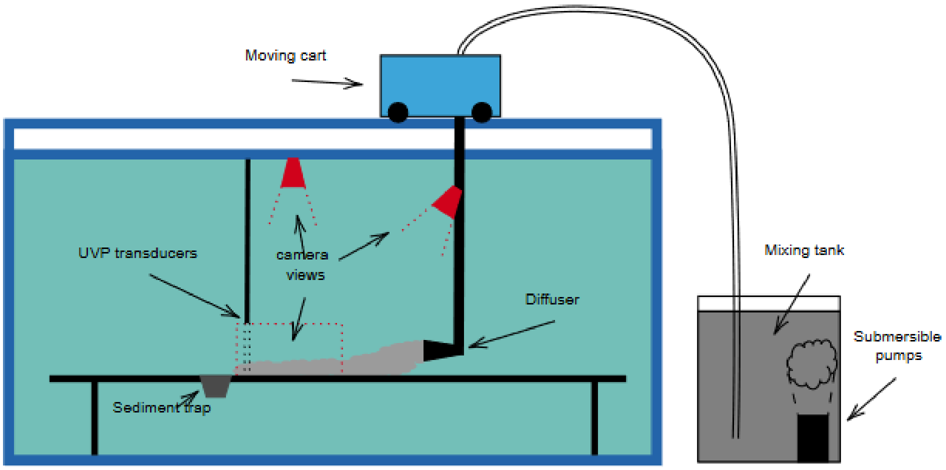

Figure 1.4: Schematic of experimental setup from Van Pelt [63]

1.4. Research Questions

To meet the objective of this research, the following research questions have been formulated:

- When do unwanted phenomena occur during the discharge or near-field dispersion of a turbidity current on a sloping seabed from a moving source?
- How will the ratio of source velocity over discharge velocity influence the near-field dispersion of a turbidity current on a slope?

Unwanted phenomena are defined as additional unfavorable conditions during the discharge of the sediment plume or propagation of the turbidity current that in reality would have negative effects on the impact of deep-sea mining or other subsea operations that generate sediment plumes.

By answering these research questions, a better understanding of the near-field dispersion of turbidity currents on a slope, discharged by a moving source, is achieved.

1.5. Research Methodology

The theoretical (literature) research will be done on the near-field dispersion of turbidity currents on a slope, discharged from a moving source, to find out how much information is available on the research subject, to see where the knowledge gap is and to sketch the research framework. The literature review results are described in Chapter 2.

The practical (experimental) research will take place in the offshore and dredging laboratory of the TU Delft. The experimental research should give results that confirm conclusions from the literature study and broaden the knowledge on the dispersion of turbidity currents. During the experiments, the near-field dispersion of the turbidity current will be measured while changing the slope angle, the concentration of the discharge mixture and the velocity ratio. The sediment flux will be constant throughout the research. The diffuser will remain parallel to the slope; thus, the diffuser angle follows the slope angle. The extensive experimental methodology will be described in Chapter 3, with the results in Chapter 4, analysis and discussion of those results in Chapter 5 and conclusions with recommendations in Chapter 6.

2 | Literature Review

In this chapter, the theoretical part of this research, the literature review, is described. Section 2.1 is about the sediment in the CCZ, Section 2.2 elaborates on the origin of the sediment plume, Section 2.3 describes the main characteristics of a turbidity current. Section 2.4 focuses on the relevant aspects of the experimental research and lastly, Section 2.5 gives hypotheses on the research questions, based on the literature research.

2.1. Sediment

In this paragraph, the properties of the soil are elaborated. Section 2.1.1 discusses the characteristics of the CCZ sediment. Section 2.1.2 describes the settling velocity of sediment in different flow regimes.

2.1.1. CCZ Sediment Characteristics

The CCZ classifies as deep-sea (abyssal plain), where most encountered sediments are usually a mixture of clay and silt. Most of this sediment already made a massive trip from distant land masses, through ocean currents or wind. Locally produced sediment originates from the weathering of oceanic rock or skeletal remains of mostly pelagic organisms composed of carbonate or silica. While it is expected to find a significant amount of coarse-grained bioclastic sediment, produced by the benthic megafauna, the sediment of the abyssal plane is predominantly very fine-grained, reflecting the sluggish bottom current regime [33]. The diameter ranges of the sediment fractions on the seabed of the CCZ are as per Table 2.1.

Table 2.1: Fraction distribution of sediment from the CCZ [24, 28, 33]

Name of Sediment Fraction	Diameter Range [μm]	GSR Data Average [%]
Clay	< 2	12.0
Silt	2-63	76.2
Sand	63-2000	11.8

2.1.2. Settling Velocity

The sediment that is suspended in the turbidity current has a certain settling velocity, which is influenced by sediment type and particle diameter. The settling velocity itself influences the suspension time and propagation of a turbidity current. More on turbidity currents in Section 2.3. The settling velocities are all calculated by using the relative submerged density of the sediment particle (R_{sd} [-]), which is calculated as per Equation (2.1) [51].

$$R_{sd} = \frac{\rho_s - \rho_l}{\rho_l}, \tag{2.1}$$

where ρ_s [$\frac{kg}{m^3}$] is the density of the solid (the sediment particle) and ρ_l [$\frac{kg}{m^3}$] is the density of the liquid (sea water).

For different flow regimes, different calculations for approaching the settling velocity have been used. Stokes for laminar settling, Budryck and Zanke for settling in the transition zone and Rittinger for turbulent settling. The regime of the flow is determined by Reynolds, who classified the flow regimes as per Table 2.2. A visualization of the settling velocity of individual particles in different flow regimes is given in Figure 2.1, where d [m] is the particle diameter.

- Laminar flow, d < 0.1 mm, according to Stokes, calculated as per Equation (2.2).

$$v_{t,St} = 424 \cdot R_{sd} \cdot d^2 \tag{2.2}$$

- Transitional flow, 0.1 mm < d < 1 mm, according to Budryck and Zanke, calculated as per Equation (2.3) and Equation (2.4).

$$v_{t,Bud} = 8.925 \cdot \frac{\sqrt{1 + 95 \cdot R_{sd} \cdot d^3} - 1}{d} \tag{2.3}$$

$$v_{t,Za} = \frac{10 * v_l}{d} \cdot (\sqrt{1 + \frac{R_{sd} \cdot g \cdot d^3}{100 \cdot v_l^2}} - 1) \tag{2.4}$$

- Turbulent flow, d > 1 mm, according to Rittinger, calculated as per Equation (2.5).

$$v_{t,Rit} = 87 \cdot \sqrt{R_{sd} \cdot d} \tag{2.5}$$

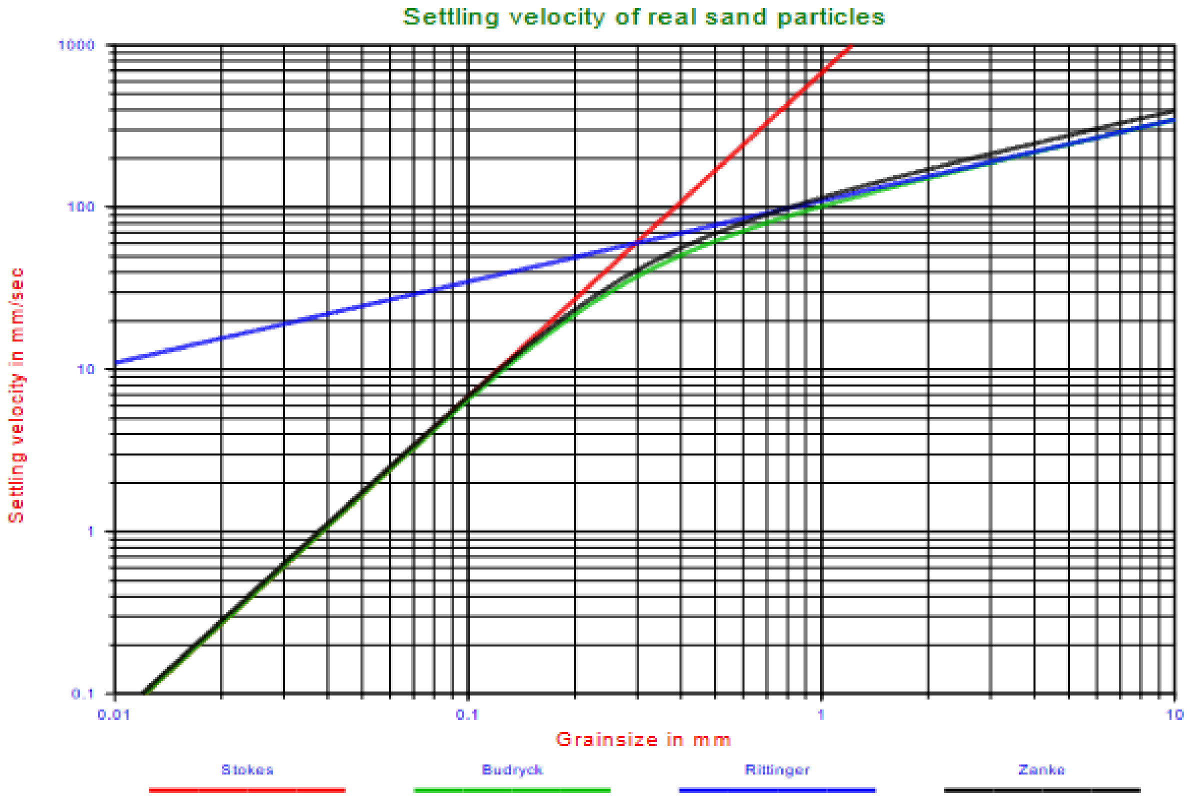

Figure 2.1: Settling velocity of individual particles [51]

In Equation (2.2) till Equation (2.5), the settling velocity is calculated for only an individual grain. This grain moves downward, while the same volume of water has to move upward. In a mixture, with many grains settling, this induces an average upward velocity of water and the collision of particles with one another, resulting in a decrease in settling velocity. This is often referred to as hindered settling [7, 51]. The ratio of the hindered settling velocity over the settling velocity can be calculated as per Equation (2.6). However, at very low concentrations, with a relatively low amount of individual grains, the average settling velocity will increase, because some of the grains will settle in each other's wake [51].

$$\frac{v_{t,h}}{v_t} = (1 - c_{vs})^{\beta}, \tag{2.6}$$

where c_{vs} is the volume concentration, between 0 and 0.3, and β is an analytically determined value by Richardson and Zaki (1954), between 2.39 and 4.65 [66].

Table 2.2: Flow regimes based on Reynolds number [80]

$0 < Re < 1$	Highly viscous laminar flow
$1 < Re < 100$	Laminar flow, strong Reynolds number dependence
$100 < Re < 10^3$	Laminar flow
$10^3 < Re < 10^4$	Transition from laminar to turbulent flow
$10^4 < Re < 10^6$	Turbulent flow, moderate Reynolds number dependence
$10^6 < Re < \infty$	Turbulent flow, slight Reynolds number dependence

2.1.3. Flocculation

Clay and other soil particles can adhere, forming larger aggregates, or groupings, increasing the effective particle diameter [3]. This phenomenon is known as flocculation. The fractal dimension (d_f) and the breakage coefficient (E_b) play a significant role in controlling the aggregation and break-up processes of flocculation, which is the result of doing experiments and numerical modeling of the particle size distribution (PSD) [23, 70]. Based on research from Gillard *et al.* (2019), the median particle size of a CCZ sediment mixture can increase, within 7 minutes, from 12 to 600 μm, significantly increasing the settling velocity (Section 2.1.2) [28]. Flocculation can be stimulated by flocculants, which can be both organic and inorganic.

The effects of flocculation can predominantly be observed in the far-field region, since the larger particles will settle as soon as the turbidity current subsides enough. The effects on the near-field region (Section 2.2) are limited to the immediate vicinity of the SMT. Overall, it is believed that flocculation is of great importance for reducing the impact of turbidity flows [23, 28].

2.2. Near-field Plume

This paragraph describes the region close to the discharge apparatus, the near-field region. Section 2.2.1 describes the controlling terms in the near-field region. Section 2.2.2 explains the impact area, where the plume collides with the seabed, also called the impingement area. Section 2.2.3 elaborates on the flux balance approach, used to classify discharged flows.

2.2.1. Governing Terms

The near-field region is defined as the region close to the SMT, mostly controlled by the discharge conditions [24, 25]. The sediment mixture that is discharged from the SMT through the diffuser has a certain velocity V_d. It is expected that the discharge velocity is (almost) equal to the source velocity V_s of the SMT, resulting in a velocity ratio $\zeta \approx 1$, calculated as per Equation (1.1). Since the outflow characteristics of a near-field plume (region 1 and 2 in Figure 2.2) are governed by the volume flux, momentum flux (Boussinesq and non-Boussinesq) and buoyancy flux [24, 26], calculated as per Equation (2.7) till Equation (2.10), in the case of $\zeta = 1$ the plume would not have a momentum-driven phase, as the relative velocity of the mixture with the ambient fluid would be zero [63].

$$Q_o = A \cdot v_d \tag{2.7}$$

$$M_{o,B} = Q_o \cdot v_d \tag{2.8}$$

$$M_o = Q_o \cdot v_d \cdot \rho \tag{2.9}$$

$$B_o = Q_o \cdot g', \tag{2.10}$$

where g′ is the reduced gravity, calculated as per Equation (2.11). In the Boussinesq approximation, which can be used in all non-isothermal flows, the relative density does not play a role, because it ignores the density difference of the heavy ambient fluid and the light ambient fluid [19], however The equations terms that are multiplied by gravity are not ignored, meaning that all density differences due to inertial effects are ignored and the approximation becomes only a function of temperature. For the non-Boussinesq approximation, a constant kinematic viscosity is assumed, meaning it can be used for both turbulent and laminar flows [75].

$$g' = \frac{g \cdot (\rho_0 - \rho_1)}{\rho_0} \tag{2.11}$$

The properties of the sediment plume immediately after being released from the collector vehicle are primarily controlled by inertial processes, such as turbulence induced by the discharge jet, or turbulence in the wake of the collector. At some distance behind the collector, however, these inertial processes will have dissipated and the diluted plume will be driven by its buoyancy. Design and operation choices determine the level of dilution of the plume at this transition from inertia to buoyancy-driven flow [59].

2.2.2. Impingement Area

The impingement area or region, also called impact area, is where the near-field plume collides with the seabed, leading to a wall-bounded flow [63]. Due to the direct interaction with the seabed, the negative buoyant plume disperses over the seabed. Both seabed erosion and sediment deposition are expected to take place in this area [24]. This area is depicted in Figure 2.2 as "3 - Impingement Region".

The impingement area is important, because it is the location where the turbidity current is initiated. At the impingement area, a lower volumetric suspended sediment leads to a shorter run-out distance of the turbidity current and therefore reduces the environmental impact [24]. In addition to that, it was also found by Elerian *et al.* (2021) by combining the models of Lee *et al.* (2013) and Parker *et al.* (1986) that the same goes for a smaller sediment flux. A smaller sediment flux at the impingement point results in a shorter run-out distance of a turbidity current and therefore has a lower environmental impact [24, 44, 62].

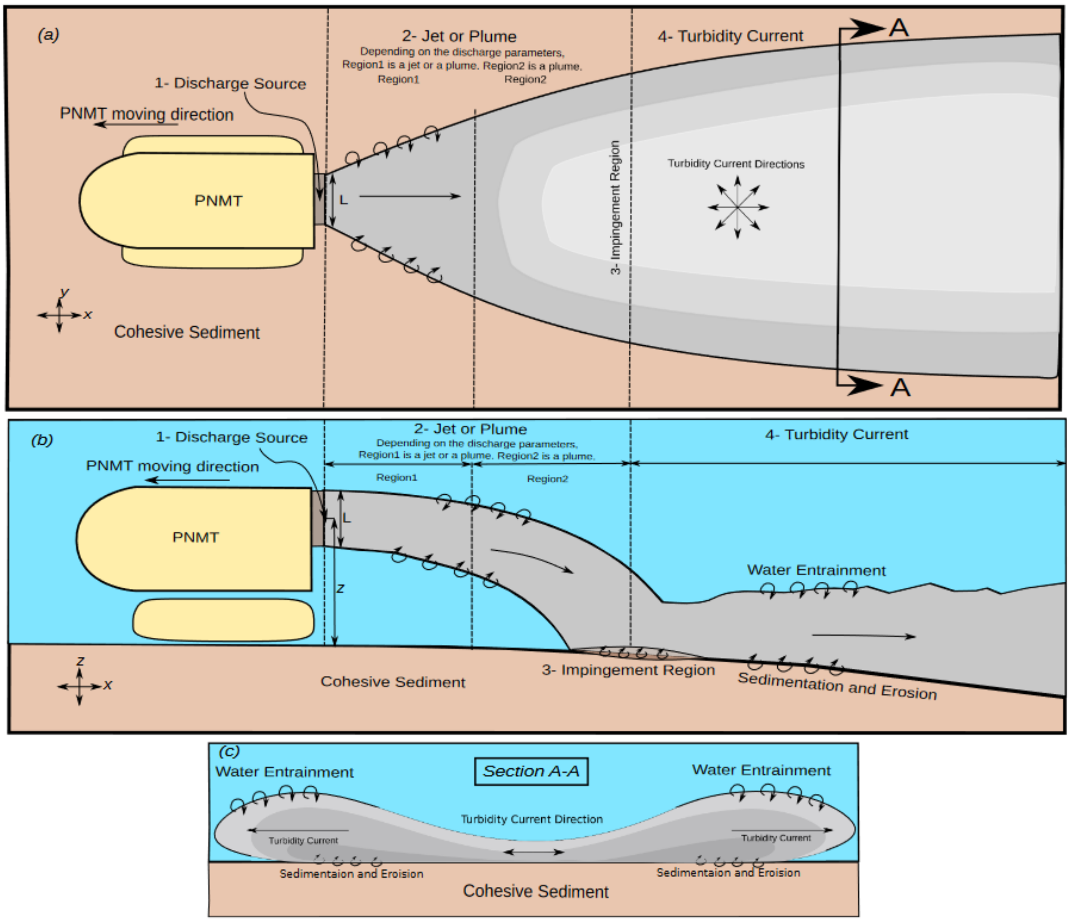

Figure 2.2: Evolution of a sediment-water mixture discharged from a PNMT. (a) Top view; (b) Side view; (c) Section A-A shows the direction of a turbidity current [22]

2.2.3. Flux Balance

The flux balance can be used to classify the discharged flow into different regimes, using the flux balance parameter Γ, defined as the ratio of buoyancy to inertia force [24, 53]. The flux balance parameter is calculated as per Equation (2.12) and Equation (2.13) [35].

$$\Gamma_{o,B} = \frac{5 \cdot B_o \cdot Q_o^2}{8 \cdot \alpha \cdot \sqrt{\pi} \cdot M_{B,o}^{5/2}}, \tag{2.12}$$

$$\Gamma_o = \frac{5 \cdot B_o \cdot Q_o^2}{8 \cdot \alpha \cdot \sqrt{\pi} \cdot M_o^{5/2}}, \tag{2.13}$$

where α is the entrainment coefficient, ranging from $0.10 < \alpha < 0.16$ for plumes and $0.065 < \alpha < 0.08$ for jets. The variations in α occur due to different experimental setups and the resulting error [11]. The different regimes are as per Table 2.3 [24, 48, 53, 54].

Table 2.3: Flux balance flow regimes [24]

$\Gamma = 0$	Pure jet	Remains jet until dissipation due to viscous diffusion
$0 < \Gamma < 1$	Forced plume	Buoyant jet, buoyancy forces dominant at discharge source [53]
$\Gamma = 1$	Pure plume	Momentum and buoyancy flux are equal at the discharge source [48]
$\Gamma > 1$	Lazy plume	Buoyancy forces dominant at discharge source [54]

In addition to the classification of discharged flow, the flux balance parameter is also introduced as a square ratio between source length L_s and jet length L_j, calculated as per Equation (2.14) [12, 24].

$$\Gamma_o = \frac{L_s}{L_j}^2, \tag{2.14}$$

where, for Boussinesq plumes L_j and L_s are calculated as per Equation (2.15) and Equation (2.16).

$$L_{j,B} = \frac{\sqrt{10} \cdot M_{B,o}^{3/4}}{3 \cdot \pi^{1/4} \cdot \alpha^{1/2} \cdot B_o^{1/2}}, \tag{2.15}$$

$$L_{s,B} = \frac{5 \cdot Q_o}{6 \cdot \sqrt{\pi} \cdot \alpha \cdot M_{B,o}^{1/2}}, \tag{2.16}$$

and for non-Boussinesq plumes calculated as per Equation (2.17) and Equation (2.18).

$$L_j = \frac{\sqrt{10} \cdot M_o^{3/4}}{3 \cdot \pi^{1/4} \cdot \alpha^{1/2} \cdot B_o^{1/2}}, \tag{2.17}$$

$$L_s = \frac{5 \cdot Q_o}{6 \cdot \sqrt{\pi} \cdot \alpha \cdot M_o^{1/2}}, \tag{2.18}$$

2.3. Turbidity Currents

This paragraph elaborates on turbidity currents. The sediment plume, a mixture of water and sediment, has a higher density than its ambient fluid, which results in it sinking quickly to the seabed. From there, it then will propagate as a turbidity current [33, 55], which is the dominant transport mechanism for particulate material across the floor of lakes and oceans [79]. Section 2.3.1 elaborates on the anatomy of a turbidity current and Section 2.3.2 describes the characteristics of a turbidity current. Section 2.3.3 gives the different dimensionless flow parameters that are used to describe the flow of a turbidity current. Section 2.3.5 describes the dispersion of a turbidity current on a flat surface. Section 2.3.6 describes the influence of a slope on the dispersion of a turbidity current and Section 2.3.7 describes the influence of a moving source on the dispersion of a turbidity current.

2.3.1. Anatomy

A turbidity current is generally divided into three parts: the head, body and tail, as can be seen in Figure 2.3. The head of the turbidity current in particular has different properties from the body and tail. Because the head displaces the ambient fluid, the concentration in the head is the highest, which results in friction resistance [24]. The shape of the head is related to the frictional drag imposed at the current boundary. For a smooth floor, a roughened floor or a sloping bottom, the shape of the head differs, where it has typically a thicker head on sloping bottoms [16, 31].

At the back of the head, near the body of the turbidity current, vortices start to take place, also called Kelvin-Helmholtz billows (as can be seen in Figure 2.3), due to the effect of velocity shear and turbulence in the ambient fluid. This results in a sharp discontinuity in the thickness of the current towards the body. The average velocity of the body has to be higher than the forward velocity of the head for the turbidity current to achieve a constant rate of advance [24].

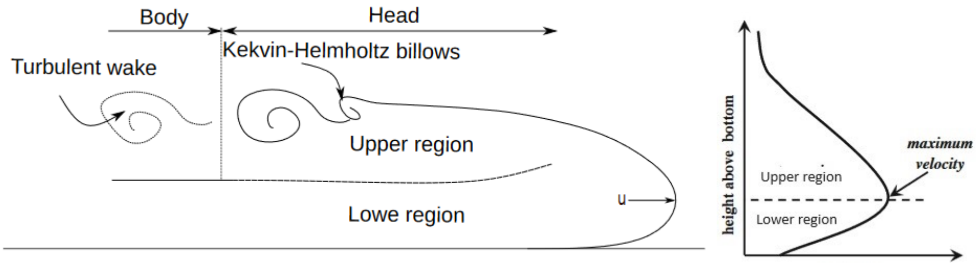

(a) Anatomy

(b) Velocity profile

Figure 2.3: Anatomy (a) and velocity profile (b) of a turbidity current [16, 50]

2.3.2. Characteristics

A turbidity current is a sediment-laden gravity current, with Newtonian rheology and turbulent state [71], and belongs to the family of density currents [79]. Turbidity currents differentiate themselves from density currents that are associated with temperature or salinity differences by the presence of sediment, which is usually held into suspension by the fluid turbulence [24, 69]. According to Bagnold (1962) and Shanmugam (2020), turbidity currents can typically only truly function as turbulent suspensions when the sediment concentration c is below 9%. This practically excludes turbidity currents with a relatively high density [6, 71], however, Elerian *et al.* (2021) states that turbidity currents can exist in both turbulent and laminar regimes [24].

When modeling the behavior of a turbidity current, it is important to consider the multiple particle size fractions and their interactions, like aggregation and the break-up processes. If this is not considered, an incorrect estimation of the particle settling velocity will be made, which plays an important role in determining the behavior of the turbidity current [23]. According to Elerian *et al.* (2023) and Helmons *et al.* (2022), studies from Ouillon (2021), based on DNS, and from Decrop (2019), CFD based on RANS, give a good basic understanding of the structure of a turbidity current in the near-field region, however they do not consider the multiple particle size fractions and their interactions [20, 23, 33, 59].

2.3.3. Dimensionless Flow Parameters

Dimensionless parameters form the foundation of understanding turbidity currents using physical or numerical experiments. The relevant dimensionless parameters include the densimetric Froude number (Fr), the Reynolds number (Re), the Rouse number (β) and the gradient Richardson number (Ri) [79]. An overview of all the dimensionless parameters can be seen in table 2.4.

Table 2.4: Dimensionless flow parameters [79]

Symbol	Name	Significance
Fr	Densimetric Froude number	Relative importance of inertial and density gravity forces
Re	Reynolds number	Turbulence in a gravity current
P	Rouse number	Settling velocity over shear velocity
Ri	Richardson number	Quantify the flow stability

Densimetric Froude Number

The densimetric Froude number is a parameter that determines the speed of propagation in turbidity currents, giving the relative importance of inertial and density gravity forces in terms of the influence of momentum and buoyancy flux [64, 79]. The densimetric Froude number is given by Equation (2.19).

$$Fr = \frac{\bar{u}}{\sqrt{g' \cdot h}}, \tag{2.19}$$

where $\bar{u}$ is the depth-average velocity and h the flow thickness. Flows on steeper slopes tend to have a $Fr > 1$, where wake turbulence dominates negative buoyancy, whereas flows on shallower slopes with rough beds tend to have $Fr < 1$, where buoyancy dominates [55, 79].

Reynolds Number

The Reynolds number is a dimensionless parameter, which holds a strong function for turbulence in a gravity current, calculated as per Equation (2.20).

$$Re = \frac{\bar{u} \cdot h}{\nu}, \tag{2.20}$$

where ν is the molecular kinematic viscosity of the fluid. In different flows, the Reynolds number describes the turbulence of a flow in a dimensionless parameter, meaning that different flows with equal Reynolds numbers are comparable in level of turbulence.

Rouse Number

The Rouse number defines the ratio of settling velocity over shear velocity, calculated as per Equation (2.21).

$$P = \frac{v_t}{\kappa \cdot u_* \cdot \lambda}, \tag{2.21}$$

where v_t is the settling velocity of particles in suspension, more in-depth explained in Section 2.1.2, κ the Von Karman constant, u_* the shear velocity and λ the dimensionless mixing length scale of the flow. When the value of P < 1, it is argued that the sediment is kept in suspension [79].

Richardson Number

The gradient Richardson number, consisting of the ratio of the buoyancy gradient to the shear, can be used to quantify the flow stability and is calculated as per Equation (2.22).

$$Ri = \frac{g' \cdot L}{u_0^2} \tag{2.22}$$

Notice that the Richardson number is practically the inverse of the Froude number squared. When $Ri > 1$ the flow is buoyancy dominated and when $Ri < 1$ the flow is momentum driven.

2.3.4. Seabed Effects

For a turbidity current to travel vast distances across the seafloor, sediment has to remain in constant suspension. This happens with turbulent mixing, a feedback loop known as auto-suspension. Auto-suspension is summarized by the Knapp-Bagnold criterion, where the available flow power per mass ($u_*{}^2\overline{u}$) must be greater than the work per mass ($gR\phi\omega_s h$) done to keep sediment in suspension and the depth-average viscous dissipation ($\epsilon_0 h$) [79], which can be seen in Equation (2.23).

$$u_*{}^2\overline{u} = gR\phi\omega_s h + \epsilon_0 h, \tag{2.23}$$

According to Wells and Dorrell (2021), the Knapp-Bagnold criterion precludes the persistence of auto-suspension. Auto-suspension is explained by self-acceleration, or ignition, where the turbidity current has the continued ability to entrain (settled) sediment from the seabed into suspension and to indefinitely thicken the flow through ambient fluid entrainment. However, Wells and Dorrell (2021) state that it does not explain the maintenance of the auto-suspension in turbidity currents on seabeds where the slopes, and thus the gravitational forces, are negligible [79].

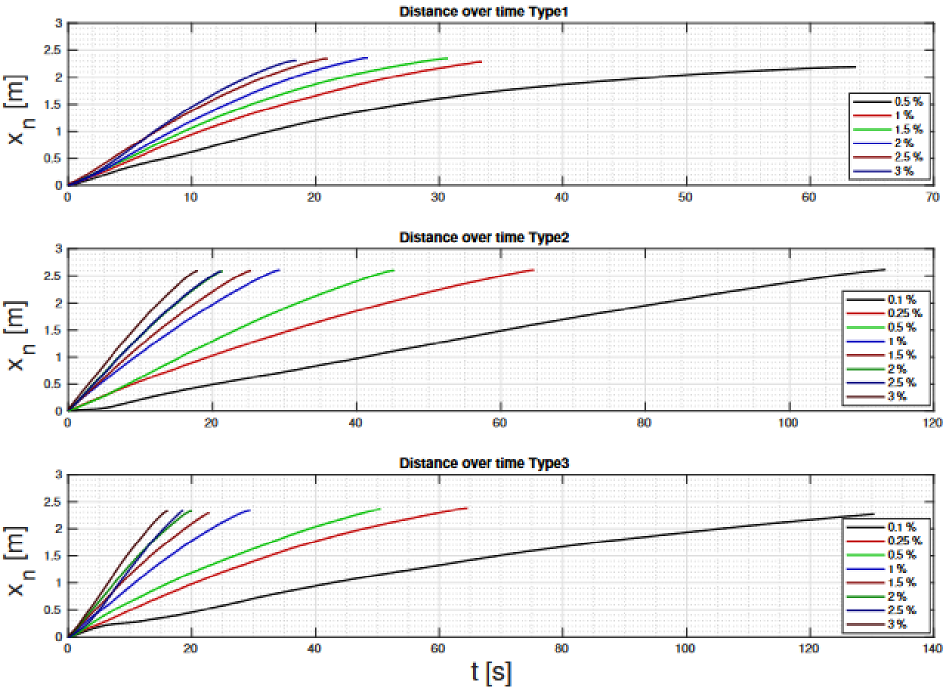

Figure 2.4: Front position of the turbidity $x_n[m]$ currents as a function of the propagation time $t[s]$ on a flat seabed [22]

2.3.5. Dispersion on a Flat Surface, Discharged from a Stationary Source

The propagation of a turbidity current in a lock exchange on a flat surface can be broken down into three different phases [36, 67]: the slumping phase, the self-similar phase and the viscous-buoyancy phase. In the first phase, the slumping phase, the head of the turbidity current is formed (as described in Section 2.3.1) and the propagation speed is constant due to the balance between the inertia and buoyant forces. In the second phase, the self-similar phase, the propagation speed is reduced, due to viscous forces disrupting the balance. At last, in the third phase, the viscous-buoyancy phase, the viscous forces dominate the flow and the turbidity current dies out [22].

There are parameters to influence the propagation distance and velocity of the turbidity current. In a flow with high-turbulence intensity, particles remain longer in suspension, because the gravity force on the particle cannot overcome the turbulence force anymore. This effect can be strengthened by increasing the initial concentration. In addition to that, Elerian *et al.* (2022) also found a positive correlation between the initial concentration and the front speed of the turbidity current, providing the current with more momentum [22]. In addition to that, the densimetric Froude number also has a positive relation to the front velocity [63]. The propagation of a turbidity current with three different sediment types and six different concentrations can be seen in Figure 2.4 [22]. Wijmans (2021) concludes that in the field, a higher volumetric concentration (> 1%) could prove beneficial in preventing the spatial spread of a turbidity current, due to a decreased momentum to buoyancy ratio, with a shorter distance to impingement and shorter distance after. A larger concentration does in turn result in a more aggressive impingement, resulting in higher velocities after impingement [81].

To predict the behaviour of a turbidity current and to minimize computational efforts, multiple drift-flux modeling approaches can be used. The model is composed mainly of a single mixture moment equation, a single mixture continuity equation and a single phase transport equation for each particle size fraction, where there is hardly any momentum exchange between the solid and liquid phase [22].

2.3.6. Dispersion on a Slope, Discharged from a Stationary Source

According to Dai (2023), a turbidity current down an inclined slope can be categorized into two different types, namely the ones supplied by a continuous buoyancy inflow and the ones generated by an instantaneous release of finite buoyancy [18]. The front location and front velocity plotted against time from this research can be seen in Figure 2.5.

Dai (2013) identified two different phases in turbidity current propagation: the acceleration phase

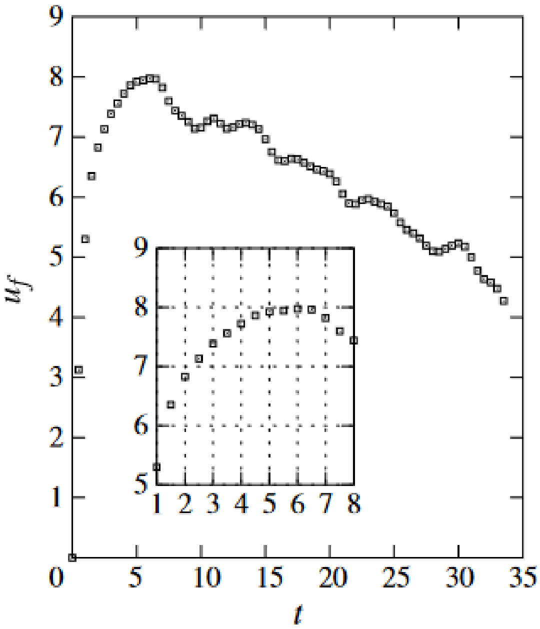

Figure 2.5: Front velocity $u_f[\frac{m}{s}]$ as a function of time $t[s]$ on a slope of 2° [18]

and the deceleration phase [18]. This is different from the phases that were identified by Huppert (1980) and Rottman (1983) as described in Section 2.3.5. However, these three different phases can be identified in Figure 2.5, where $t = 0 - 4s$ is the slumping phase (increasing front velocity), $t = 4 - 6.5s$ is the self-similar phase (constant front velocity) and $t = 6.5 - 35s$ is the viscous-buoyancy phase (decreasing front velocity). Dai (2013) defined the acceleration phase between $t = 0 - 6.5s$ and the deceleration phase from that time onwards. From the lock-exchange experiments for slopes of 0, 2, 6 and 9 °, it can be seen that the distinctive form of the current head quickly appears, as can be seen in Figure 2.6 [18]. In this figure, the time intervals are: for 0° (a-d) $t = 4.5, 12, 22, 30s$; for 2° (a-d) $t = 6.5, 12.5, 20, 36s$; for 6° (a-e) $t = 6, 10, 22, 26, 31.5s$; for 9° (a-d) $t = 7.5, 12, 18, 28s$.

From Figure 2.6 it can be seen that the head of the turbidity current is more streamlined at the gentle (0° and 2°) slopes than at the results from the steep (6° and 9°) slopes. The reason for this might be the absence of the large roller closer behind the head at the steeper slopes, which takes over the head in the deceleration phase, spreading the turbidity current on the slope, without violent mixing. This does not happen for the turbidity currents on the gentle slopes, because they propagate into the stage of motion where the viscous effect dominates [18, 22], which is in accordance with Elerian *et al.* (2022), described in Section 2.3.5. He *et al.* (2018) also found that the head becomes less streamlined and shorter at higher slope angles and also mentions turbulent billows at the upper interface of the current head, which can be interpreted as the large rollers as Dai (2013) calls it [18, 32].

Critical Angle

A turbidity current on a slope almost behaves like an avalanche. It erodes the surface and drags sediment particles along in its path, keeping itself in suspension for a longer period [49]. This is called auto-suspension, which states that when the vertical bed slope velocity is larger than the settling velocity of the sediment particle, the particles remain in suspension ($u_p \cdot sin(\theta) > v_t$) [82]. With a turbidity current in auto-suspension and a horizontal pressure difference, it is even possible that the turbidity current goes into auto-acceleration [69]. At the point where the particle suspension is equal to the particle deposition, the bed slope is its critical angle. If this slope angle is exceeded, the turbidity current is kept in auto-suspension, meaning that the excess density does not deplete and the current does not 'die' [27].

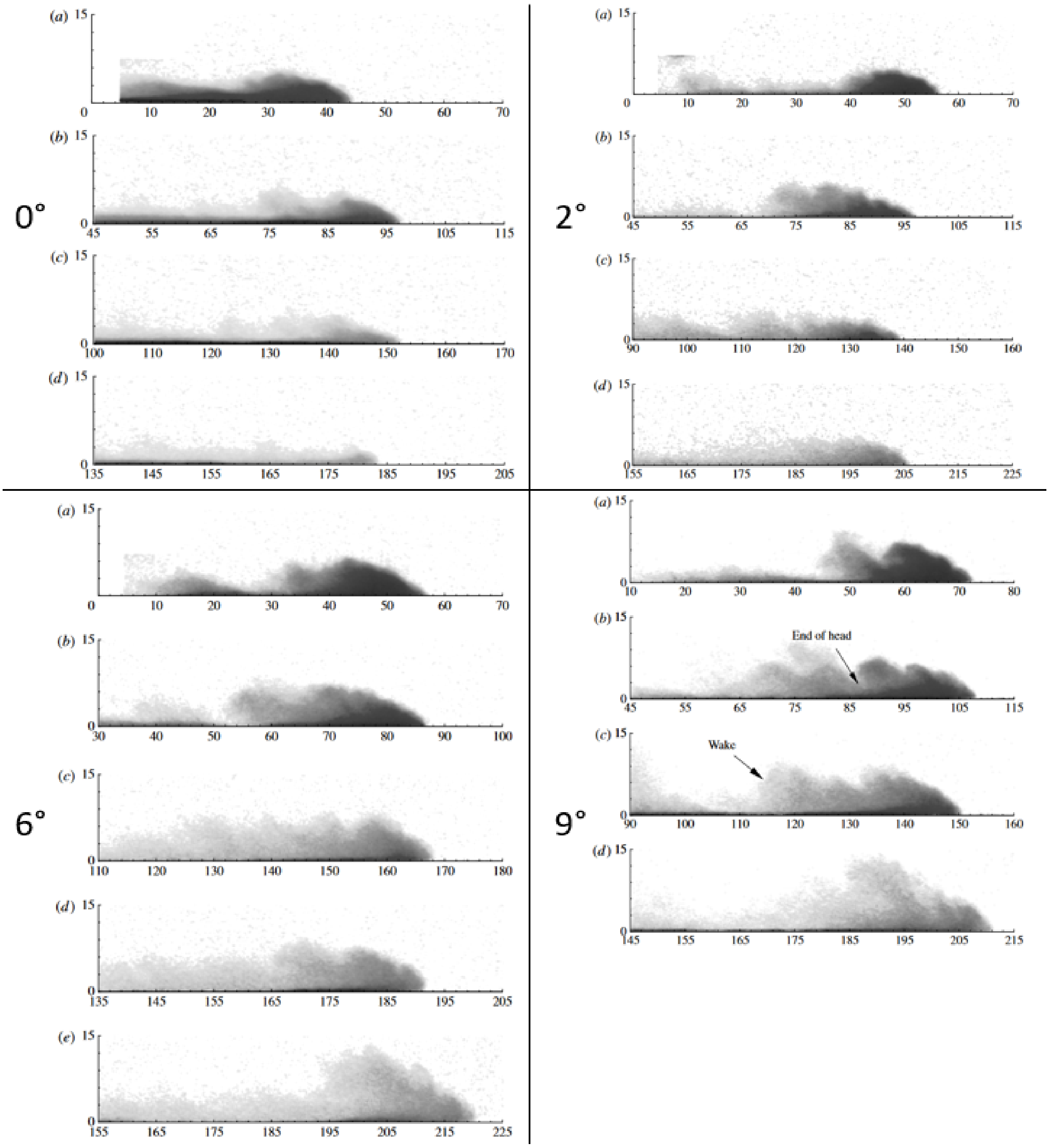

Figure 2.6: Fluid density images for turbidity currents at slopes of 0, 2, 6 and 9° [18]

2.3.7. Dispersion on a Flat Surface, Discharged from a Moving Source

Besides the influence of the bathymetry, it also has been researched what the influence of a moving source on the dispersion of a turbidity current is. To gain insight into this, Ouillon *et al.* (2021) conducted the first investigation of a gravity current continuously released from a moving source using direct numerical simulation (DNS) [59], which is also used by He *et al.* (2018) for investigating the dynamic behaviors of lock-exchange turbidity currents down a slope [32]. The numerical predictions related to the research of Ouillon *et al.* (2021) were consistent with the field experiment results, which were conducted at a depth of 4500 m in the CCZ region by Lin *et al.* (2023) [46]. It should be noted that the discharge from the source from Ouillon *et al.* (2021) is in a vertical direction instead of the (more relevant for this research) horizontal direction, which gives a different momentum to the flow [59].

According to Blanchette (2022), who used a box model (BM) and shallow-water equations (SWE) to solve the spread of the current numerically, the relevant quantities are averaged horizontally over the total extent of the current. From the box model, it is found that the spread of the current is very similar for a range of V_s, however when the moving source comes to a halt, the spread of the current quickly slows down, due to larger settling velocities near the discharge point. From the SWE it is found that the source velocity even has less influence on the spread of the current, for the considered period (30 s), but that the rate of spread is significantly higher than for the box model. However, Blanchette (2022) also states that the SWE over-predicts the rate of spreading of the current, resulting in an overestimation of the spreading area [9].

According to Blanchette (2022), the V_s does positively influence the deposit rate [9]. In addition to that, the increase of the velocity ratio, and therefore V_s relative to V_d, is found to generate smaller discharge angles [63], which are defined in Figure 2.7. The initial spreading angle is defined as α, the spreading angle after impingement is defined as β and the impingement angle is defined as θ. The impingement length is defined as L_i.

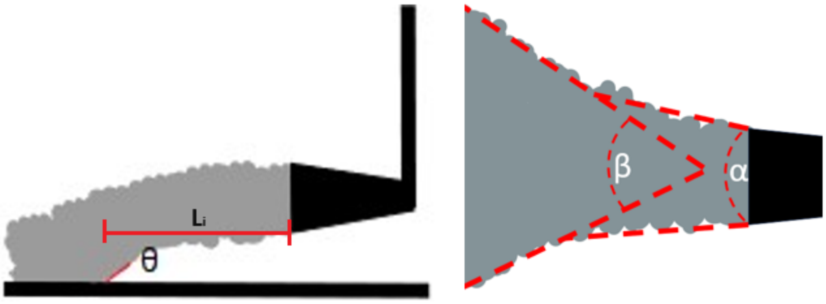

Figure 2.7: Turbidity current angle definitions [63]

It is found that the Froude number, calculated as per Equation (2.19) of the flow is of big influence for the behaviour of the turbidity current. This shows in the shape, the deposit and the dispersion. For a Froude number of $Fr^2 > 2$, which is a super-critical regime, the current takes a more elongated shape and for $Fr^2 < 2$, which is a sub-critical, the current takes a more round shape [9]. At a lower Froude number ($Fr = 0.6$), the flow is also less homogeneous, with higher concentrations at the sides of the diffuser, due to more spreading in the direction perpendicular to the velocity direction of the SMT, also resulting in an increasing deposit height of the turbidity current [9, 63]. In addition to that, the impingement length increases, decreasing the impingement angle θ. A higher Froude number decreases the impingement length and increases θ [63]. For $Fr^2 \approx 2$, the current is in an intermediate state, a transition regime, where the current shows a minor elongation, substantiated by both the SWE and the BM from Blanchette (2022) [9].

Blanchette (2022) introduced a drag coefficient in the model to correct for the wake of the SMT, but found that this does not have much influence on the current beyond the immediate vicinity of the vehicle [9]. The length of the entire wake is affected by a change in velocity however, it increases exponentially with the relative discharge velocity (V^*) of the plume, as defined by Liu *et al.* (2023) as the dimensionless difference between source velocity and discharge velocity of the plume ($V^* = \frac{V_s - V_d}{V_s}$) [47], somewhat different than the velocity ratio as defined in Equation (1.1).

2.4. Experimental Research

In this section, important aspects of experimental research are described. In Section 2.4.1, the process and importance of scientific scaling are described. Section 2.4.2 gives the recommendations from previous research.

2.4.1. Scientific Scaling

To research complex physical processes without using simulation programs or numerical models, an experiment setup can be made. For DNC, the tools and processes that are in play are of large dimensions as such, they have to be scaled down to improve the workability and reduce the costs of the experimental setup. This is where scientific scaling comes into play. Scientific scaling can be done based on the geometric, kinematic or dynamic principle. The most commonly used scaling factors are the Froude number, calculated as per Equation (2.19) and the Reynolds number, calculated as per Equation (2.20). The Froude scaling provides an equality for the ratio between inertia and gravitational forces, while Reynolds scaling provides an equality for the ratio between inertia and viscous forces [76, 79]. Scaling can be applied with a length scale factor, which can be calculated as per Equation (2.24). In the research from Van Pelt (2023), a scaling factor of $\alpha = \frac{1}{20}$ is used, after an iterative approach [63].

$$\alpha_s = \frac{L_r}{L_m}, \tag{2.24}$$

where L_r is the length in reality and L_m is the length in the model.

Accurate scaling can be done with either scaling factor (Froude or Reynolds), but combining the two is very tricky, because both rely on different principles, as explained in Section 2.3.3. For example, assuming that the length scale factor is defined as per Equation (2.24), where L_m is the length of the model and L_r is the length in reality for Froude scaling, the velocity scale factor would be equal to $\sqrt{\alpha_s}$, but for Reynolds scaling, it would be $\frac{1}{\alpha_s}$. The Reynolds number is in particularly useful for flow classification, because it describes the turbulence of a flow in a dimensionless parameter, meaning that different flow regimes can be differentiated. These flow regimes are as per Table 2.2.

2.4.2. Previous Recommendations

Multiple (practical) recommendations for improving the quality of the experiments done in the modular flume in the sediment lab at the TU Delft have been made by experts by experience. These recommendations are described below.

Mixture Concentration Accuracy

The experimental setup used by Van Pelt (2023) consists of a flume tank and a mixing tank, as can be seen in Figure 1.4. The mixture concentration is one of the key parameters in the experimental runs, meaning that it is very important to measure the mixture concentration accurately and to make sure that the concentration that is measured in the mixing tank is also discharged in the modular flume. During the experiments from Van Pelt (2023), it was noticed that the sediment in the mixing tank was not homogeneously distributed throughout the whole tank, meaning that the concentration within the mixing tank was not homogeneous. It is believed that the reason is a lack of energy (distribution) throughout the mixing tank. This problem can be solved by adding an extra pump to the mixing tank to generate a more turbulent environment, reducing the settling of sediment [63]. In addition to that, it is also recommended to add an ADV (explained in Section 3.2.1) in front of the discharge pump inlet, to have accurate, real-time data of the mixture concentration that is discharged in the modular flume [63].

Velocity ratio

During the experiments of Van Pelt (2023), the the ratio a of cart velocity over buoyant velocity is used, as proposed by Ouillon (2021), but according to Van Pelt (2023) this ratio is overly complicated, because the buoyant velocity of a plume is hard to determine during experiments [59, 63]. Therefore Van Pelt (2023) advised a different ratio, ζ, which is defined as cart velocity over discharge velocity, as can be seen in Equation (1.1), which is more simplistic and much easier to enforce in the test runs [63].

Flow Regime

As described in Section 2.3.7, according to Blanchette (2022) the turbidity current can be divided into three different regimes: sub-critical ($Fr^2 < 2$), intermediate ($Fr^2 \approx 2$) and super-critical ($Fr^2 > 2$) regimes. The intermediate regime needs more understanding according to Blanchette (2022), because the constructed model was unable to accurately quantify the maximum spread of the deposits, due to small settling speeds that required a larger computational domain [9]. Therefore, Blanchette (2022) recommends further research into turbidity currents within this regime.

Algae Growth Prevention

During the experiments of Van Pelt (2023), it was noticed that over time the clarity of the water reduced, leading to a decrease in video footage quality. The cause for this was the growth of algae in the modular flume. A proposed method to counter (or reduce) the growth of algae is by using a solution of sodium hypochlorite (bleach), which is also used in the towing tank of the Technical University Delft (TUD). Based on communication with the responsible staff of the towing tank, one liter with a 12.5% solution would be enough to greatly reduce algae growth in the modular flume [63].

2.5. Conclusion

In this paragraph, preliminary answers are given to the research questions. In general, every answer is a conclusion from the literature research and a hypothesis for the research question.

- When do unwanted phenomena occur during the discharge or near-field dispersion of a turbidity current on a sloping seabed from a moving source?

Based on the literature research, no substantiated answer can be given to this research question. A phenomenon that will negatively impact the effects of deep-sea mining that is described in the literature is auto-suspension, where the vertical bed slope velocity is larger than the settling velocity of the sediment particle and the particles remain in suspension instead of settling. However, no conditions are described for when this might occur.

- How will the ratio of source velocity over discharge velocity influence the near-field dispersion of a turbidity on a slope?

A higher source velocity will result in lower dispersion angles, but will overall not have too much influence on the dispersion of the turbidity current. A higher discharge velocity, on the other hand, will result in a smaller impingement angle, meaning that more energy from the mixture will be transferred into the discharge direction, decreasing the dispersion of the turbidity current. Logically, for a lower discharge velocity, the horizontal momentum will be lower.

The velocity ratio is defined as the source velocity over the discharge velocity, meaning that if the influence of the source velocity is minimal, the influence of the velocity ratio is dominated by the inverse influence of the discharge velocity. This means that for a lower velocity ratio, the dispersion of a turbidity current decreases.

3 | Experimental Methodology

In this chapter, the methodology of the experiments is described. The experiments were carried out in a flume tank in the Offshore and Dredging Laboratory of TU Delft. In Section 3.1, the experimental setup is discussed. Section 3.2 describes the different measurement techniques used in the setup, to obtain the required data. Section 3.3 describes the used method to calibrate the different devices. In Section 3.4, the different parameters and assumptions for this experiment are described and discussed. Lastly, Section 3.5 gives the exact procedure for how the experiments are performed.

3.1. Experimental Setup

The basic experimental setup has already been used before by Van Pelt (2023) [63], which can be seen in Figure 1.4. The setup design will be used and adjusted to serve the purpose of this research. Both the moving cart (as described in Section 3.1.1) and the imitated seabed (as described in Section 3.1.1) will be placed under an angle, to simulate a sloping seabed. The experiments are done on a scale of 1:20, the same scale factor as Van Pelt (2023) used [63]. The setup can be seen in Figure 3.1.

Figure 3.1: Overview of the experimental setup

3.1.1. Modular Flume

The experiments will take place in a modular flume tank. This tank has a length of 5 m, a width of 2.25 m and a height of 2 m, as can be seen in Figure 3.2, and will be filled with fresh water with a one litre 12.5% solution of bleach to prevent algae growth. This tank has been used in earlier research regarding DSM plume discharge by Van Grunsven *et al.* (2018), Osejo Rodriguez (2019), Blankenaar (2020), Wijmans (2021) and Van Pelt (2023) [10, 30, 57, 63, 81]. The flume has glass panels all around for good visibility inside.

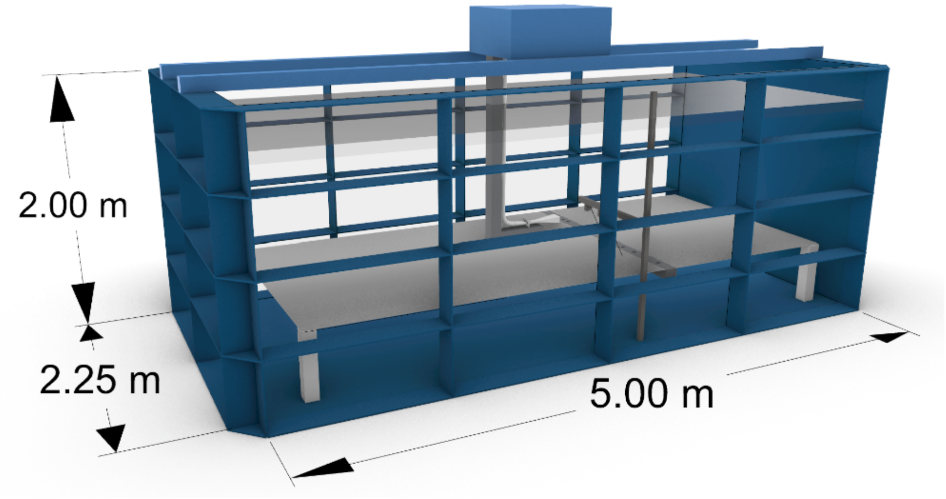

Figure 3.2: Modular flume with dimensions [63]

Sloping Rails and Seabed

On the bottom of the flume tank, a table is placed to simulate the seabed. This table has integrated light boxes to increase contrast for better visibility. To simulate a sloping seabed, the table is placed under specific angles, which is further explained in Section 3.5. On top of the tank, two beams have been placed with rails mounted on them. The beams are resting on a nut on threaded rods, attached with hinge joint to the tank, as can be seen in Figure 3.3, so the height of the beam above the top of the tank can be adjusted to obtain different slope angles. The table in the tank is secured to the rails with hinge joints and rods, to make sure that when the rails are placed at an angle, that same angle is set to the table, effectively creating a sloping seabed with parallel rails (Section 3.4.2).

Figure 3.3: Threaded rod, supported by a hinge, to adjust the angle of the rails and table

Moving Cart with Diffuser

On top of the rails, a cart can be driven by a chain. This cart holds a vertical frame, immersed in the water. This frame supports a discharge pipe with at the end a horizontal diffuser to discharge a mixture into the water, as described in Section 3.1.2. The horizontal centreline of the diffuser is placed at exactly 100 mm above the table (Section 3.4.2). The cart with the diffuser frame and diffuser hanging under it can be seen in Figure 3.4a. The moving cart with an underwater diffuser simulates an operating PNMT. The cart on the rails is controlled by a panel, containing a button for left and right and a power supply rotary knob, which can be seen in Figure 3.4b.

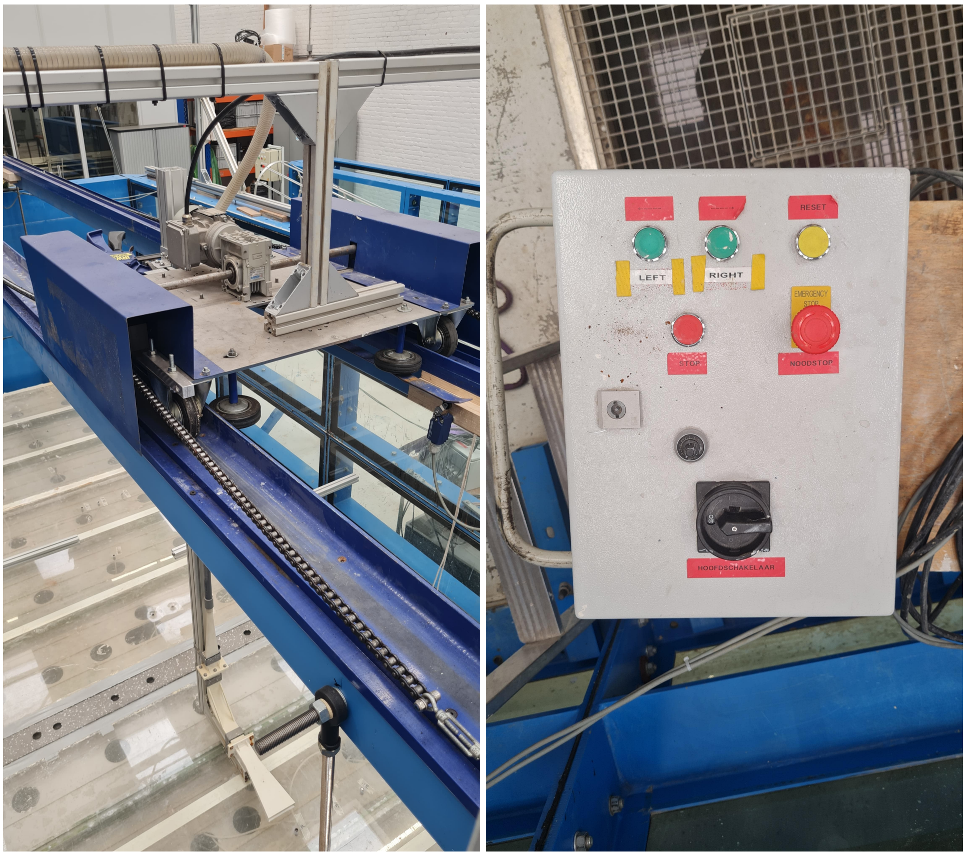

(a) Cart on rails with diffuser

(b) Control panel of moving cart

Camera setup

The camera setup consists of three camera angles: a top view, a side view and a mounted view. Both the top and side views are focused on the same location where the transducer is located, as described in Section 3.1.1 and visualized in Figure 3.5. The camera for the mounted view is secured on the diffuser frame and provides a constant top view of the diffuser mouth. The side view camera is placed on the outside of the tank, against the glass wall. Both the top and mounted view cameras are secured on secondary frames, making them easily removable out of the water.

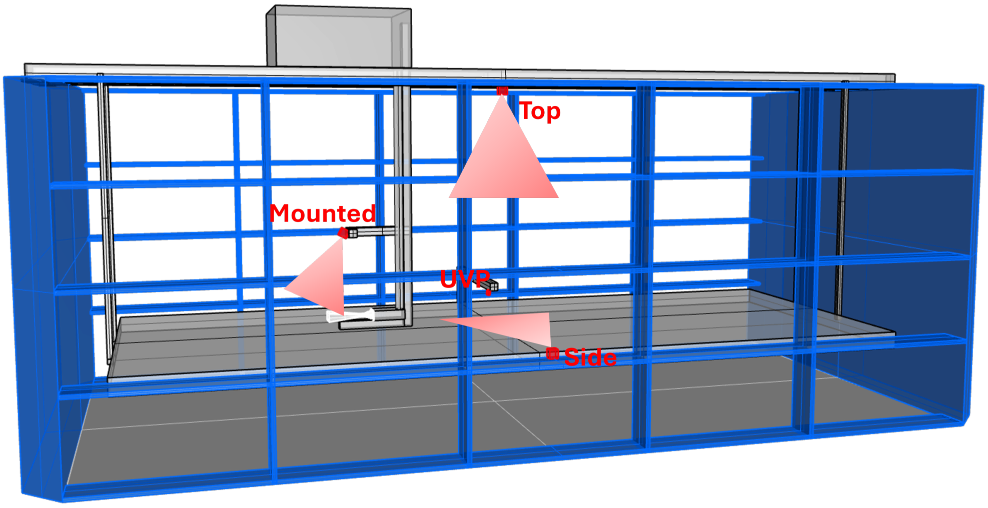

Figure 3.5: Visualisation of camera angles

Sensor Placing

Two devices are used in the experimental setup, namely an acoustic Doppler velocimeter (ADV) and two different ultrasonic velocity profilers (UVP), which are explained in Section 3.2. The ADV probe is placed in the centre of the mixing tank and is used to measure the concentration of the mixture before every experiment.

The UVP transducer is placed within the flume, at halfway the length of the flume, with an offset of 10 cm from the centre (driving) line, and a distance of 20 cm perpendicular above the table, pointing towards the side of the tank with a 25° angle. This UVP is used to obtain a velocity profile of the head of the turbidity currents, propagating towards the side wall of the tank. A visualization can be seen in Figure 3.6.

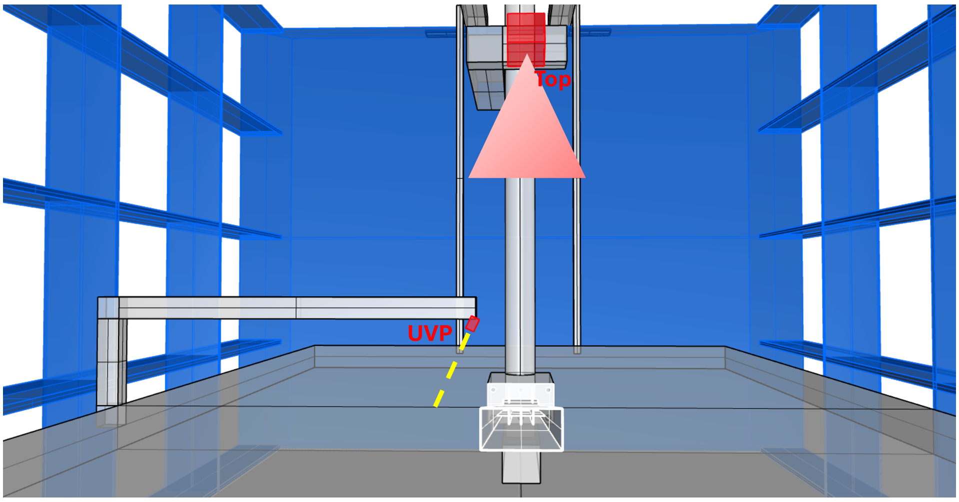

Figure 3.6: Visualisation of UVP placing and profile

The flowmeter to measure the mixture flux, is placed on a pipe connecting the mixing tank, through a pump and hoses, with the diffuser. The pipe has a straight part before and after the flowmeter, to ensure a fully developed flow at the measurement point. The flowmeter that is used, is the KATflow 200. The flux through the pipe can be regulated by a valve system after a pump, with a backflow option to the mixing tank.

Figure 3.7: KATflow 200 flowmeter

3.1.2. Mixing Tank and Mixture

Due to the cohesive effects (described in Section 2.1.3) and cumbersome nature of clayey material, the choice has been made to substitute the clay with glass beads, from now on referred to as "sediment". The particle diameter of the used glass beads is in the range of 40 to 70 μm and they have a density of 2,460 $\frac{kg}{m^3}$. Using a non-cohesive mixture means that no flocculation will occur, meaning that an important physical aspect of clay will be missing in the experiments. However, due to the higher density of the glass beads and the lack of very small particles, they will settle faster in the flume, resulting in the experiments being conducted faster. Blankenaar (2020) conducted experiments with similar material (glass beads) as used in these experiments [10]. The results can be seen in Figure 3.8.

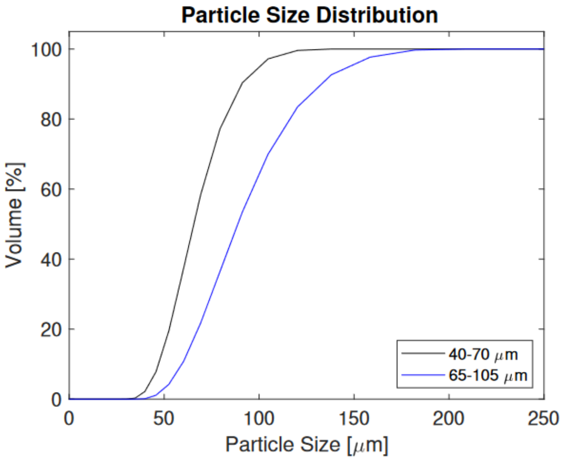

Figure 3.8: Particle size distribution of glass beads with a particle diameter of 40 to 70 and 65 to 105 μm [10]

The mixing tank has a volume of 0.5 m^3 or 500 litre and it will hold a mixture with a volume concentration of 2.5% or 61.5 gram glass beads per litre water respectively, converted as per Equation (3.1). The glass beads are brought into suspension by three submersible pumps and one water pump with a backflow hose, to create a homogeneous mixture. From the mixing tank, the mixture is pumped through the diffuser into the flume tank by the water pump.

$$c = c_{vs} \cdot \frac{\rho_s}{\rho_s + \rho_l} \tag{3.1}$$

where c $[\frac{g}{L}]$ is the concentration of sediment in the water.

3.2. Measurement Techniques

In this section, the different measurement techniques that are used during the experiments are discussed, which are the ADV, UVP and flowmeter(Section 3.2.1), the camera footage (Section 3.2.2) and the Niskin bottle (Section 3.2.3).

3.2.1. ADV and UVP

With an ADV and UVP, the velocity of particles in a flow can be measured. For the ADV, based on the signal-to-noise ratio (SNR), the concentration can be calculated and for the UVP, based on the surface area that a flow goes through, the flux through a pipe can be calculated.

The working principle is based on the Doppler effect, which states that there is a difference in the frequency of a sound heard when standing still and when moving either towards or away from an acoustic source, the so-called Doppler shift. Because the ADV and UVP are both the transmitter and the receiver in a single probe and the transmitted acoustic waves have to bounce back on a particle, they measure twice the Doppler shift. In the case of the flowmeter device, KATflow 200 has a transmitter and a receiver in two different sensors. The resulting relative velocity between the source and reflecting particle can be calculated as per Equation (3.2) [43, 56], which is the basis for the velocity of a flow in three directions: x, y and z.

$$v_{rel} = \frac{f_d \cdot C}{2 \cdot f_s} \tag{3.2}$$

where f_d [Hz] is the Doppler frequency shift, f_s [Hz] the frequency of the sound when both the receiver and the acoustic source are stationary, C [$\frac{m}{s}$] the speed of sound and V [$\frac{m}{s}$] the relative velocity between the source and reflecting particle.

With the input of the dimensions of the pipe that the flowmeter is placed on, the total mixture flux that goes through the pipe can be calculated. Calculating the concentration can be done with the signal-to-noise ratio (SNR). Measurements during a stationary setup with a homogeneous mixture give an unwanted noise, based on the concentration of the mixture and the particle characteristics. When the concentration of the mixture is known, a calibration curve can be constructed to measure the concentration in situations with unknown concentration, as described in Section 3.3.1.

For measurements in a smaller setup, the reflected acoustic waves from a hard surface, such as the bottom of a tank, are much stronger than the reflected acoustic waves from the suspended particles in the water. This means that the UVP has to be placed under a certain angle, so that the transmitted acoustic wave is never perpendicular to a hard surface, like a tank wall or bottom [43, 56]. An example of an experimental setup including a UVP can be seen in Figure 3.9. It can be seen that the UVP is placed under an angle towards the bottom and that the velocity is measured at a distance from the transducer where particles are observed.

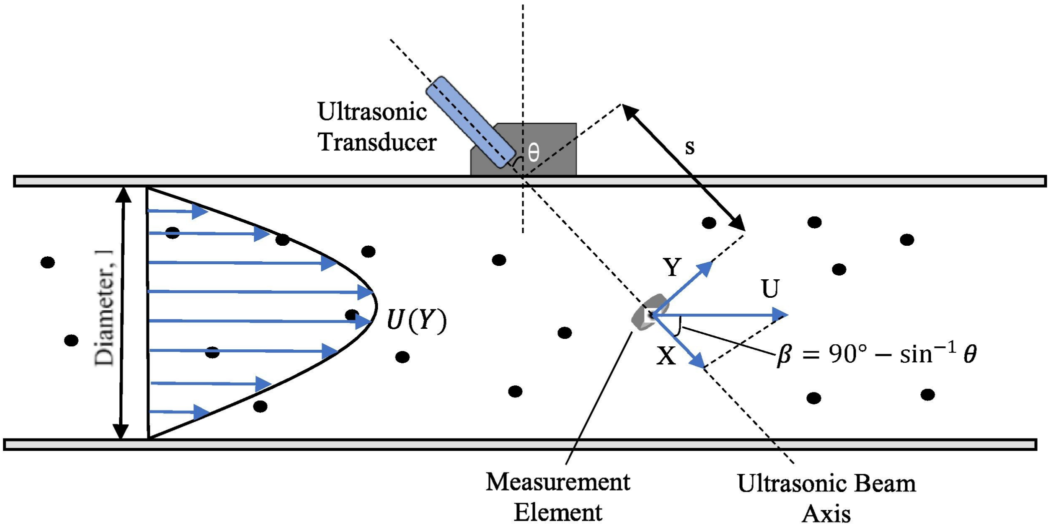

Figure 3.9: Schematic illustration of an experimental setup in a pipeline including a UVP [43]

3.2.2. Visualisation

The behaviour of the turbidity current can be observed with camera footage. By placing multiple cameras at different angles and positions, focused on the turbidity current, specific phenomena can be captured and analysed, like the formation of the current head or the turbulent billows at the upper interface of the current head (Section 2.3.6). The camera placing can be seen in Figure 3.5.

3.2.3. Niskin Bottle

A Niskin bottle is made to draw samples from the mixing tank before every experiment. This is a more robust way of verifying the mixture concentration. Because the sample first has to be analysed (as described in Section 4.4), before the sampled concentration is known, it is mainly used to verify the results from the ADV.

3.3. Calibration of the Devices

In this section, the calibration methods for the devices are described. Section 3.3.1 describes the method for the calibration of the ADV. Section 3.3.2 describes the calibration of the diffuser cart velocity.

3.3.1. ADV Calibration

The calibration of the ADV was done at the Physic Chemical Laboratory of Deltares, where a balance with a resolution of 0.01 mg was available. The ADV is placed in a container with a volume of 8.5 litres, together with two mixing tools to keep the water turbulent enough to suspend the sediment and create a homogeneous mixture. The concentration of the sediment is increased in steps of 5 $\frac{g}{L}$ and with the ADV the SNR is recorded. These data points are plotted against the known concentration and a linear trend line is plotted through those points, as can be seen in Appendix D. The calibration setup and method are based on experiments done by Chmiel *et al.* (2018) [15]. The trend line that is plotted is linear and not logarithmic, which is to be expected when dealing with acoustic measurement techniques, because the SNR is already defined in decibels and therefore logarithmic.

3.3.2. Cart Velocity Calibration

To impart a certain velocity to the cart, it is necessary to have a calibration curve that links the input to the output, because the input is a rotary value (0-10), but the required output is the cart velocity. This has to be done for every slope angle, because for every uphill or downhill slope angle, a different amount of power is required for the cart to reach a certain velocity. Therefore, for every slope angle and direction, the amount of time it takes for the cart to drive a certain distance is measured for different rotary values, to obtain the power-to-velocity curve of the cart. The cart velocity calibration curves at corresponding slope angles and driving directions can be seen in Appendix A.1. The trend lines that are drawn through the data points are second order, because that is the relation between velocity and resistance.

3.4. Assumptions and Parameters

In this paragraph, the assumptions and parameters of the experiments are given and discussed. In Section 3.4.1, the sediment and mixture are discussed. Section 3.4.2 describes the seabed assumption and discusses the height of the diffuser. The slope angles are described in Section 3.4.3. Lastly, Section 3.4.4 describes the velocity ratio parameter.

3.4.1. Glass Beads and Diffuser

As described in Section 3.1.2, instead of real clay from the CCZ, the choice is made to use glass beads with similar d50, shape and density, due to the cumbersome nature of clayey materials. In addition to that, this substitution is also made to isolate the behaviour of the singular particles within a turbidity current, since clayey materials tend to flocculate, as described in Section 2.1.3.

The diffuser that is used to discharge the mixture underwater has an outflow area of 0.002 m^2, with vanes added on the inside to ensure a well-divided flow. A render of the diffuser can be seen in Figure 3.10.

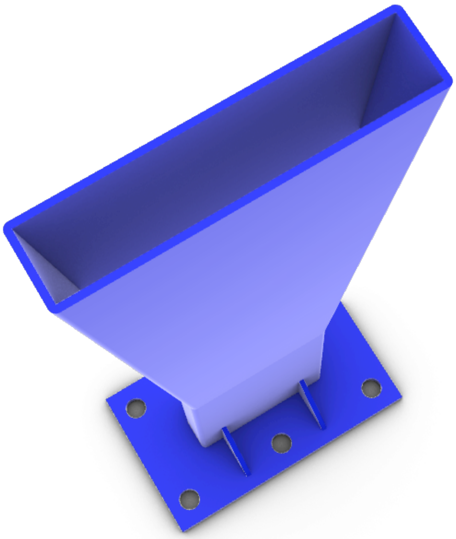

Figure 3.10: 2.5% volume concentration diffuser with a discharge area of 0.002 m^2 (0.1x0.02)

3.4.2. Seabed and Diffuser Height

The seabed is mimicked by a table, suspended from the rails by rods. Unlike a real seabed, the table is smooth, without any loose sediment depositions. This simplification is made to avoid interaction between sediment deposition and the turbidity current and the influence of roughness on the propagation of the turbidity current. In addition to that, creating a realistic seabed with known characteristics for an experimental setup at this scale is very challenging.

Blankenaar (2020) concluded in her research, for a stationary source and a scale of 1:15, that the recommended distance between the horizontal centreline of the diffuser and the table is 100 mm [10]. Without taking the scaling factor into account, this value is also used by Van Pelt (2023) at a scale of 1:20 [63]. It is unknown whether having a moving source instead of a stationary setup influences this value, however, no significant differences in physics and process have been observed. For this research to be reliably comparable to the research of Van Pelt (2023), the height of the centreline of the diffuser above the table is also chosen to be 100 mm.

3.4.3. Slope Angles

Due to the practical limit of the setup, the maximum angle that can be tested is 5°. The range of angles that are tested are therefore -5° till 5° at -5°, -4°, -3°, 0°, 3° and 5°. The negative slope angles are for the downhill driving experiments, the positive slope angles are for the uphill driving experiments. The rails are mounted on the tank through threaded rods and hinges, enabling one side of the rails to be lifted, placed and secured under an angle. Since the table is suspended from the rails, it also takes that same angle.

3.4.4. Velocity Ratios

From the literature, it is expected that for a velocity ratio (ζ, calculated as per Equation (3.3)) of 1, where the source velocity is equal to the discharge velocity, the initial dispersion of the turbidity current is the least, as described in Section 2.2.1. A velocity ratio higher than 1 means a lower discharge velocity than source velocity, which is interesting, because it would give a horizontal momentum in the direction of the diffuser. To verify this and determine the influence of the velocity ratio on the dispersion of a turbidity current, two different velocity ratios are tested, namely 1.00 and 1.25.

$$\zeta = \frac{v_s}{v_d}, \tag{3.3}$$

3.5. Experimental Procedure

The experimental procedure for each experimental run is as follows:

1. Clean the table.
2. Check whether the rails have the correct slope angle. If not, adjust correctly and do a cart velocity calibration (Section 3.3.2).
3. Check whether the diffuser is discharging correctly. If not, flush the system with fresh water to get rid of the air in the system.
4. Wait till the water is completely at rest, approximately 1-2 hours.
5. Bring the sediment in the mixing tank into suspension until it is a homogeneous mixture.
6. Do an ADV measurement in the mixing tank (Section 3.2.1).
7. Take a Niskin bottle sample from the mixing tank (Section 3.2.3).
8. Do a temperature measurement in both the mixing tank and the flume.
9. Put the cameras on the frames, start the recording and secure the frames in the flume (Section 3.1.1).
10. Drive the cart to the beginning of the rails at a slow pace to minimize the disturbance of the water.
11. Check if all the sediment in the mixing tank is suspended.
12. Check if the black cloth is fully closed.
13. Put the desired power into the cart.
14. Ready the UVP measurement and the stopwatch.
15. Open the pump valve until the desired flow is obtained (Section 3.2.1).
16. Start the UVP measurement (Section 3.2.1).
17. Start the cart and the stopwatch at the same time.
18. When the cart reaches the end of the rails, stop the stopwatch and close the pump valve.
19. Wait five minutes, then take out the camera frames and stop the recording.
20. Repeat.

Strictly following these steps ensures that every experiment is performed in exactly the same way, eliminating as many procedure errors as possible.

4 | Results

This chapter gives the results from the different measurement techniques used during the experiments, which are the camera footage, UVP measurements, ADV measurements and Niskin bottle samples. Firstly, Section 4.1 gives the test matrix and the respective variable parameter values. In Section 4.2, the results from the camera footage are given and it is explained how they are obtained. Section 4.3 describes how the velocity profiles from the UVP data are obtained and how they are checked for their reliability. Lastly, Section 4.4 describes how the mixture concentration is obtained from the ADV measurements and the Niskin bottle samples and how they compare to the aimed mixture concentration.

4.1. Experiments

The test matrix can be seen in Table 4.1. The variables within the experimental matrix are the slope angle (i), the volume concentration (c_{vs}) of the mixture, the velocity ratio (ζ) and the driving direction. The velocity ratio gives the ratio between the source velocity (v_s) and the discharge velocity (v_d) as per Equation (1.1). It seems that the experimental numbering lacks any logic, however, a lab closure caused significant delay, resulting in not being able to perform all the experiments from the intended experimental matrix, which included experiments with a lower volumetric concentration (1 %) of the mixture. While these remaining experiments are to be beyond the scope of this thesis, the original numbering system has been maintained for consistency. It can be seen that experiment 8 has multiple variations, which are made to zoom in on specific effects of the turbidity current.

Table 4.1: Test matrix

Experiment	i [°]	c_{vs} [%]	ζ [-]	V_s [$\frac{m}{s}$]	V_d [$\frac{m}{s}$]	Driving direction [-]
1	0	2.5	1.35	0.16	0.119	Flat
2	0	2.5	0.97	0.14	0.140	Flat
7	-5	2.5	1.25	0.067	0.054	Downhill
8	-5	2.5	1.00	0.067	0.067	Downhill
8.1	-5	2.5	1.00	0.11	0.11	Downhill
8.2	-5	2.5	1.00	0.044	0.044	Downhill
8.3.2	-5	2.5	1.68	0.067	0.040	Downhill
9	-3	2.5	1.25	0.067	0.054	Downhill
10	-3	2.5	1.00	0.067	0.067	Downhill
15	-4	2.5	1.25	0.067	0.054	Downhill
16	-4	2.5	1.00	0.067	0.067	Downhill
21	5	2.5	1.25	0.067	0.054	Uphill
22	5	2.5	1.00	0.067	0.067	Uphill
23	3	2.5	1.25	0.067	0.054	Uphill
24	3	2.5	1.00	0.067	0.067	Uphill

4.2. Camera Footage

The camera footage is analysed using Digimizer. This program can analyze figures to determine angles (diffuser angle, dispersion angle, and impingement angle) and relative lengths (impingement length and bulge length). The definitions of these angles and lengths (except for bulge length, which is defined in this paragraph) are given in Section 2.3.7.

The diffuser and dispersion angles are obtained from both the top view and the mounted view camera footage. The impingement angle is obtained from the side-view camera footage. The footage is analysed at multiple timestamps around the point where the turbidity current is passing underneath the UVP transducer. At each of these timestamps, angles are determined and averaged for one video (or experiment). An example of the analysis of a single timestamp can be seen in figure 4.1 and Figure 4.2. All the camera views have been made horizontal, to increase the ease of the analysis.

Figure 4.1: Side view footage at experiment 16

Figure 4.2: Mounted view footage at experiment 9

The impingement length is calculated from the impingement angle. Because the height of the centreline of the diffuser above the table (h_d) is known, the impingement length can be calculated with a trigonometric function, as per Equation (4.1).

$$L_i = \frac{h_d}{\tan(\theta)} \tag{4.1}$$

From the side view footage, a phenomenon has been observed. At certain slope angles, the impingement of the sediment plume has a horizontal direction component back towards the diffuser, resulting in a turbidity current bulge under the diffuser. This can be seen in Figure 4.3. The length of the bulge is defined as the distance from the tip of the impingement angle to the tip of the bulge and is obtained from the side view camera footage as well. The length of the bulge (L_b [m]) is calculated by measuring both the diffuser height and the length of the bulge in Digimizer in pixels. Because the height of the diffuser is known, the length of the bulge can be calculated. The bulge formation will be further analyzed in Section 5.1.1.

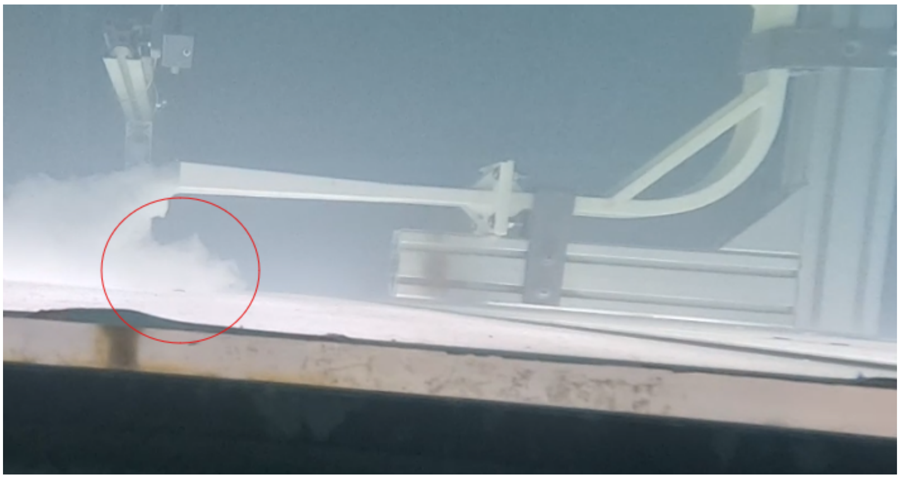

Figure 4.3: Bulge phenomenon at experiment 7

In Table 4.2, the resulting plume characteristics per experiment based on the analysis of the camera footage and the temperature measurements in the mixing tank and flume are given.

Table 4.2: Plume characteristics from the downhill driving tests based on camera footage

Experiment	i [°]	c_{vs} [%]	ζ [-]	V_s [$\frac{m}{s}$]	V_d [$\frac{m}{s}$]	dT [°C]	α [°]	β [°]	θ [°]	L_i [m]	L_b [m]
1	0	2.5	1.35	0.16	0.119	4.9	15	25	20	0.242	0.000
2	0	2.5	0.97	0.14	0.140	4.7	13	39	15	0.338	0.000
7	-5	2.5	1.25	0.067	0.054	1.3	17	86	47	0.085	0.150
8	-5	2.5	1.00	0.067	0.067	3.7	7	92	48	0.081	0.101
8.1	-5	2.5	1.00	0.11	0.11	6.4	21	64	23	0.208	0.000
8.2	-5	2.5	1.00	0.044	0.044	5.5		106	46	0.088	0.054
8.3.2	-5	2.5	1.68	0.067	0.040	11.7	10	41	26	0.188	0.041
9	-3	2.5	1.25	0.067	0.054	18.9	17	102	27	0.174	0.125
10	-3	2.5	1.00	0.067	0.067	22.8	11	85	23	0.216	0.000
15	-4	2.5	1.25	0.067	0.054	1.2	17	43	19	0.262	0.158
16	-4	2.5	1.00	0.067	0.067	2.6	11	52	23	0.211	0.105
21	5	2.5	1.25	0.067	0.054	5.4	10	60	27	0.175	0.000
22	5	2.5	1.00	0.067	0.067	1.7	18	69	48	0.081	0.000
23	3	2.5	1.25	0.067	0.054	4.1		53			0.000
24	3	2.5	1.00	0.067	0.067	2.7	15	65	37	0.118	0.000

It can be seen that for experiment 8.2 and experiment 23, there is no data for the diffuser angle (α), because of a poor outflow of the mixture from the diffuser, which can be seen in Figure 4.4. In addition to that, no impingement angle (and length) could be obtained for experiment 23, because during the file handling of the side view footage an error occurred, destroying the footage.

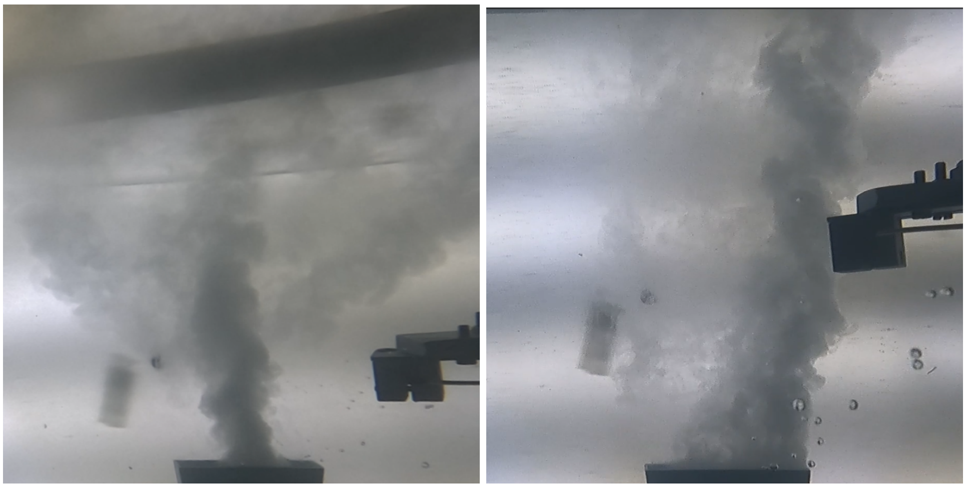

Figure 4.4: Poor mixture outflow from the diffuser at experiment 8.2 (left) and experiment 23 (right)

The snapshots used to analyze the footage of all the experiments for the three different camera angles can be seen in Appendix B.

4.3. UVP Data

To obtain the correct data from the UVP, first an estimation has to be made at what timestamp the head of the turbidity current would pass the UVP transducer. This is done by matching the camera footage with the UVP measurement duration. A raw velocity profile looks like the profile depicted in Figure 4.5.

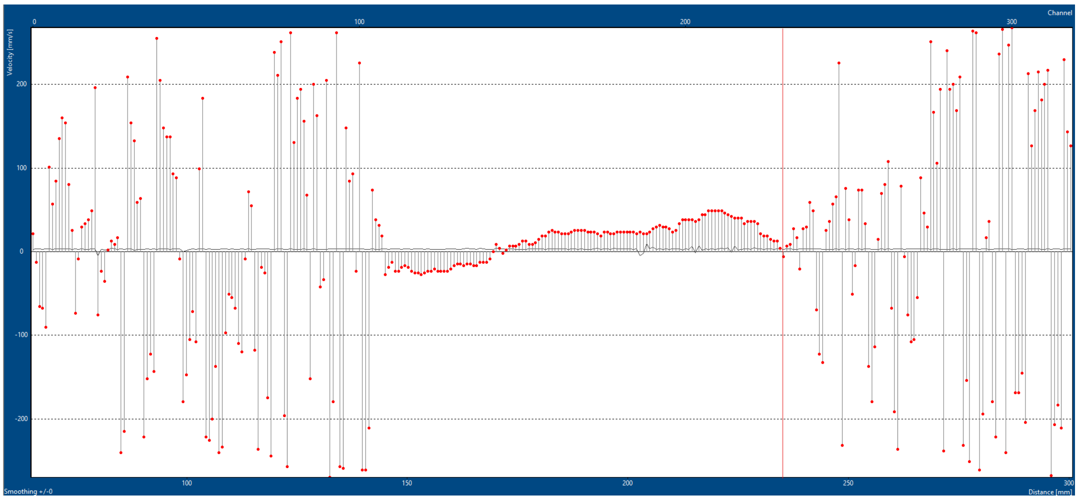

Figure 4.5: Raw UVP measurement from experiment 16 with the red line indicating the position of the table

Around the timestamp where the turbidity current passes the UVP transducer, the velocity profile is taken and averaged over three consecutive measurements (n[v_1, v_2,v_3]). From this averaged velocity profile, the variance (s^2 [$\frac{mm^2}{s^2}$]) is calculated, as per Equation (4.2), to show the reliability of the averaged measurement. The noise is deleted from the velocity profile data where the variance is consistently high, to create an actual velocity profile.

$$s^2 = \frac{(v_1 - \bar{v})^2 + (v_2 - \bar{v})^2 + (v_3 - \bar{v})^2}{n - 1} \tag{4.2}$$

where $\bar{v}$ $[\frac{mm}{s}]$ is the average velocity of the datapoint, calculated as per Equation (4.3).

$$\bar{v} = \frac{v_1 + v_2 + v_3}{n} \tag{4.3}$$

Knowing the variance itself is insufficient to determine whether certain data points are reliable. A high variance is worse for a velocity nearing 0 than a higher velocity. Therefore, a maximum relative variance deviation of 20% is chosen, concerning the maximum dispersion velocity (v_{max} $[\frac{mm}{s}]$) within the actual velocity profile. This variance reference line is drawn according to the calculation as per Equation (4.4).

$$s^2_{check} = \omega^2 * \bar{v}^2, \tag{4.4}$$

where ω is the variance deviation, with a value of 0.2 for a variance deviation of 20%. All the data points with a higher variance than the s^2_{check} are displayed differently in the velocity profile plot, because they have a higher deviation than 20% and are therefore less reliable. A plot with the averaged velocity profile, the actual variance and the variance check can be seen in Figure 4.6.

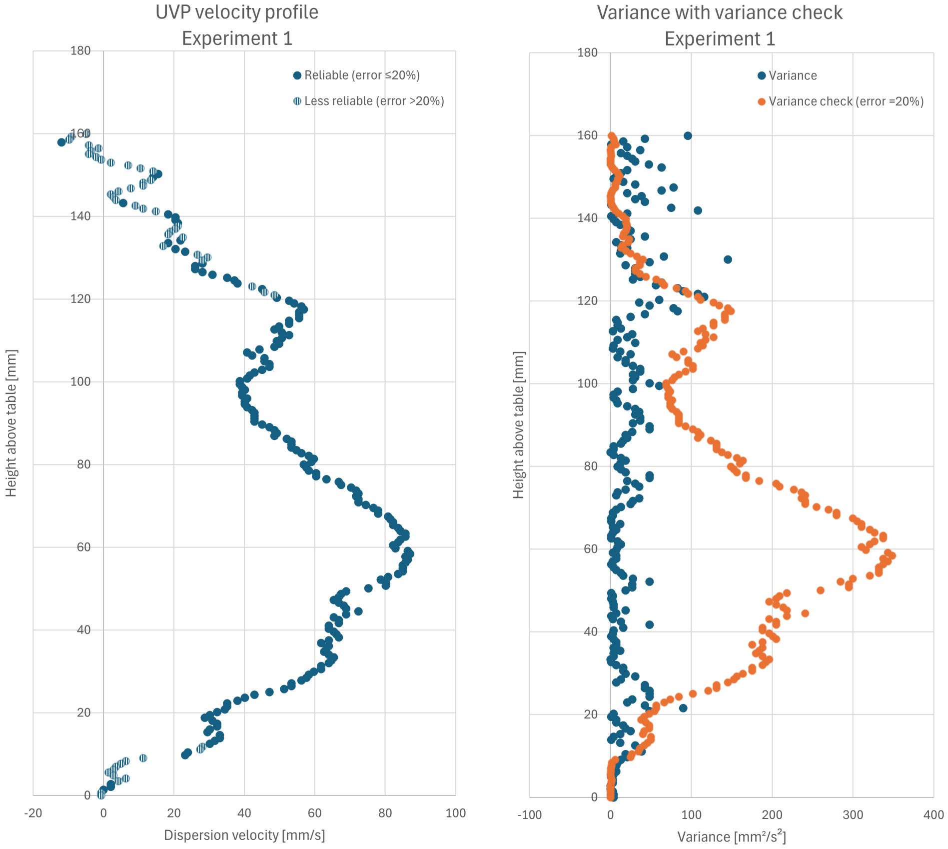

Figure 4.6: Velocity profile with variance and variance check plot from experiment 1

The velocity profiles and variance plots from all the experiments can be seen in Appendix C. Only the velocity profile of experiment 8.1 is missing, due to an error while performing this experiment.

4.4. Concentration Measurements

Before every experiment, the ADV is placed in the centre of the mixing tank and is used for a 50-second long concentration measurement of the mixture, as described in Section 3.1.1. The result from one measurement is four datasheets, one per probe, with SNR readings, as explained in Section 3.2.1. These readings are averaged and converted to a concentration with the help of the calibration curve, given in Appendix D, that is obtained by calibrating the ADV, as described in Section 3.3.1.

In addition to that, samples have been drawn from the mixing tank with a Niskin bottle, as mentioned in Section 3.2.3. This is in theory a perfect sample from the mixture, which is a reliable way to verify the ADV measurements. With the known volume of the Niskin bottle and the total weight of the captured sediment in the Niskin bottle, the concentration of the sampled mixture can be calculated. To obtain the total weight of the captured sediment, the mixture samples are poured through a filter with 30μm pores to capture the sediment, after which the filter with sediment is dried in an oven at 100°C for 24 hours on a large dish. Finally, the filter with sediment is weighed and the weight of the filter itself is subtracted, resulting in the total weight of the sediment in one sample. This analysis process is shown in Figure 4.7.

Figure 4.7: Niskin bottle samples analysis

The results from the ADV analysis and the Niskin bottle sample analysis are plotted together with the aimed concentration in the mixing tank per experiment in Figure 4.8. It can be seen that one Niskin bottle measurement is displayed slightly different, due to a significant high concentration, which should not be possible in a homogeneous mixture. The same goes for the other two ADV measurements that are displayed differently. The deviating ADV measurements can be explained by the possibility that the probes experienced reflection from a hose or one of the submersible pumps, influencing the acoustic signal. The accuracy of the measurements from both the ADV and the Niskin bottle concerning the aimed concentration in the mixing tank can be seen in Figure 4.9.

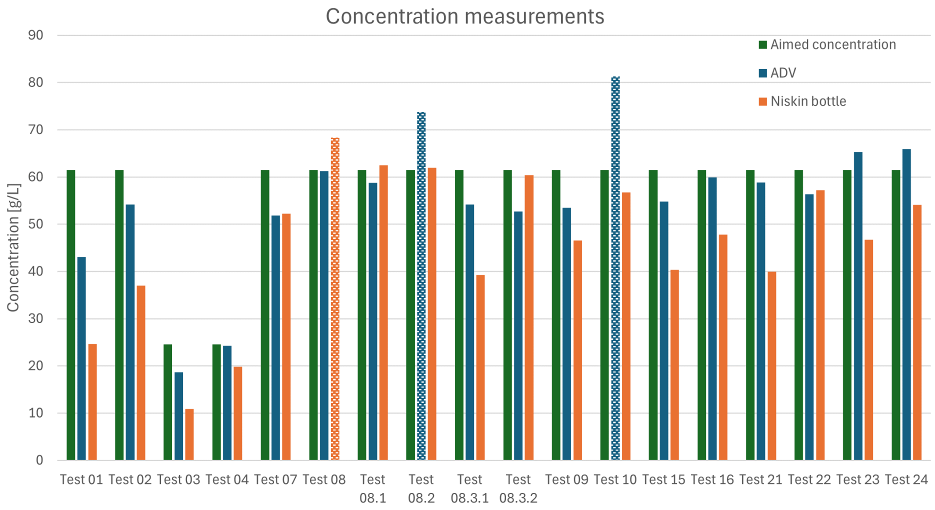

Figure 4.8: Concentration measurements in the mixing tank with the ADV and Niskin bottle samples

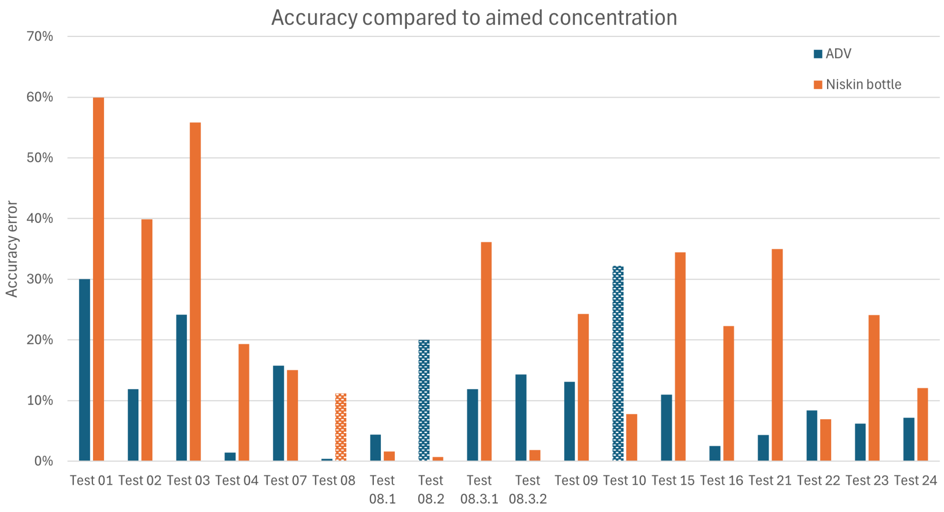

Figure 4.9: The relative error of the concentration measurements in the mixing tank concerning the aimed mixture concentration

The data from the ADV and raw data from the Niskin bottle samples from the mixing tank for all the experiments can be seen in Appendix D.

5 | Analysis and Discussion

This chapter describes the analysis (Section 5.1) and discussion (Section 5.2) of the results from the experiments.

5.1. Analysis

In this section, the results acquired from the experiments will be analyzed. Section 5.1.1 describes and analyses a phenomenon observed during the experiments, to answer the first research question on unwanted phenomena during the discharge or dispersion of a turbidity current, which is a buoyant plume and a bulge formation. Section 5.1.2 describes and analyses trends that have been found, to answer the second research question on the influence of the velocity ratio on the dispersion of a turbidity current. Section 5.1.3 describes and analyses trends that have been found, to answer the research objective on the influence of the slope angle and direction on the dispersion of a turbidity current, discharged from a moving source. Lastly, Section 5.1.4 describes a phenomenon that occurred once, by accident, a floating plume.

5.1.1. Bulge Formation

From the camera footage, a phenomenon has been observed that the turbidity current forms a bulge towards the diffuser from the impingement point at certain slope angles, when driving in the downhill direction. The bulge length is plotted against the slope angle in Figure 5.1.

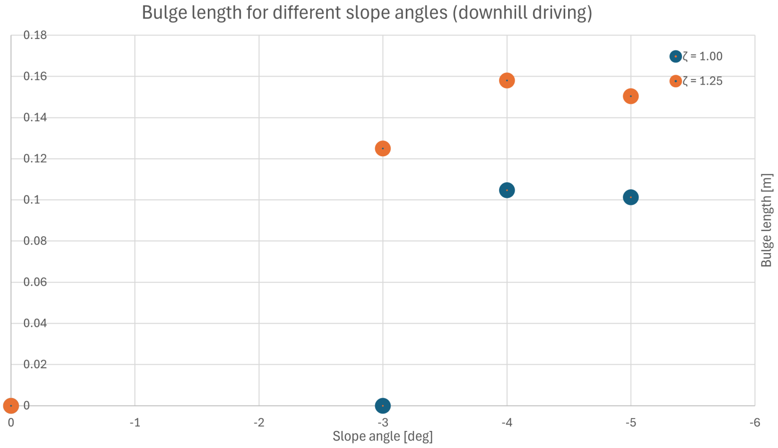

Figure 5.1: Bulge length for different slope angles for $\zeta = 1.00$ and $\zeta = 1.25$

It can be seen that for $\zeta = 1$, the bulge appears at a slope angle of 4° and remains for higher angles. However, when the velocity ratio is increased to 1.25, the bulge already appears at a slope angle of 3° and remains for higher angles. This is coherent with what is expected, because with a $\zeta > 1$, the source velocity is higher than the discharge velocity, meaning that the turbidity current is effectively discharged downhill, meaning that it would have a higher propensity to have a downhill impingement direction component.

This is also coherent with the trend that can be seen in the impingement angle for different slope angles. A larger impingement angle will result in a higher propensity to have an impingement direction downhill. This is confirmed by the data analysis from the side view footage, where the impingement angle for every experiment is determined. The relevant data is plotted in Figure 5.2.

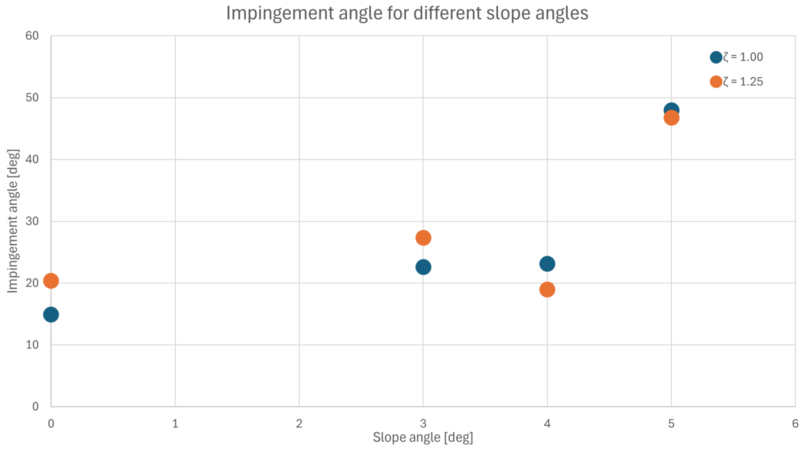

Figure 5.2: Impingement angle for different slope angles for $\zeta = 1.00$ and $\zeta = 1.25$

The general trend can be seen that for larger slope angles, the impingement angle is also larger. After discharge, the gravitational force pulls the current vertically down and is not influenced by the changing slope angle, while the measurement of the impingement angle rotates with the changing slope. This means that from a logical perspective, the impingement angle should increase when the slope angle is increased.

In addition to that, the trend has been found that for larger impingement angles, the dispersion angle is also larger. Figure 5.3 shows the dispersion angle plotted against the impingement angle. It can be seen that for higher dispersion angles, the impingement angle is higher on average. The trend is coherent with the trend that for a larger impingement angle, there is more propensity to form a bulge, because a larger dispersion angle also means that the turbidity current has a higher velocity component in the driving direction, which would also benefit the formation of a bulge.

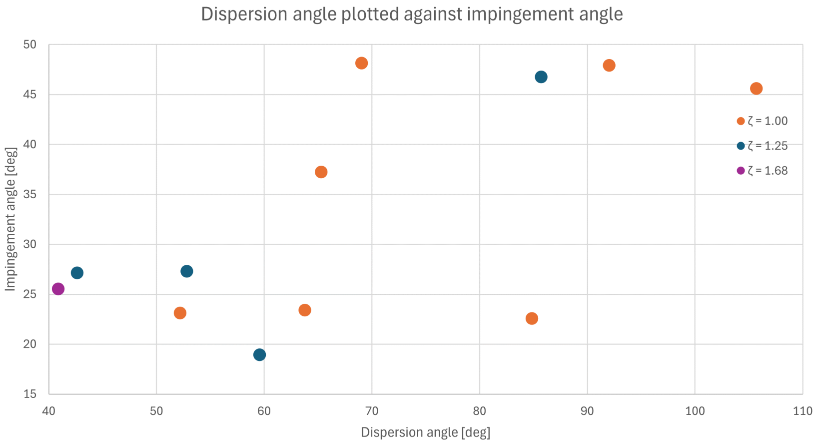

Figure 5.3: Dispersion angle plotted against impingement angle

The bulge formation is an unwanted phenomenon in deep-sea mining operations. When considering the experimental scale (1:20), a bulge length of 10 cm becomes 2 m in reality, which could potentially black out the sensors and cameras on the backside of the PNMT. Additionally, the interaction of the turbidity current bulge with the PNMT could lead to an increase in dispersion of the turbidity current.

5.1.2. Influence of the Velocity Ratio on the Dispersion

Downhill Driving Direction

By comparing similar experiments at different velocity ratios, the trend is found that for a higher velocity ratio, the dispersion velocity and the height of the turbidity current are greater, compared to the turbidity currents at lower velocity ratios. This is supported by comparing the UVP data from experiments 9 and 10, performed at a slope angle of 3°, experiments 15 and 16, performed at i = 4°, and experiments 7, 8 and 8.3.2, performed at i = 5°. The velocity profiles from these experiments are plotted in Figure 5.4.

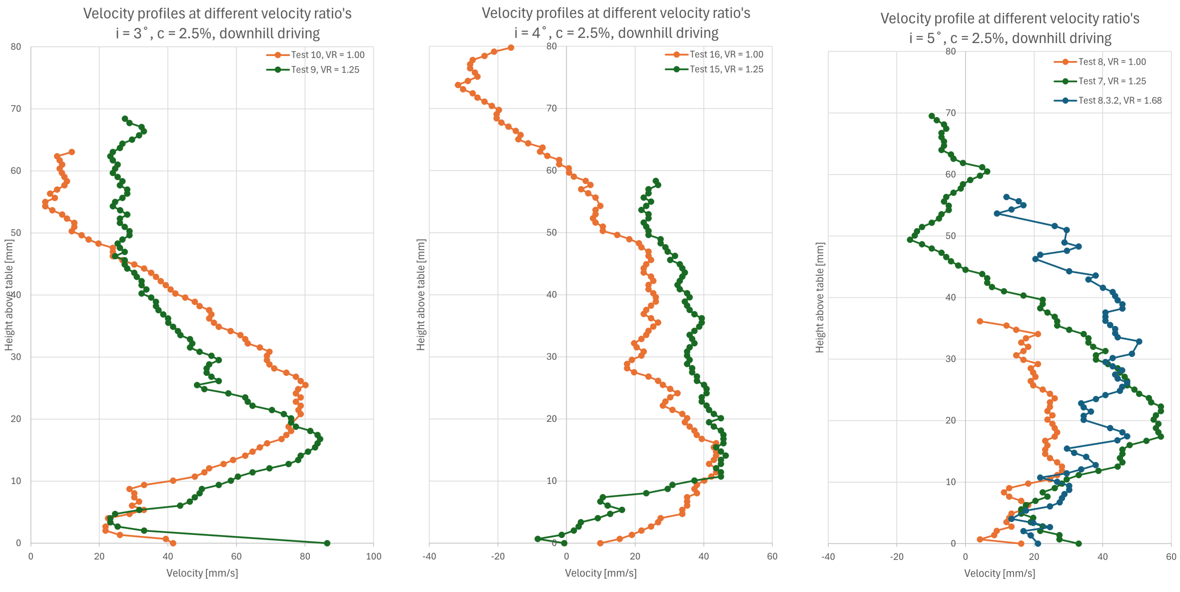

(a) i = 3° **(b)** i = 4° **(c)** i = 5°

Figure 5.4: Velocity profiles at different velocity ratios

Figure 5.4a plots the velocity profiles of experiments 9 and 10, performed at a slope angle of 3°. Experiment 10 is performed with $\zeta = 1.00$, experiment 9 with $\zeta = 1.25$. It can be seen that the maximum dispersion velocity is the highest for experiment 9, with a value of 84.4 $\frac{mm}{s}$, where it is 80.1 $\frac{mm}{s}$ for experiment 9. In addition to that, the height of the turbidity current is greater for experiment 9 than for experiment 10.

The maxima lay quite close to one another, but according to the concentration measurements that are done for experiments 9 and 10, as can be seen in Section 4.4, the mixture concentration of experiment 10 is relatively higher than that of experiment 9. As described in Section 2.3.5, an increase in concentration also means an increase in dispersion velocity, meaning that the difference in maximum dispersion velocity between experiments 9 and 10 would be greater when the concentrations are exactly the same.

Figure 5.4b shows the velocity profiles of similar experiments at a slope angle of 4 degrees, namely experiments 15 and 16, Experiment 16 is performed at $\zeta = 1.00$, and it can be seen that the maximum dispersion velocity is 43.6 $\frac{mm}{s}$, with a turbidity current height of 58.4 mm. Experiment 16 is compared to experiment 15, which is performed at $\zeta = 1.25$. Experiment 15 reaches a maximum dispersion velocity of 46.4 $\frac{mm}{s}$ with a turbidity current height of 58.4 mm. For experiment 16 the maximum dispersion velocity is 43.6 $\frac{mm}{s}$ with a turbidity current height of 60.4 mm.

Again, the maxima of the dispersion velocities lay close to each other, but again Section 4.4 shows that the measured mixture concentration of experiment 16 is higher than experiment 15. This means that the difference in maximum velocity between experiments 15 and 16 would be greater when the concentrations were exactly the same.

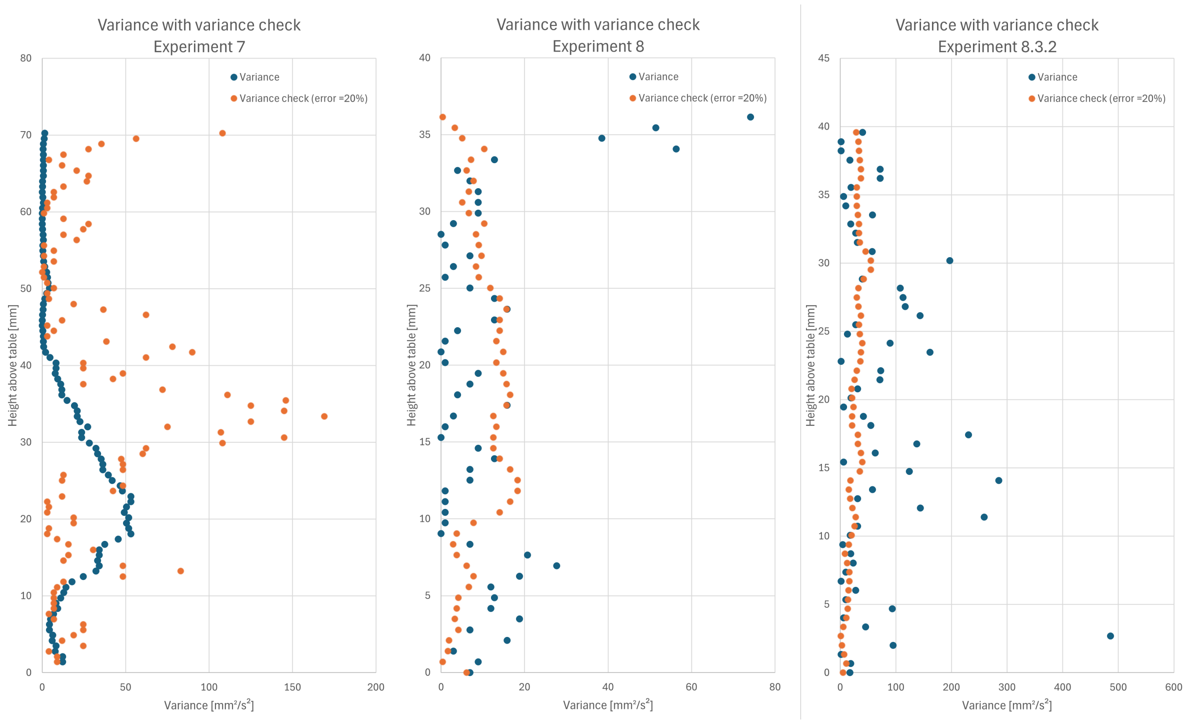

(a) Experiment 7 **(b)** Experiment 8 **(c)** Experiment 8.3.2

Figure 5.5: Variance and variance check from experiment 7, 8 and 8.3.2

Figure 5.4c shows the velocity profiles of similar experiments at a slope angle of 5 degrees, namely experiments 7, 8 and 8.3.2, with a variable velocity ratio. Experiment 8 is performed at $\zeta = 1.00$. It can be seen that the maximum dispersion velocity is 28.1 $\frac{mm}{s}$, with a turbidity current height of 36.2 mm. Experiment 7, performed at $\zeta = 1.25$, has a maximum dispersion velocity of 56.9 $\frac{mm}{s}$ and a turbidity current height of 44.5 mm. Lastly, experiment 8.3.2, performed at $\zeta = 1.68$, has a maximum dispersion velocity of 56.9 $\frac{mm}{s}$ and a turbidity current height of 56.3 mm. The same trend as in Figure 5.4a cannot be found immediately here. The data shows, when comparing experiment 7 with experiment 8.3.2, that for a higher velocity ratio, the maximum dispersion velocity decreases. However, when looking closely at the entire velocity profile of experiment 7 compared to experiment 8.3.2, the overall dispersion velocity of experiment 8.3.2 is higher than experiment 7, except in the peak. It therefore could be argued that, based on the other comparisons from Figure 5.4a and within Figure 5.4b, this is a deviation based on the sensitivity of the UVP transducers. To support this conclusion, the variance of the three experiments has been plotted in Figure 5.5. It can be seen that the variance of experiments 7 and 8 is relatively low and stable, unlike the variance of experiment 8.3.2, which is more capricious, especially when comparing the variance to the variance check. It can be concluded that the data from experiment 8.3.2 is less reliable. Note that a close look should be taken at the x-axis.

The observed trend is also supported by a trend that is described earlier in Section 5.1.1: for a higher velocity ratio, there is more propensity to form a bulge and due to the reduction of momentum in the discharge direction, there is also an increased dispersion of the turbidity current. It could also be argued that for a higher velocity ratio for a downhill driving direction, gravity has more time to exert its force on the flow before impingement, increasing the vertical momentum, and resulting in a more powerful impingement, which increases the dispersion of the turbidity current. An increase of the dispersion angle for higher velocity ratios is supported by both Figure 5.2 and Figure 5.3. Also, according to the trend in Section 5.1.3, a higher dispersion angle means a higher dispersion velocity and a greater height of the turbidity current. However, the vertical concentration distribution plays a role in obtaining a good insight into the turbidity current height, which was not measured during the experiments.

Uphill Driving Direction

In Figure 5.6, the slope angle has been plotted against the dispersion angle for the experiments with an uphill driving direction, for experiments with a velocity ratio of 1.00 and 1.25. It can be seen that for the experiments with a lower velocity ratio (experiments 22 and 24), the dispersion angle is higher than for the experiments with a higher velocity ratio (experiments 21 and 23). To verify this trend, the velocity profiles from the respective experiments have been plotted in Figure 5.7.

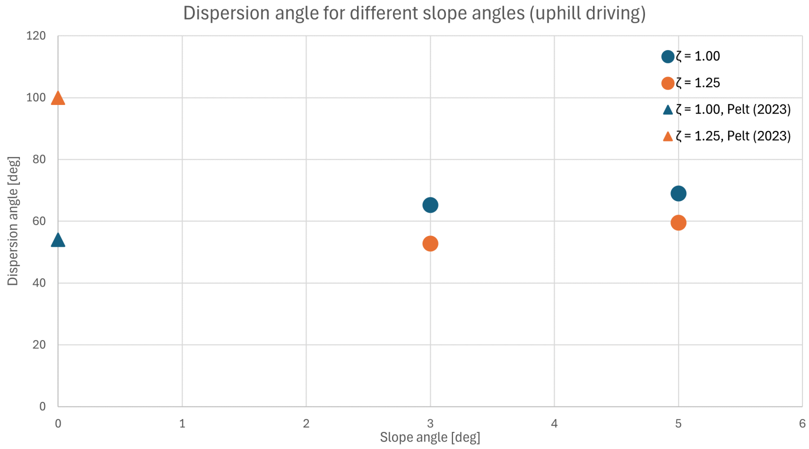

Figure 5.6: Dispersion angle at different slope angles for $\zeta = 1.00$ and $\zeta = 1.25$, driving in the uphill direction, with added data points from van Pelt (2023) [63]

The velocity profiles in Figure 5.7b support this trend. It can be seen that the maximum dispersion velocity (and therefore the dispersion angle) is greater for experiment 22 with $\zeta = 1.00$ than for experiment 21 with $\zeta = 1.25$. The maximum dispersion velocity for experiment 21 is 64 $\frac{mm}{s}$ and for experiment 22 it is 88.5 $\frac{mm}{s}$. However, Figure 5.7a does not diligently support this trend, because the maximum dispersion velocity from the velocity profiles from experiments 23 and 24 are nearing equal. There the maximum dispersion velocity for experiment 23 is 79.4 $\frac{mm}{s}$ and for experiment 24 it is 80.1 $\frac{mm}{s}$. The measured concentration for both experiments is very similar, so that does not give a reason why these values are so close to each other, while, according to the found trend, it is expected that they deviate more. It can also be seen from Figure 5.7b that the turbidity currents are the highest in the experiments with the higher velocity ratios.

The trend that can be seen in the influence of the velocity ratio on the dispersion of the turbidity current when driving uphill is the opposite of the trend that is found when driving downhill. The unusual finding is that here the turbidity currents with the lowest dispersion velocity have the greatest height. Again, the vertical concentration distribution plays a role in obtaining a good insight into the turbidity current height, which was not measured during the experiments.

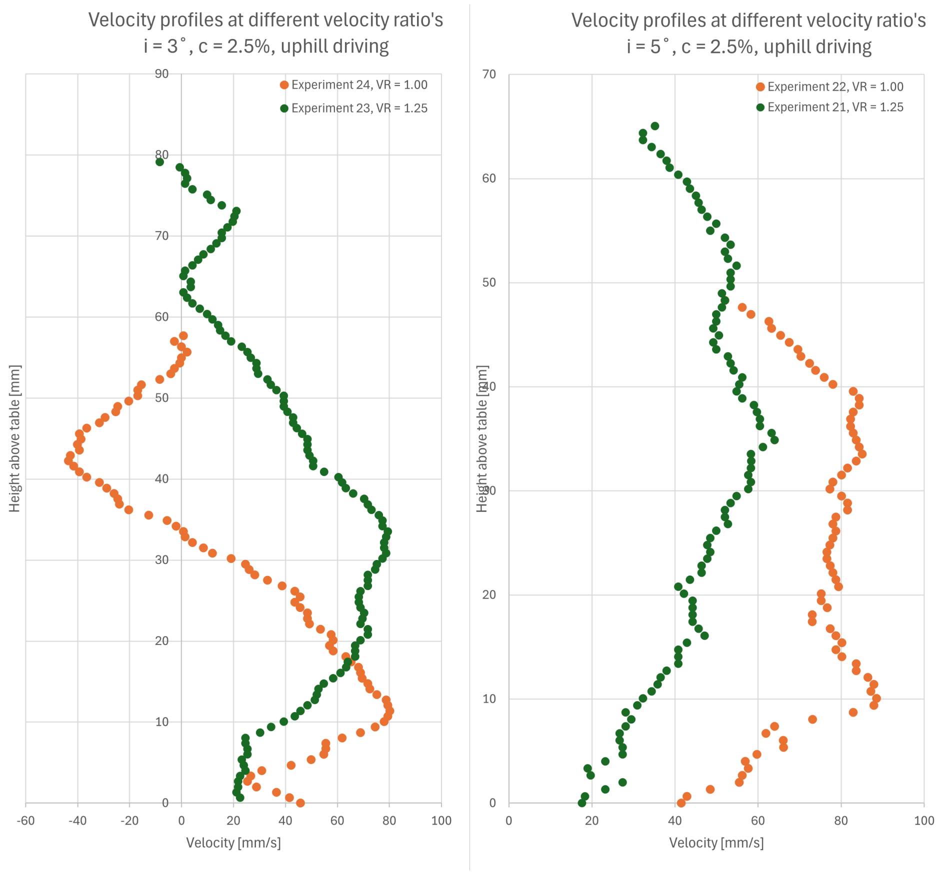

(a) $i = 3°$ **(b)** $i = 5°$

Figure 5.7: Velocity profiles at different velocity ratios for i = 3° and i = 5°, driving in the uphill direction

Trends

The trends that can be found for similar downhill driving experiments with a higher velocity ratio is that the turbidity current tends to have a higher dispersion velocity and the height tends to be increasing. The experiments are performed at the same source velocity, with a varying discharge velocity, where a higher velocity ratio means a lower discharge velocity.

For the uphill driving experiments, the inverse trend has been found that for a higher velocity ratio, the dispersion velocity is lower. However, it is found that for a higher velocity ratio, the turbidity current is higher, equal to the trend for downhill driving.

5.1.3. Influence of the Slope Angle on the Dispersion

An adapted Froude number has been calculated for the discharged plume. The original Froude number is calculated as per Equation (2.19), but with introducing a moving source and still having a discharge velocity, the original Froude number does not fully represent the correct momentum flux by only taking the discharge velocity into account. Therefore, a revised Froude number is calculated, as per

$$Fr_{revised} = \frac{v_{d}*}{\sqrt{g' * H}} \tag{5.1}$$

where $v_{d}*$ is the relative discharge velocity, calculated as per Equation (5.2) and H is the diffuser height.

$$v_{d}* = |v_d - v_s| \tag{5.2}$$

The revised Froude number of the discharged plumes, categorized per slope angle and direction, is plotted against the maximum dispersion velocity and can be seen in Figure 5.8. No specific trends or regime changes can be found for the different experiments.

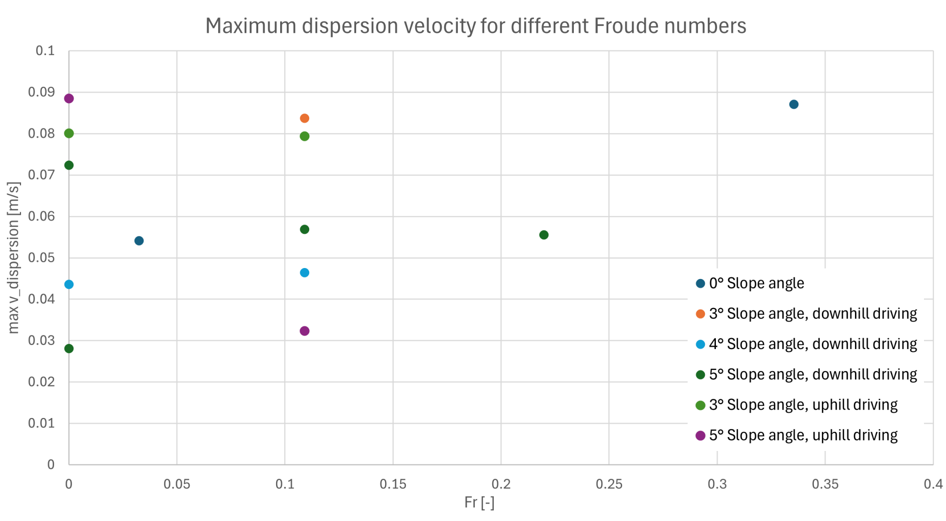

Figure 5.8: Froude number plotted against the maximum dispersion velocity, categorized per slope angle and direction

Downhill Driving Direction

A trend has been found in the relation between the slope angle and the dispersion of the turbidity current. Two different sets of experiments have been compared to each other, namely experiments 7, 9 and 15, performed at $\zeta = 1.0$, and experiments 8, 10 and 16, performed at $\zeta = 1.25$. The velocity profiles from these experiments are plotted in Figure 5.9.

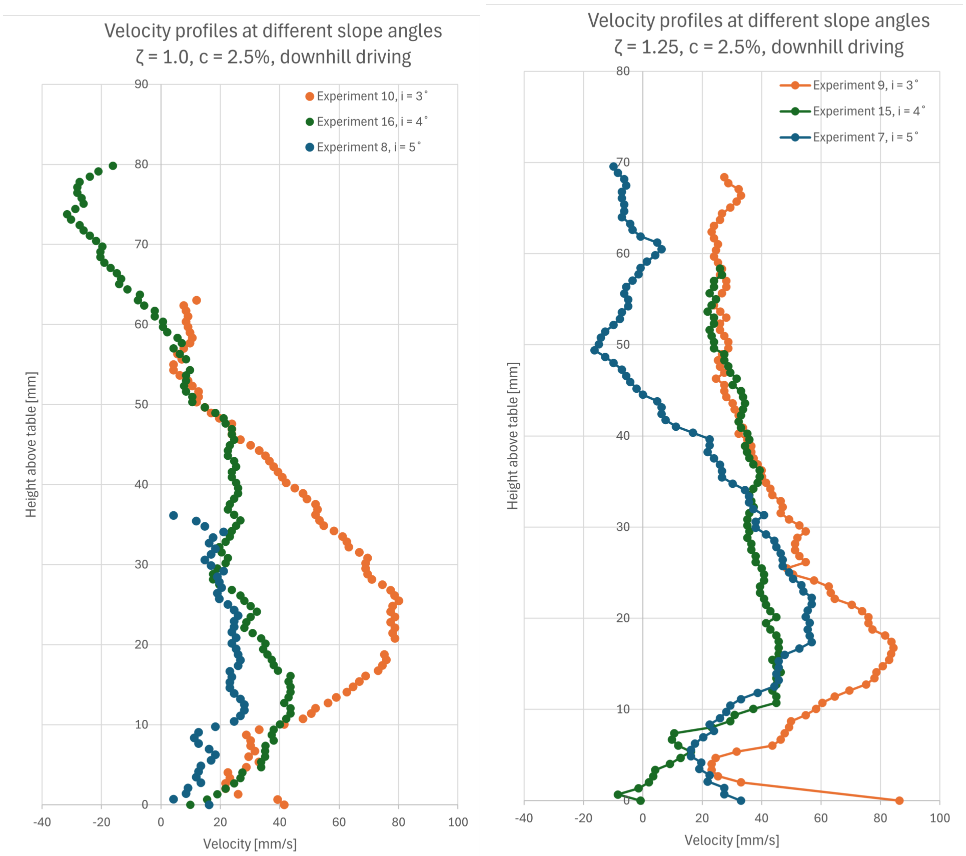

(a) ζ = 1.0 **(b)** ζ = 1.25

Figure 5.9: Velocity profiles at different slope angles for $\zeta = 1.00$ and $\zeta = 1.25$, driving in the downhill direction

In Figure 5.9a, it can be seen that for experiments with $\zeta = 1.0$ and a downhill driving direction, the maximum dispersion velocity is at experiment 10 (slope angle of 3°) with 80.1 $\frac{mm}{s}$. The maximum dispersion velocity at experiment 16 (slope angle of 4°) is 43.6 $\frac{mm}{s}$ and at experiment 8 (slope angle of 5°) it is 28.1 $\frac{mm}{s}$.

Similar results can be seen in Figure 5.9b. The figure shows that for experiments with $\zeta = 1.25$ and a downhill driving direction, the maximum dispersion velocity is at experiment 9 (slope angle of 3°) with 84.4 $\frac{mm}{s}$. The maximum dispersion velocity at experiment 15 (slope angle of 4°) is 46.4 $\frac{mm}{s}$ and at experiment 7 (slope angle of 5°) it is 56.9 $\frac{mm}{s}$.

Both plots conceal a trend that is not clearly visible at first glance; The maximum dispersion velocity reduces as the slope angle increases. This is both visible at Figure 5.9a and Figure 5.9b for the velocity profiles at 3° and 4° slope angle, but is more difficult to see when also looking at the velocity profile of experiment 7 at a 5° slope angle in Figure 5.9b. A UVP measurement is sensitive and a peak velocity is much more difficult to measure than an entire, averaged velocity profile. Therefore, the continuation of the trend in the experiments at the slope angle of 5° can be explained with the total dispersion velocity integral per velocity profile, which also decreases for an increasing slope angle, as can be seen in Figure 5.10. A closer look can be taken at the individual velocity profiles, focusing on the reliability of the data points as explained in Section 4.3, depicted in Appendix B.

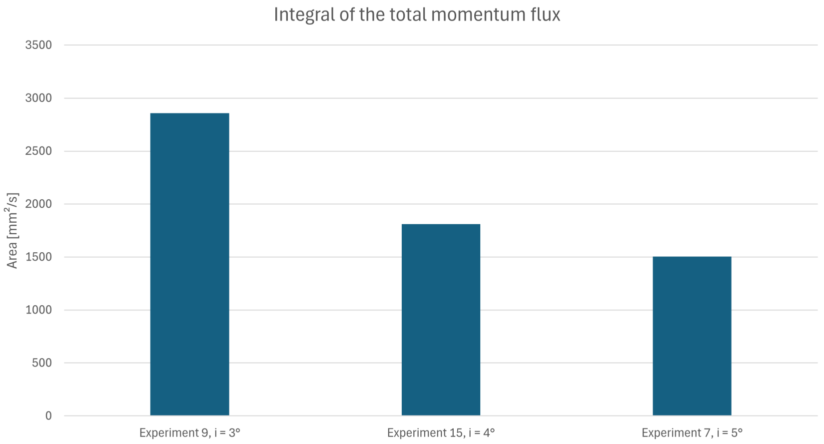

Figure 5.10: Integral of velocity profiles for experiments with a downhill driving direction at $\zeta = 1.25$

This can be further substantiated when plotting the dispersion angle against the slope angle for these six experiments, as can be seen in Figure 5.11. This plot also shows that the dispersion angles, obtained from the camera footage, for the experiments at a slope angle of 5° are relatively high. It is difficult to find the general trend within this plot, but when comparing the dispersion angle to the maximum velocity, it can be concluded that for a higher dispersion velocity, the dispersion angle is higher, which is to be expected.

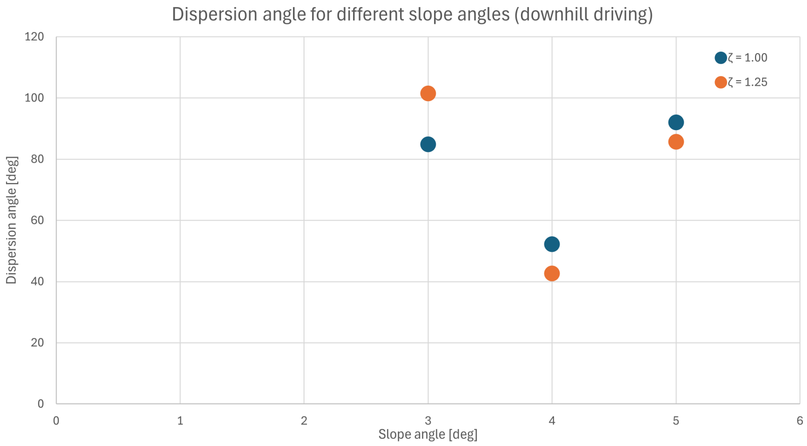

Figure 5.11: Dispersion angle at different slope angles for $\zeta = 1.00$ and $\zeta = 1.25$, driving in downhill direction

In addition to that, it can also be observed from Figure 5.9a that the turbidity current from experiment 10 (slope angle of 3°) is the highest, closely followed by the one from experiment 16 (slope angle of 4°). The reason this turbidity current is not seen as higher, even though the velocity profile is higher, is that it can be seen that the profile crosses the 0 velocity line at around 60 mm, effectively generating only vortices above that point. Experiment 8 (slope angle of 5°) shows to have the lowest turbidity current.

From Figure 5.9b, the same trend can be observed. It can be seen that the turbidity current from experiment 9 (slope angle of 3°) is the highest, closely followed by the turbidity current from experiment 15 (slope angle of 4°), which also follows the general shape of experiment 9 from 35 mm above the table upward. However, since the profile ends lower above the bed (at 58.4 mm versus 68.4 mm), it means that above 58.4 mm there was no consistent turbidity current anymore, most likely only vortexes. Experiment 7 (slope angle of 5°) shows to have the lowest turbidity current, ending at 45 mm with only vortexes above.

Uphill Driving Direction

It can be observed in Figure 5.6 that steeper slopes result in a slightly larger dispersion angle. This suggests an increase in dispersion velocity with steeper slope angles. However, when examining the velocity profiles from experiments conducted at a slope of 3° (experiment 22 and 24) and those at a 5° slope (experiment 21 and 23) shown in Figure 5.12, this trend is not consistently supported.

Figure 5.12a supports the trend, where experiment 24 at a 3° slope angle shows a maximum dispersion velocity of 80.1 $\frac{mm}{s}$, and experiment 22 at a 5° slope angle shows a maximum dispersion velocity of 88.5 $\frac{mm}{s}$. However, Figure 5.12b does not support the trend that for a steeper slope angle, the dispersion velocity is higher. Experiment 23 at a 3° slope angle has a maximum dispersion velocity of 79.4 $\frac{mm}{s}$, while experiment 21 at a 5° slope angle has a lower maximum dispersion velocity of 64 $\frac{mm}{s}$.

The measured concentration of the mixture from experiment 23, as can described in Section 4.4, is relatively higher than that of experiment 21. According to Section 2.3.5, this implies that the dispersion velocity is relatively higher due to the difference in concentration rather than due to the influence of the slope angle. However, this does not fully explain why the trend is not consistently observed in this analysis. Furthermore, the values of the integrals of the two velocity profiles are very close, as shown in Figure 5.13.

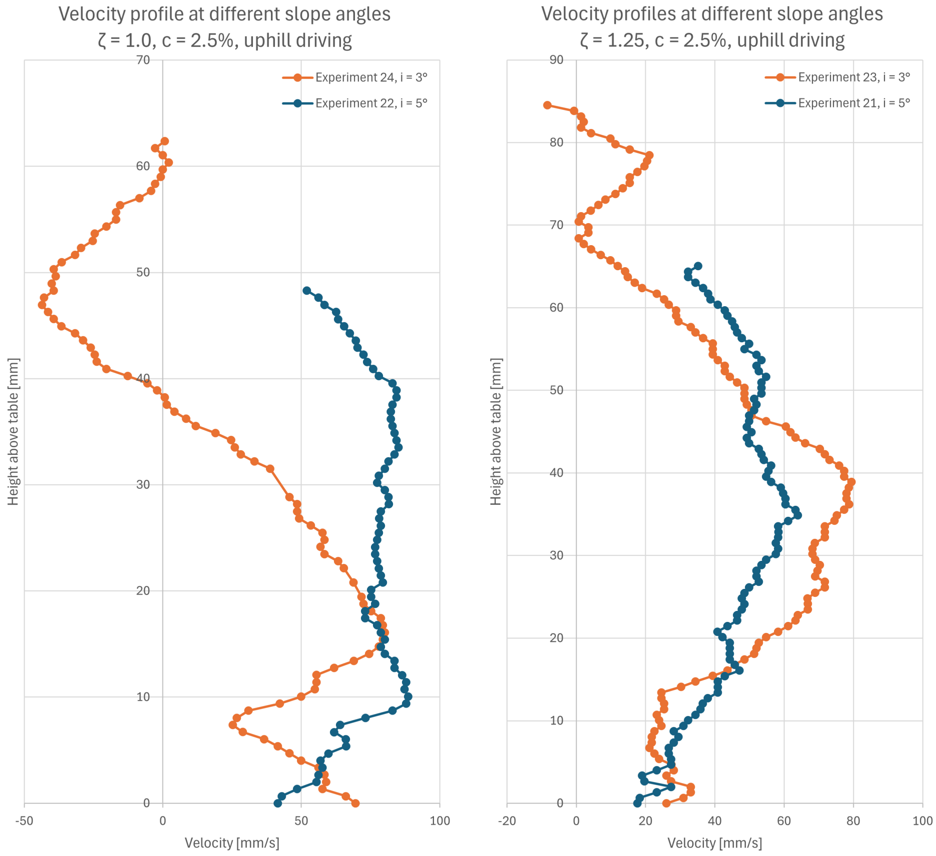

(a) $\zeta = 1.0$ **(b)** $\zeta = 1.25$

Figure 5.12: Velocity profiles at different slope angles for $\zeta = 1.00$ and $\zeta = 1.25$, driving in the uphill direction

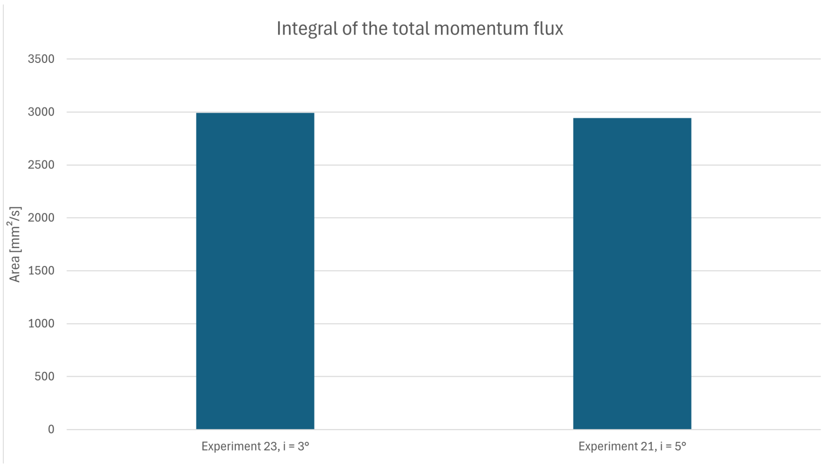

Figure 5.13: Integral of velocity profiles for experiments with an uphill driving direction at $\zeta = 1.25$

Trends

The two trends that can be seen for the downhill driving experiments are: a lower slope angle gives a higher dispersion velocity and greater turbidity current height and a higher dispersion angle gives a higher dispersion velocity. When putting these conclusions together, from reasoning it can then be concluded that for a lower slope angle, the dispersion angle is higher. This is a difficult trend to see in Figure 5.11, however, it is supported by and deducted from two different, clear trends.

For the uphill driving experiments, no conclusive trend can be found. It could be argued that, according to some of the data, for a steeper slope angle the dispersion velocity increases, however, this is both counter-intuitive and not supported by all the obtained data.

5.1.4. Floating Plume

An unusual phenomenon has been observed in experiment 8.3.1, where the discharged plume became buoyant. An image of this phenomenon can be seen in Figure 5.14.

Figure 5.14: Buoyant plume phenomenon

The velocity profile from experiment 8.3.1, as depicted in Figure 5.15, shows that the dispersion velocity is relatively low. Still, the height where the plume has its maximum dispersion velocity is much higher above the table than in other experiments. It is called a plume and not a turbidity current on purpose, because a turbidity current is gravity driven (Section 2.3.2). It can be seen from Figure 5.14 that the plume is buoyant and does not settle. The velocity profile with corresponding variance can be seen in Figure 5.15. It can be seen from the velocity profile that the plume does not have the characteristic form of a turbidity current, supporting the claim that the plume is buoyant.

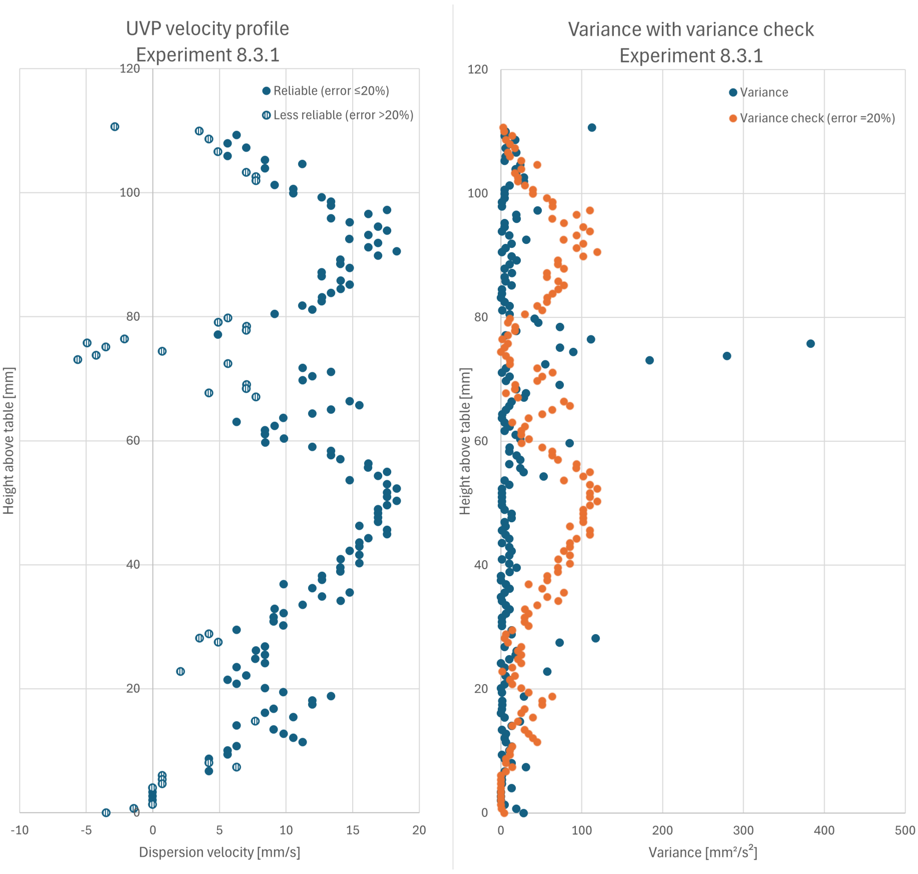

Figure 5.15: Velocity profile with variance and variance check plot from experiment 8.3.1

From the ADV measurement, the mixture concentration is found to be 54.2 $\frac{g}{L}$, with the actual desired concentration to be at 61.5 $\frac{g}{L}$. However, the Niskin bottle sample that was taken gives a lower concentration, 39.29 $\frac{g}{L}$, which is a 36% deviation from the aimed concentration of 61.5 $\frac{g}{L}$. It is possible that the Niskin bottle sample is taken in a not fully homogeneous mixture or that a small amount of material was lost during the sample analysis at Deltares. However, this (appearing) reduction in concentration in the discharged plume does still not give a satisfactory explanation of how the plume can behave buoyant, since there is still a considerable density difference.

Additionally, there was also a difference in the temperature of the discharged mixture and the ambient water. According to the temperature measurements just before performing the experiment, the temperature of the (ambient) water in the flume was 19.3 °C and the mixture temperature in the mixing tank was 42.1 °C. The latter is extremely high, which was due to a mistake of leaving the submersible pumps in the mixing tank on during the waiting time between the two experiments. If four pumps in a small tank just pump water around, all the energy (eventually) converts to heat. This means that four pumps with 750 W power output each are a heater of 3 kW. The density of water at 19°C is 998.36 $\frac{kg}{m^3}$ and for water with a temperature of 42°C it is 991.39 $\frac{kg}{m^3}$ [17]. This is a reduction in density by 6.97 $\frac{kg}{m^3}$.

When combining the data from the Niskin bottle sample (worst case scenario) and the increase in temperature, the density of the plume adds up to 1030.68 $\frac{g}{L}$ or $\frac{kg}{m^3}$, still over 30 $\frac{kg}{m^3}$ denser than the density of the ambient water. It is expected that such a density difference results in a turbidity current, so no satisfactory argumentation has been found in the density difference between the plume and the ambient fluid on why this plume is buoyant and does not settle.

The correct perspective might be found by considering the Froude number as defined by Rotzien *et al.* (2022) [68], calculated as per Equation (5.3). Due to the high temperature of the mixture, the viscosity also reduces, which influences the Froude number of the plume. As described in Section 2.3.3, the Froude number is an indication for the dominating factor (either wake turbulence or buoyancy) of the initial flow after discharge and for lower Froude numbers, the impingement length increases, as described in Section 2.3.7. This case must have passed the point where there is still an impingement point for the plume on the bed, resulting in a floating plume, which is mostly buoyancy-driven.

$$Fr = \frac{\mu}{\sqrt{g \cdot L}}, \tag{5.3}$$

where μ is viscosity, g is gravity and L is length.
Van Pelt (2023) mentioned in his conclusions that a higher discharge velocity could result in a floating (or buoyant) plume [63]. However, no deviation from the intended volume flux of the mixture is measured by the flowmeter, meaning that the actual discharge velocity was equal to the intended discharge velocity. The floating plume is labeled as an unwanted phenomenon, because a non-settling plume will disperse more overall, increasing the affected area by the sediment dispersion.

5.2. Discussion

In this paragraph, the assumptions (Section 5.2.1), measurements (Section 5.2.2) and conclusions (Section 5.2.3) of this research are discussed.

5.2.1. Assumptions

Mixture Composition

The mixture discharged through the diffuser in the flume consists of glass beads suspended in water. These glass beads have a diameter range of 40-70 µm, with a median diameter (d50) of 55 µm and a density of 2,460 $\frac{kg}{m^3}$. This is similar, though not identical, to the silt fraction (76.2%) within the CCZ sediment, which has a diameter range of 2-63 μm. A smaller portion (11.8%) of the CCZ sediment consists of coarser material, primarily sand, with a diameter range of 63-2000 μm. The remaining 12% CCZ sediment is composed of clay, with a diameter below 2 μm, which is the key difference between glass beads and CCZ sediment.

Clay particles can adhere to each other, forming larger aggregates through a process known as flocculation, which increases the effective particle diameter and settling speed. Flocculation is challenging to observe, and research on this phenomenon is still emerging. To eliminate the effects of flocculation, glass beads were chosen as the material for the mixture, since they would settle faster, thus hastening the subsequent experiments. Additionally to that, it also eliminates the task of frequent water changes in the flume. However, this decision reduces the resemblance between the turbidity current behaviour in the experimental setup and real-world conditions.

Ambient Water

Freshwater was used during the experiments instead of saltwater due to the corrosive nature of saltwater, which the flume and equipment were not designed to handle. The salt ions in salt water promote flocculation, with the help of organic matter. It binds mineral particles together, which in turn leads to faster settling of suspended materials. However, because glass beads were used instead of sediment and freshwater instead of saltwater, this effect was not present during the experiments.

Seabed

In the experimental setup, the seabed is simulated using a smooth, hard surface by suspending a table under the rails. This differs from the actual seabed in the CCZ, where the top layer consists of soft sediment. This simplification was made because it is difficult to replicate the properties of a natural seabed, especially at the scale of the experimental setup. This simplification affects the behaviour of the generated turbidity current. A smooth surface generates less shear on the turbidity current, resulting in less resistance and thus less deceleration. On the other hand, without loose sediment, the turbidity current cannot pick up additional sediment through shearing, which could increase its horizontal momentum and dispersion velocity.

5.2.2. Measurements

UVP Velocity Profiles

The dispersion velocity of the turbidity current generated during the experiments was measured using an Ultrasonic Velocity Profiler (UVP). The UVP is highly sensitive to the concentration and velocity of the mixture, requiring an average of multiple consecutive velocity profiles to obtain a reliable measurement. The UVP has a narrow operational window for generating accurate velocity profiles, which occurs when the nose of the turbidity current passes in front of the transducer. Since the UVP produces a profile every decisecond, these profiles differ as the current moves through, so averaging them does not provide an exact representation of the current's velocity profile.

Moreover, the UVP transducer must be tilted at an optimal angle (found to be 25°) to avoid detecting reflective acoustic waves from the bed, which would introduce noise. This tilting causes the velocity profile to shift horizontally. Over a height of 25 cm, the profile moves 9 cm horizontally (calculated as $sin(25°) * 25cm$). Most velocity profiles measured during the experiments show good quality, with variances within a 20% error margin. However, this does not account for the tilt, which is only corrected by adjusting the vertical height using $cos(25°)$.

Appendix C contains the UVP profiles, accompanied by variance plots and checks that indicate the reliability of the data points. It shows that in many experiments some of the turbidity current velocity profile data points are less reliable, as they exceed the 20% error threshold. While less reliable points at the top or bottom of the turbidity current are less critical, the data points near the maximum dispersion velocity must be reliable for identifying trends and drawing conclusions.

Concentration Measurements

The Acoustic Doppler Velocimeter (ADV) is a highly sensitive device, primarily designed for measuring velocity profiles. Through calibration, a correlation between the signal-to-noise ratio (SNR) and concentration was established, allowing concentration measurements to be taken. However, due to the device's sensitivity and the relatively flat calibration curve within the specific concentration range and with this specific particle type, measurement errors can be significant, even when averaging data over a longer duration.

The ADV is also susceptible to interference from reflective acoustic waves off the walls and bottom of the mixing tank, as well as from equipment such as pumps and hoses. This can lead to less accurate SNR profiles, affecting concentration measurements. To ensure reliability, concentration measurements were backed up using Niskin bottle sampling. Although this method provides a snapshot rather than an averaged measurement, it is a more robust and foolproof way of measuring. Analysis of the Niskin bottle samples revealed small traces of algae growth, which slightly compromised the reliability of the samples by increasing the total solid mass. However, the comparison between the Niskin samples and ADV measurements showed good agreement, validating the use of ADV measurements, despite their inherent error, as the most reliable option for instantaneous feedback.

Cart Velocity Input

The cart velocity input is controlled by a turning knob, which does not directly indicate velocity but rather a proportion of the power input. Therefore, two conversion steps are required to convert the input value into the actual cart velocity: from the input value to the power input, and from the power input to the cart velocity. As a result, new calibrations had to be performed for each set of experimental conditions to determine the cart velocity accurately.

Due to the imprecise nature of the turning knob, it was challenging to set an exact value, as there was no digital feedback. The cart's velocity was determined by timing its movement over a known distance along the rails, which introduced potential errors due to manual timing. It is possible that an error of up to 0.5 seconds occurred at both the start and end of timing and in combination with the time required for the cart to reach its intended velocity, this could result in a total error of up to 2 seconds in a 40-second experiment, leading to a possible velocity input error of around 5%. This margin of error could potentially result in an incorrect velocity ratio being assumed for certain experiments. This would have a minor effect on the data analysis, however, the general conclusions would remain the same.

Water Disturbances

Between experiments, the table was cleaned using a wet vacuum cleaner, which was a time-consuming and labour-intensive process that caused significant disturbance to the water in the flume. Additionally, when changing the slope angle or driving direction, a new cart velocity calibration test was required, which also introduced turbulence into the water. These disturbances necessitated a waiting period between processes and the next experiment to allow the water to settle, assuming that within several hours the water turbulence would return to near-zero levels.

However, no turbulence measurements were taken before starting new experiments, so it is possible that the water still was turbulent when starting an experiment, influencing the dispersion of the turbidity current. The extent of this influence is unknown and practically impossible to correct for.

Source Velocities

It was observed that high source velocities reduced the quality of the measurements. Practical limitations of the setup caused significant vibration in the cart and diffuser when the cart was driven at high velocity, resulting in shaky camera footage and uneven discharge of the mixture through the diffuser. These effects impacted the UVP measurements, especially in experiments 1, 2, and 8.1. Consequently, the data from these experiments are considered less reliable compared to similar experiments conducted at lower source velocities.

5.2.3. Analysis

General

A key advantage of using a larger experimental setup is the ability to perform integrated experiments that account for multiple interacting factors. However, this size also introduces challenges, such as an increased risk of external influences beyond the intended variables. Combined with sensitive instruments like the ADV and UVP, obtaining fully coherent data proves challenging. This makes it difficult to identify trends, particularly when the differences between experiments are small.

Bulge Formation

Like the floating plume, the experimental matrix was not designed to investigate the causes and conditions for bulge formation, resulting in limited data. However, bulge formation was more consistently observed across different experiments compared to the floating plume. This consistency allowed for the identification of general trends, providing some insight into potential causes.

Bulge formation has been described in simulations by Ouillon *et al.* (2021), who identified a regime between sub-critical and supercritical flow where certain input parameters cause the turbidity current to move ahead of the discharge towards the diffuser [59]. Their study, however, was conducted on a flatbed, so it is possible that similar parameters were mimicked in this study by introducing a sloping bed. Alternatively, the slope itself may be a direct cause of the bulge formation, bypassing the need for specific input parameters.

Floating Plume

The floating plume phenomenon was observed in a single experiment, which was not designed to investigate this occurrence. Consequently, the experimental matrix did not include parameters specifically tailored to explore the causes and conditions under which a floating plume forms, other than the difference in temperature between the flume and mixing tank. Therefore, the available data is limited, and conclusions drawn are speculative. The analysis mainly suggests the temperature difference is a potential explanation for the phenomenon.

The floating plume has been discussed in literature by Van Pelt (2023), who attributed it to a disproportionately high discharge velocity [63]. However, this was ruled out as a cause in the current experiment, since the discharge velocity (and velocity ratio) were consistent with other experiments that did not produce a floating plume.

Influence of the Velocity Ratio

The trend that has been found from the data analysis regarding the influence of the velocity ratio on the sideways dispersion of the turbidity current differs from expectations. While the separate effects of discharge velocity and source velocity have been studied on flat surfaces, their combined effect as a ratio on a sloping bed has not been thoroughly analyzed.

The observed trend deviates from those described in the literature review (Section 2.5). However, no studies in the literature combine a moving source with a sloping bed, which could explain the divergence. The coherence of the data suggests that the observed trend is reliable, potentially indicating that the slope introduces a new flow regime.

Numerical simulations by Elerian (2023) produced two runs (1 and 2) that show the trend observed in this study's downhill driving experiments, where a higher velocity ratio resulted in higher dispersion velocity. However, no conclusive explanation was provided for this behaviour, as other parameters remained consistent across the runs. The primary deviation was the higher source (PNMT) velocity of 0.5 $\frac{m}{s}$ compared to 0.25 $\frac{m}{s}$. Elerian recommended additional simulations with lower source velocities to determine whether the source velocity is a significant factor in triggering this unusual behaviour.

The Froude number used by Elerian to classify the runs is the ratio of momentum flux to buoyancy in a plume. However, only the discharge velocity was used to calculate the momentum flux, rather than the relative discharge velocity (v_d*), calculated as per Equation (5.2). When plotting the revised Froude number (as per Equation (5.1)) in the data analysis, runs 1 and 8 both have a Froude number of 0 and show closely matched velocity profiles, despite a twofold difference in source and discharge velocities. These two runs were not initially analysed together due to their different Froude numbers (1.75 and 1.24, respectively). The results are plotted in Figure 5.16, where the maximum sideways dispersion velocity was determined from the numerical run velocity profiles.

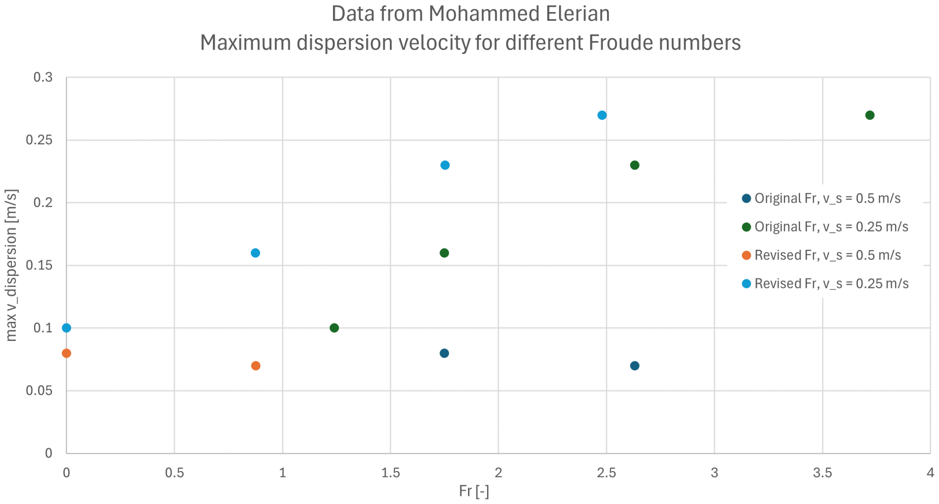

Figure 5.16: Data from M. Elerian, with Froude number revision [23]

For the numerical simulations, it is observed that with a higher source velocity of 0.5 $\frac{m}{s}$, the dispersion velocity decreases slightly as the Froude number increases. In contrast, for simulations with a lower source velocity of 0.25 $\frac{m}{s}$, the dispersion velocity increases with higher Froude numbers. This supports the hypothesis that source velocity influences the dispersion velocity of the turbidity current, considering an equal velocity ratio

In this research, most experiments were conducted with a source velocity of 0.067 $\frac{m}{s}$ at a scale of 1:20. This translates to a real-world source velocity of approximately 0.3 $\frac{m}{s}$, which falls within the range identified by Elerian (2023) where a change in trend (probably due to source velocity) is observed. Consequently, the trend indicating that a higher velocity ratio results in a higher dispersion velocity during downhill driving is considered more reliable.

Influence of the Slope Angle and Direction

Remarkably, no coherent trend can be found in the plot with the Froude number from all the experiments, separated by slope angle and direction, as per Figure 5.8. The Froude number is calculated based on input parameters, so this is not affected by any influences during the performance of the experiments. Because no trend can be seen in this plot, it suggests that the plume or turbidity current is not dominated by buoyancy flux or momentum flux, but an external factor, the sloping bed.

The trends that have been found in the data from the downhill driving experiments are both logical and clearly visible in the data and are supported by the literature. However, the findings in the literature are never based on data from experiments with both a moving source and a sloping bed.

No trend could be found in the data from the uphill driving experiments. From a logical perspective, it is expected that the same trend applies to the uphill experiments as to the downhill experiments. The effects of the slope will increase the gravitational effects on the turbidity current, giving it more propensity to flow downhill instead of disperse sideways. It might be possible that due to the lack of an abundance of measurements, no actual trends can be found. A single deviating velocity profile already compromises the analysis.

6 | Conclusions and Recommendations

6.1. Conclusions

In this section, the conclusions of the data analysis, as described in Section 5.1, are given. These conclusions are brief and to the point and answer the questions and the objective of this research.

6.1.1. Research Question - Unwanted Phenomena

The research question on the unwanted phenomena during the discharge or dispersion of a plume reads as follows: *When do unwanted phenomena occur during the discharge or near-field dispersion of a turbidity current on a sloping seabed from a moving source?*

During the experiments, two different phenomena have been identified to be unwanted during the discharge or dispersion of a mixture in an ambient fluid, which is the formation of a bulge and a floating plume.

Bulge Formation

During experiments with steeper slope angles and a downhill driving direction, it was observed that the turbidity current forms a bulge at the impingement point in the direction of the diffuser. Based on the data obtained from these experiments, it can be concluded that both a higher velocity ratio and a steeper slope angle positively influence bulge formation. The data shows that for a velocity ratio (ζ) of 1.00, the bulge appears at a slope angle of 4°, while for $\zeta = 1.25$, the bulge already appears at a slope angle of 3°.

Additionally, it was found that a steeper slope angle results in a higher impingement angle, which in turn shortens the impingement length. This leads to more concentrated impingement directed toward the diffuser, contributing to the formation of the bulge.

These conclusions are drawn from the analysis of combined data from the UVP, camera footage, and concentration measurements, as described in Section 5.2.

Floating Plume

During an experiment with an unintentional deviation in configuration, a floating plume was observed. Based on the data obtained from the measurements, it can be concluded that this behaviour was most likely caused by a significant temperature difference between the mixture and the ambient fluid, where the mixture had a considerably higher temperature. This temperature difference prevented the discharged plume from settling and forming a turbidity current, causing it to remain buoyant, similar to an actual sediment plume.

The higher temperature reduced the density of the mixture and lowered the Froude number, both of which decreased the tendency of the plume to settle. Similarly, Van Pelt (2023) also concluded that a discharged plume could remain buoyant if the horizontal momentum during discharge is too high, which effectively means that when the discharge velocity is too high, the velocity ratio becomes too low [63].

This conclusion is supported by the combined analysis of data from the UVP, camera footage, and concentration measurements, as described in Section 5.1.4.

6.1.2. Research Question - Influence of the Velocity Ratio

The research question on the influence of the velocity ratio on the spread of a turbidity current is as follows: *How will the ratio of source velocity over discharge velocity influence the near-field sideways dispersion of a turbidity current on a slope?*

Based on experiments performed with similar configurations for a downhill driving direction, but with varying slope angles and velocity ratios, it can be concluded that a higher velocity ratio results in a larger dispersion angle and a greater turbidity current height. A higher velocity ratio is defined as a reduction in discharge velocity while maintaining the same source velocity. Additionally, it was found that a larger dispersion angle corresponds to a higher dispersion velocity.

For experiments performed with a similar configuration in an uphill driving direction, an inverse trend was observed. Specifically, for a higher velocity ratio, the dispersion angle was smaller, resulting in a lower dispersion velocity. However, it was also found that, as in the downhill experiments, a higher velocity ratio led to an increase in turbidity current height.

These conclusions are drawn from the analysis of combined data from the UVP, camera footage, and concentration measurements, as described in Section 5.1.2.

6.1.3. Research Objective - Influence of the Slope Angle and Direction

The objective of this research is stated as follows: *"Determine the influence of a slope angle and slope direction on the near-field dispersion of a turbidity current, discharged from a moving source.*

Based on the experiments conducted, for the downhill driving direction, it can be concluded that as the slope becomes steeper, the dispersion angle, dispersion velocity, and the height of the turbidity current decrease.

For experiments conducted with a similar configuration but with an uphill driving direction, no conclusive trend was identified in the data. While some data suggest that the dispersion velocity increases with a steeper slope angle, this observation is counter-intuitive and is not consistently supported by all the obtained data.

These conclusions are drawn from the analysis of combined data from the UVP, camera footage, and concentration measurements, as described in Section 5.1.3.

6.2. Recommendations

In this chapter, recommendations are given for future research (Section 6.2.1), for practical improvements on the experimental setup or methodology (Section 6.2.2) and on the application of the results of this research for full-scale deep-sea mining (Section 6.2.3).

6.2.1. Future research

This paragraph will describe the recommendations for future research, which is the influence of concentration (Section 6.2.1), reducing the source velocity (Section 6.2.1), performing experiments on smaller scale (Section 6.2.1), the floating plume (Section 6.2.1), the bulge formation (Section 6.2.1) and doing experiments with real CCZ sediment in salt water (Section 6.2.1).

Floating Plume

During one experiment, a floating (buoyant) plume has been observed. This phenomenon was not expected or intended, so the experimental matrix was not designed to zoom in on the causes. The data from the singular experimental run has been analyzed and some possible causes have been identified. However, due to a lack of data, no specific parameter ranges have been identified that would cause a floating plume. It is important to know, because (it is expected that) a floating plume disperses more than a turbidity current. Therefore, additional research is required to find these parameter ranges.

Bulge Formation

During the experiments, the phenomenon of bulge formation has been observed. Again, the experimental matrix was not designed to zoom in on the causes of the bulge formation, so additional research is required to observe the behaviour of the bulge and find the parameters that influence the bulge formation. Because the bulge has been observed in multiple experimental runs, a foundation has been laid for the causes of the bulge formation, however, this is merely a nudge into the (presumed) right direction.

Influence of the Concentration

Due to complications during the experiments, the intended experiments that should give insight into the influence of the concentration of a plume on the dispersion of a turbidity current could not be performed. For future research, it is recommended that experiments should be conducted with an experimental matrix as such, that the influence of the concentration on the dispersion of a turbidity current, discharged from a moving source on a sloping bed can be determined.

The concentration is one of the parameters in deep-sea mining that can be taken into account in the design of the collector vehicle. Outside of the deep-sea mining Branch, the concentration is something that can often be altered, based on the effects that concentration has on the behaviour of the plume or turbidity current.

It is also recommended to perform measurements within the turbidity current, to gain more insight into the influence of concentration within the near-field plume on the dispersion of the turbidity current, other than just as an input parameter.

Low Source Velocity

It can be seen from the conclusions of the influence of the velocity ratio on the dispersion (Section 6.1.2) that the source velocity that is used in the experiments seems to be in a different, unusual regime, which was already found by Elerian (2023) [23]. It is recommended to repeat some of the experiments from this research, with a equal velocity ratio, but slower source and discharge velocity. It is expected that the mainstream trend will be found, that for a higher velocity ratio, the dispersion velocity will be lower.

Smaller Scale

The experimental setup that is used in this research is quite a large-scale setup. This means that multiple variables can be integrated into a bigger experiment, however, it is also much more susceptible to error or deviations. It is therefore recommended to do similar experiments at a smaller, more manageable scale. This should result in more qualitative results, further substantiating and shaping the trends that have been found and building the trends that could not be found.

Real CCZ Sediment with Salt Water

During these experiments, glass beads are used to create a mixture, other than real CCZ sediment, for reasons that are described in Section 3.4.1. This is an assumption that detracts from reality, so it is important to know how a mixture with actual CCZ sediment would behave. A smaller, more easy to handle setup should be used for this, because it is expected that the water would cloud a lot more due to some very small particles.

In addition to that, the water in the setup when using real CCZ sediment should be salt, to both mimic the concentration difference better and to mimic the flocculation process the most realistic.

6.2.2. Practical Improvements

This paragraph will give recommendations on practical improvements on the used experimental setup or similar experimental setups, to increase consistency and quality of the results. These are on the mixing tank (Section 6.2.2), removing air from the system (Section 6.2.2), the input of the cart velocity (Section 6.2.2), combat algae growth (Section 6.2.2) and altering the velocity ratio (Section 6.2.2).

Mixing Tank

Sediment in Suspension

It is recommended to use a mixing tank that has the least possible corners. It has been found that a lot of sediment accumulation will take place, which is very difficult to get and keep into suspension. The ideal shape of a mixing tank would be a drum.

Temperature Management

As described in Section 5.1.4, it has been found that the temperature of the mixture can rise surprisingly fast when the mixture is kept in suspense by four submersible pumps. It is therefore recommended to let the submersible pumps only run during the actual experiments and let the mixture settle after. To get the sediment back into suspension again, it is recommended to use both the submersible pumps and backflow hose from one of the pumps or a broom to wash over the bottom of the tank to reach all the sediment.

ADV Measurements

It is found that the ADV measurement is very sensitive to the reflection of the acoustic waves. To make sure that a reliable concentration measurement is done in the mixing tank, it is recommended to put it as far away as possible from the walls, the submersible pumps and possible backflow hose.

Flooding

When finishing an experiment, it is strongly advised to make sure that all valves in the system between the mixing tank and flume are closed. When all pumps are shut off, a siphoning effect will come into effect, because the water level in the flume is much higher than in the mixing tank, which will flood the mixing tank. This is found out the hard way.

Air Removal

It was found, during the experiments, that air slips into the system when exchanging the diffuser or the hoses, accumulating at the highest point of the system. This results in air bubbles during discharging, influencing the outflow. It is therefore recommended to put a small valve on the highest point of the hoses in the setup, to release the air in the system just before the start of the experiment, and to make sure that the mixture is pumped through the diffuser without any air.

Cart Velocity Input

At this point, the cart is operated by a rotary value knob for velocity input, as described in Section 3.1.1. As this gives no real-time feedback on the velocity of the cart, this is very inaccurate and once a mistake is made, the entire experiment has to be repeated. It is therefore recommended to either build a velocity meter on the cart, to have real-time feedback on the velocity, or to alter the power input to a velocity input, to ensure more exact cart velocities during the experiments.

Algae Growth

To combat algae growth in both the mixing tank and the flume, it is recommended to use a bleach solution in the water. Assuming that the flume has a volume of 20 m^3, one liter with a 12.5% solution should be enough to prevent any algae growth. For the mixing tank this would come down to 2 centiliter with a 12.5% solution should be enough. When drawing samples from the mixing tank or flume, which are not analyzed within a short period, it is recommended to add an extra droplet of bleach to make sure that there will be no algae growth.

Altering Velocity Ratio

When working with the velocity ratio ζ or something similar, it is recommended to alter the source velocity instead of the discharge velocity to obtain different velocity ratios in similar experimental runs. Keeping the discharge velocity equal ensures a constant sediment flux, which is more beneficial for finding trends in concentration influences.

In addition to that, in reality, it is simpler to alter the velocity of the PNMT, than to alter the discharge velocity.

6.2.3. Application for Full-Scale Deep-Sea Mining

Based on the conclusions of this research, tentative recommendations for full-scale deep-sea mining can be made. It should be noted that during this research, a lot of assumptions have been made, compromising the resemblance between the experiments and the reality. These recommendations should therefore merely be seen as suggestions. The recommendations are on the source and discharge velocity (Section 6.2.3) and the path planning (Section 6.2.3) of the PNMT during deep-sea mining operations.

Velocity Ratio

It is recommended to adjust the source velocity and discharge velocity in such a way, that they are equal to each other. For different operations, there is probably a different optimal source velocity and therefore the discharge velocity should be adjustable. There are two different ways to adjust the discharge velocity, namely adjusting the discharge area or adding additional discharge pumps.

From the literature, it is found that due to a relatively high discharge velocity (and therefore a low velocity ratio), there is a possibility to generate a floating plume due to the buoyancy domination of the flow. A floating plume has an increased dispersion over a turbidity current. On the other hand, from this research, it is found that a relatively low discharge velocity (and therefore a high velocity ratio) increases the overall dispersion of the turbidity current when driving downhill. In addition to that, a high velocity ratio also gives the propensity to the turbidity current to form a bulge towards the diffuser. This bulge will possibly result in an interaction between the turbidity current and the collector, causing possible blackouts for the sensors and cameras, while also possibly being driven upwards by the rotation of the collector tracks, increasing the dispersion of the turbidity current even more. This bulge has only been observed for the downhill driving experiments. It has been found that for uphill driving experiments, the dispersion for a high velocity ratio does not increase. However, reducing the discharge velocity also means that the area of the diffuser has to be enlarged, reducing the volume efficiency of the PNMT.

All above-mentioned scenarios are undesired and therefore a velocity ratio of 1 is recommended when operating the PNMT.

Path Planning

From this research, it is found that an increase in a slope angle does not increase the sideways dispersion of a turbidity current when driving in the downhill direction. However, it has been found that it does contribute to the formation of a bulge towards the diffuser of the PNMT, which will possibly result in interaction between the turbidity current and the collector, causing possible black-outs for the sensors and cameras, while also possibly be driven upwards by the rotation of the collector tracks, increasing the dispersion of the turbidity current even more. The formation of the bulge is already observed for slope angles as low as 3 degrees during the experiments. This angle is possibly even lower in reality, due to loose sediment on the seabed being suspended due to the current.

In addition to that, it has been found from the literature that loose sediment is very susceptible to a phenomenon called auto-suspension, which is basically the picking up of sediment in the body of the turbidity current from recently settled sediment more upfront in the turbidity current, causing a turbidity current not to reduce in volume and momentum and therefore preventing it from settling fully. This effect is enhanced by a slope, because a turbidity current that propagates downhill gains more momentum than on a flat seabed.

It is therefore recommended to avoid driving downhill on slopes steeper than 3 degrees for a longer period, to avoid turbidity current development behind the PNMT enough to cause excessive bulge formation or auto-suspension. During this research, no trends could be found on the influence of the slope angle on the dispersion of a turbidity current when driving uphill, but logically considered, for steeper slope angles the dispersion will also reduce. At first glance, driving uphill should not cause any extra difficulties.

References

[1] T. Abramowski, M. Urbanek, and P. Baláž. "Structural Economic Assessment of Polymetallic Nodules Mining Project with Updates to Present Market Conditions". en. In: *Minerals* 11.3 (Mar. 2021), p. 311. ISSN: 2075-163X. DOI: 10.3390/min11030311. URL: https://www.mdpi.com/2075-163X/11/3/311.

[2] S. Alhaddad, D. Mehta, and R.L.J. Helmons. "Mining of deep-seabed nodules using a Coandă-effect-based collector". en. In: *Results in Engineering* 17 (Mar. 2023), p. 100852. ISSN: 25901230. DOI: 10.1016/j.rineng.2022.100852. URL: https://linkinghub.elsevier.com/retrieve/pii/S2590123022005229.

[3] M. Allaby. *Flocculation | Encyclopedia.com*. En. May 2018. URL: https://www.encyclopedia.com/earth-and-environment/ecology-and-environmentalism/environmental-studies/flocculation.

[4] D.J. Amon and C.R. Smith. "The Clarion-Clipperton Zone". en. In: (Dec. 2017), p. 3. URL: https://www.pewtrusts.org/-/media/assets/2017/12/sea_the_clarion_clipperton_zone.pdf.

[5] D.J. Amon et al. "Insights into the abundance and diversity of abyssal megafauna in a polymetallic-nodule region in the eastern Clarion-Clipperton Zone". en. In: *Scientific Reports* 6.1 (July 2016), p. 30492. ISSN: 2045-2322. DOI: 10.1038/srep30492. URL: https://www.nature.com/articles/srep30492.

[6] R.A. Bagnold. "Auto-suspension of transported sediment; turbidity currents". en. In: *Proceedings of the Royal Society of London. Series A. Mathematical and Physical Sciences* 265.1322 (Jan. 1962), pp. 315–319. ISSN: 0080-4630, 2053-9169. DOI: 10.1098/rspa.1962.0012. URL: https://royalsocietypublishing.org/doi/10.1098/rspa.1962.0012.

[7] T.E. Baldock et al. "Settling velocity of sediments at high concentrations". In: *Coastal Engineering* 51.1 (Mar. 2004), pp. 91–100. ISSN: 0378-3839. DOI: 10.1016/j.coastaleng.2003.12.004. URL: https://www.sciencedirect.com/science/article/pii/S0378383903001340.

[8] C. Blanchard et al. "The current status of deep-sea mining governance at the International Seabed Authority". In: *Marine Policy* 147 (Jan. 2023), p. 105396. ISSN: 0308-597X. DOI: 10.1016/j.marpol.2022.105396. URL: https://www.sciencedirect.com/science/article/pii/S0308597X22004432.

[9] F. Blanchette. "Shallow-water equations and box model simulations of turbidity currents from a moving source". en. In: *Physical Review Fluids* 7.8 (Aug. 2022), p. 084301. ISSN: 2469-990X. DOI: 10.1103/PhysRevFluids.7.084301. URL: https://link.aps.org/doi/10.1103/PhysRevFluids.7.084301.

[10] B K Blankenaar. *The deep sea mining horizontal discharge plume*. en. Tech. rep. June 2020. URL: https://repository.tudelft.nl/islandora/object/uuid%3Af59153b3-8ab6-4b6c-8d17-fd2ad6d29f5a.

[11] G. Carazzo, E. Kaminski, and S. Tait. "The route to self-similarity in turbulent jets and plumes". en. In: *Journal of Fluid Mechanics* 547 (Jan. 2006). Publisher: Cambridge University Press, pp. 137–148. ISSN: 1469-7645, 0022-1120. DOI: 10.1017/S002211200500683X. URL: https://www.cambridge.org/core/journals/journal-of-fluid-mechanics/article/abs/route-to-selfsimilarity-in-turbulent-jets-and-plumes/D4C2248189B7F490AC3E99F44759631E.

[12] P. Carlotti and G.R. Hunt. "Analytical solutions for turbulent non-Boussinesq plumes". en. In: *Journal of Fluid Mechanics* 538 (Sept. 2005). Publisher: Cambridge University Press, pp. 343–359. ISSN: 1469-7645, 0022-1120. DOI: 10.1017/S0022112005005379. URL: https://www.cambridge.org/core/journals/journal-of-fluid-mechanics/article/abs/analytical-solutions-for-turbulent-nonboussinesq-plumes/E272D7256C238EB02B9870B6D16F2711.

[13] C. Carrera et al. “Clean Energy Transition, Scarcity and Urban Mining”. en. In: *SSRN Electronic Journal* (2023). ISSN: 1556-5068. DOI: `10.2139/ssrn.4424516`. URL: `https://www.ssrn.com/abstract=4424516`.

[14] *ChatGPT*. 2024. URL: `https://chatgpt.com/`.

[15] Oliver Chmiel, Ivo Baselt, and Andreas Malcherek. “Applicability of Acoustic Concentration Measurements in Suspensions of Artificial and Natural Sediments Using an Acoustic Doppler Velocimeter”. en. In: *Acoustics* 1.1 (Dec. 2018), pp. 59–77. ISSN: 2624-599X. DOI: `10.3390/acoustics1010006`. URL: `https://www.mdpi.com/2624-599X/1/1/6`.

[16] M.R. Chowdhury and F.Y. Testik. “A review of gravity currents formed by submerged single-port discharges in inland and coastal waters”. en. In: *Environmental Fluid Mechanics* 14.2 (Apr. 2014), pp. 265–293. ISSN: 1573-1510. DOI: `10.1007/s10652-014-9334-7`. URL: `https://doi.org/10.1007/s10652-014-9334-7`.

[17] Christophe. *Dichtheid van water en temperatuur*. URL: `https://nl.econologie.com/massa-volume-temperatuur-water/`.

[18] A. Dai. “Experiments on gravity currents propagating on different bottom slopes”. en. In: *Journal of Fluid Mechanics* 731 (Sept. 2013), pp. 117–141. ISSN: 0022-1120, 1469-7645. DOI: `10.1017/jfm.2013.372`. URL: `https://www.cambridge.org/core/product/identifier/S0022112013003728/type/journal_article`.

[19] A. Dai and Y. Huang. “Boussinesq and non-Boussinesq gravity currents propagating on unbounded uniform slopes in the deceleration phase”. en. In: *Journal of Fluid Mechanics* 917 (June 2021), A23. ISSN: 0022-1120, 1469-7645. DOI: `10.1017/jfm.2021.300`. URL: `https://www.cambridge.org/core/product/identifier/S0022112021003001/type/journal_article`.

[20] B. Decrop and T.D. Wachter. “Detailed CFD Simulations For near Field Dispersion of Deep Sea Mining Plumes”. In: *Proceedings of the World dredging conference Wodcon xxll, Shanghai, China*. 2019, pp. 22–26.

[21] J.C. Drazen et al. “Regional Variation in Communities of Demersal Fishes and Scavengers Across the CCZ and Pacific Ocean”. In: *Frontiers in Marine Science* 8 (2021). ISSN: 2296-7745. URL: `https://www.frontiersin.org/articles/10.3389/fmars.2021.630616`.

[22] M. Elerian, C. Van Rhee, and R.L.J. Helmons. “Experimental and Numerical Modelling of Deep-Sea-Mining-Generated Turbidity Currents”. en. In: *Minerals* 12.5 (Apr. 2022), p. 558. ISSN: 2075-163X. DOI: `10.3390/min12050558`. URL: `https://www.mdpi.com/2075-163X/12/5/558`.

[23] M. Elerian et al. “Flocculation effect on turbidity flows generated by deep-sea mining: A numerical study”. en. In: *Ocean Engineering* 277 (June 2023), p. 114250. ISSN: 00298018. DOI: `10.1016/j.oceaneng.2023.114250`. URL: `https://linkinghub.elsevier.com/retrieve/pii/S0029801823006340`.

[24] M. Elerian et al. “Near-Field Analysis of Turbidity Flows Generated by Polymetallic Nodule Mining Tools”. en. In: *Mining* 1.3 (Nov. 2021), pp. 251–278. ISSN: 2673-6489. DOI: `10.3390/mining1030017`. URL: `https://www.mdpi.com/2673-6489/1/3/17`.

[25] H.J.S. Fernando, ed. *Handbook of environmental fluid dynamics. Volume 1, Overview and fundamentals*. eng. OCLC: 1125075408. Boca Raton: CRC Press, 2019. ISBN: 978-0-367-44587-4.

[26] H.B. Fischer et al. *Mixing in Inland and Coastal Waters - 1st Edition*. Nov. 1979. URL: `https://shop.elsevier.com/books/mixing-in-inland-and-coastal-waters/fischer/978-0-08-051177-1`.

[27] T. Gerber et al. “Autocyclic Behavior of Experimental Turbidity Currents”. In: *AGU Fall Meeting Abstracts* (Jan. 2004).

[28] B. Gillard et al. “Physical and hydrodynamic properties of deep sea mining-generated, abyssal sediment plumes in the Clarion Clipperton Fracture Zone (eastern-central Pacific)”. en. In: *Elementa: Science of the Anthropocene* 7 (Jan. 2019). Ed. by J.W. Deming and S.F. Ackley, p. 5. ISSN: 2325-1026. DOI: `10.1525/elementa.343`. URL: `https://online.ucpress.edu/elementa/article/doi/10.1525/elementa.343/112485/Physical-and-hydrodynamic-properties-of-deep-sea`.

[29] *Grammarly*. 2024. URL: `https://app.grammarly.com/`.

[30] Frans van Grunsven, Cees van Rhee, and Geert Keetels. "The initial spreading of turbidity plumes - Dedicated laboratory experiments for model validation". In: (Sept. 2018). URL: https://www.researchgate.net/publication/328364913_The_initial_spreading_of_turbidity_plumes_-_Dedicated_laboratory_experiments_for_model_validation.

[31] M. Hallworth et al. "Entrainment into two-dimensional and axisymmetric turbulent gravity currents". In: *Journal of Fluid Mechanics* 308 (Feb. 1996), pp. 289–311. DOI: 10.1017/S0022112096001486.

[32] Z. He et al. "Investigations of dynamic behaviors of lock-exchange turbidity currents down a slope based on direct numerical simulation". en. In: *Advances in Water Resources* 119 (Sept. 2018), pp. 164–177. ISSN: 03091708. DOI: 10.1016/j.advwatres.2018.07.008. URL: https://linkinghub.elsevier.com/retrieve/pii/S0309170817308874.

[33] R.L.J. Helmons et al. "Dispersion of Benthic Plumes in Deep-Sea Mining: What Lessons Can Be Learned From Dredging?" In: *Frontiers in Earth Science* 10 (May 2022), p. 868701. ISSN: 2296-6463. DOI: 10.3389/feart.2022.868701. URL: https://www.frontiersin.org/articles/10.3389/feart.2022.868701/full.

[34] IISD's SDG Knowledge Hub. *ISA Assembly Elects Council Members, Discusses Two-year Timeline Trigger | News | SDG Knowledge Hub | IISD*. en-US. Aug. 2022. URL: http://sdg.iisd.org/news/isa-assembly-elects-council-members-discusses-two-year-timeline-trigger/.

[35] G. Hunt and T. van den Bremer. "Classical plume theory: 1937-2010 and beyond". In: *IMA Journal of Applied Mathematics* 76 (June 2011). DOI: 10.1093/imamat/hxq056.

[36] H.E. Huppert and J.E. Simpson. "The slumping of gravity currents". en. In: *Journal of Fluid Mechanics* 99.4 (Aug. 1980). Publisher: Cambridge University Press, pp. 785–799. ISSN: 1469-7645, 0022-1120. DOI: 10.1017/S0022112080000894. URL: https://www.cambridge.org/core/journals/journal-of-fluid-mechanics/article/abs/slumping-of-gravity-currents/27A0E9D6FFE0C745FE4E4C37AE2DC222.

[37] IEA. "World Energy Outlook 2021". en. In: (Dec. 2021). URL: https://www.iea.org/reports/world-energy-outlook-2021.

[38] IEA. "World Energy Outlook 2022". en. In: (Nov. 2022). URL: https://www.iea.org/reports/world-energy-outlook-2022.

[39] ISA. *Clarion Clipperton Fracture Zone*. URL: https://www.isa.org.jm/maps/clarion-clipperton-fracture-zone/.

[40] ISA. *Clarion Clipperton Zone - International Seabed Authority*. en-US. July 2022. URL: https://www.isa.org.jm/maps/clarion-clipperton-zone/.

[41] ISA. *Polymetallic nodules - Nature of the minerals*. en. June 2022. URL: https://www.isa.org.jm/wp-content/uploads/2022/06/eng7.pdf.

[42] Y. Kang and S. Liu. "The Development History and Latest Progress of Deep-Sea Polymetallic Nodule Mining Technology". en. In: *Minerals* 11.10 (Oct. 2021), p. 1132. ISSN: 2075-163X. DOI: 10.3390/min11101132. URL: https://www.mdpi.com/2075-163X/11/10/1132.

[43] S. Krishna et al. "Ultrasound velocity profiling technique for in-line rheological measurements: A prospective review". en. In: *Measurement* 205 (Dec. 2022), p. 112152. ISSN: 02632241. DOI: 10.1016/j.measurement.2022.112152. URL: https://linkinghub.elsevier.com/retrieve/pii/S0263224122013483.

[44] W.Y. Lee, A.C.Y. Li, and Joseph H.W. Lee. "Structure of a Horizontal Sediment-Laden Momentum Jet". en. In: *Journal of Hydraulic Engineering* 139.2 (Feb. 2013), pp. 124–140. ISSN: 0733-9429, 1943-7900. DOI: 10.1061/(ASCE)HY.1943-7900.0000662. URL: https://ascelibrary.org/doi/10.1061/%28ASCE%29HY.1943-7900.0000662.

[45] A.B. Leitner et al. "Environmental and bathymetric influences on abyssal bait-attending communities of the Clarion Clipperton Zone". en. In: *Deep Sea Research Part I: Oceanographic Research Papers* 125 (July 2017), pp. 65–80. ISSN: 09670637. DOI: 10.1016/j.dsr.2017.04.017. URL: https://linkinghub.elsevier.com/retrieve/pii/S0967063716303636.

[46] Y. Lin et al. “Simulation Study on the Sediment Dispersion during Deep-Sea Nodule Harvesting”. en. In: *Journal of Marine Science and Engineering* 11.1 (Jan. 2023). Number: 1 Publisher: Multidisciplinary Digital Publishing Institute, p. 10. ISSN: 2077-1312. DOI: 10.3390/jmse11010010. URL: https://www.mdpi.com/2077-1312/11/1/10.

[47] S. Liu et al. “A Numerical Investigation of the Dynamic Interaction between the Deep-Sea Mining Vehicle and Sediment Plumes Based on a Small-Scale Analysis”. en. In: *Journal of Marine Science and Engineering* 11.7 (July 2023). Number: 7 Publisher: Multidisciplinary Digital Publishing Institute, p. 1458. ISSN: 2077-1312. DOI: 10.3390/jmse11071458. URL: https://www.mdpi.com/2077-1312/11/7/1458.

[48] G. Marjanovic, G. Taub, and S. Balachandar. “On the effects of buoyancy on higher order moments in lazy plumes”. In: *Journal of Turbulence* 20.2 (Feb. 2019). Publisher: Taylor & Francis _eprint: https://doi.org/10.1080/14685248.2019.1593993, pp. 121–146. ISSN: null. DOI: 10.1080/14685248.2019.1593993. URL: https://doi.org/10.1080/14685248.2019.1593993.

[49] E. Meiburg, S. Radhakrishnan, and M. Nasr-Azadani. “Modeling Gravity and Turbidity Currents: Computational Approaches and Challenges”. en. In: *Applied Mechanics Reviews* 67.4 (July 2015), p. 040802. ISSN: 0003-6900, 2379-0407. DOI: 10.1115/1.4031040. URL: https://asmedigitalcollection.asme.org/appliedmechanicsreviews/article/doi/10.1115/1.4031040/370037/Modeling-Gravity-and-Turbidity-Currents.

[50] G.V. Middleton. “Sediment Deposition from Turbidity Currents”. In: *Annual Review of Earth and Planetary Sciences* 21.1 (1993). _eprint: https://doi.org/10.1146/annurev.ea.21.050193.000513, pp. 89–114. DOI: 10.1146/annurev.ea.21.050193.000513. URL: https://doi.org/10.1146/annurev.ea.21.050193.000513.

[51] S.A. Miedema. *Dredging Engineering: Special Topics*. en. Text.Chapter. June 2019. URL: https://textbooks.open.tudelft.nl/textbooks/catalog/view/22/47/144-1.

[52] K.A. Miller et al. “An Overview of Seabed Mining Including the Current State of Development, Environmental Impacts, and Knowledge Gaps”. en. In: *Frontiers in Marine Science* 4 (Jan. 2018), p. 418. ISSN: 2296-7745. DOI: 10.3389/fmars.2017.00418. URL: http://journal.frontiersin.org/article/10.3389/fmars.2017.00418/full.

[53] B.R. Morton. “Forced plumes”. en. In: *Journal of Fluid Mechanics* 5.1 (Jan. 1959). Publisher: Cambridge University Press, pp. 151–163. ISSN: 1469-7645, 0022-1120. DOI: 10.1017/S002211205900012X. URL: https://www.cambridge.org/core/journals/journal-of-fluid-mechanics/article/abs/forced-plumes/7B370C2AABC31FABB5F6C69354CEB7D1.

[54] B.R. Morton and J. Middleton. “Scale diagrams for forced plumes”. en. In: *Journal of Fluid Mechanics* 58.1 (Mar. 1973). Publisher: Cambridge University Press, pp. 165–176. ISSN: 1469-7645, 0022-1120. DOI: 10.1017/S002211207300220X. URL: https://www.cambridge.org/core/journals/journal-of-fluid-mechanics/article/abs/scale-diagrams-for-forced-plumes/C19BB94A106FDAE4BFD4FED6A7D726C5.

[55] C. Muñoz-Royo et al. “An in situ study of abyssal turbidity-current sediment plumes generated by a deep seabed polymetallic nodule mining preprototype collector vehicle”. en. In: *Science Advances* 8.38 (Sept. 2022), eabn1219. ISSN: 2375-2548. DOI: 10.1126/sciadv.abn1219. URL: https://www.science.org/doi/10.1126/sciadv.abn1219.

[56] S.P. Neill and M.R. Hashemi. “In Situ and Remote Methods for Resource Characterization”. en. In: *Fundamentals of Ocean Renewable Energy*. Elsevier, 2018, pp. 157–191. ISBN: 978-0-12-810448-4. DOI: 10.1016/B978-0-12-810448-4.00007-0. URL: https://linkinghub.elsevier.com/retrieve/pii/B9780128104484000070.

[57] J.A. Osejo Rodriguez. *Small scale testing of crawler outlet diffusers for plume reduction of offshore mining*. Tech. rep. Oct. 2018.

[58] R. Ouillon, E. Meiburg, and B.R. Sutherland. “Turbidity currents propagating down a slope into a stratified saline ambient fluid”. en. In: *Environmental Fluid Mechanics* 19.5 (Oct. 2019), pp. 1143–1166. ISSN: 1567-7419, 1573-1510. DOI: 10.1007/s10652-019-09675-z. URL: http://link.springer.com/10.1007/s10652-019-09675-z.

[59] R. Ouillon et al. "Gravity currents from moving sources". en. In: *Journal of Fluid Mechanics* 924 (Oct. 2021), A43. ISSN: 0022-1120, 1469-7645. DOI: 10.1017/jfm.2021.654. URL: https://www.cambridge.org/core/product/identifier/S0022112021006546/type/journal_article.

[60] J. Parianos, I. Lipton, and M. Nimmo. "Aspects of Estimation and Reporting of Mineral Resources of Seabed Polymetallic Nodules: A Contemporaneous Case Study". en. In: *Minerals* 11.2 (Feb. 2021), p. 200. ISSN: 2075-163X. DOI: 10.3390/min11020200. URL: https://www.mdpi.com/2075-163X/11/2/200.

[61] J. Parianos, A. O'Sullivan, and P. Madureira. "Geology of parts of the central and eastern Clarion Clipperton Zone". en. In: *Journal of Maps* 18.2 (Dec. 2022), pp. 232–245. ISSN: 1744-5647. DOI: 10.1080/17445647.2022.2035267. URL: https://www.tandfonline.com/doi/full/10.1080/17445647.2022.2035267.

[62] G. Parker, Y. Fukushima, and H.M. Pantin. "Self-accelerating turbidity currents". en. In: *Journal of Fluid Mechanics* 171.-1 (Oct. 1986), p. 145. ISSN: 0022-1120, 1469-7645. DOI: 10.1017/S0022112086001404. URL: http://www.journals.cambridge.org/abstract_S0022112086001404.

[63] K. van Pelt. *Sediment dispersion from a moving source*. en. Tech. rep. TU Delft, Aug. 2023. URL: https://repository.tudelft.nl/islandora/object/uuid%3Aab3e1d3e-11db-4d57-8da0-0e63020ae67c?collection=education.

[64] T. Prešeren et al. "The theoretical densimetric Froude number values with favourable effect on the clarifier performance". en. In: *Chemical Engineering and Processing: Process Intensification* 74 (Dec. 2013), pp. 97–105. ISSN: 02552701. DOI: 10.1016/j.cep.2013.09.001. URL: https://linkinghub.elsevier.com/retrieve/pii/S0255270113001943.

[65] W.J. Rankin. *Manganese Nodule - an overview | ScienceDirect Topics*. 2014. URL: https://www.sciencedirect.com/topics/engineering/manganese-nodule.

[66] J.F. Richardson and W.N. Zaki. "Sedimentation and fluidisation: Part I". en. In: *Chemical Engineering Research and Design* 75 (1954), S82–S100. ISSN: 02638762. DOI: 10.1016/S0263-8762(97)80006-8. URL: https://linkinghub.elsevier.com/retrieve/pii/S0263876297800068.

[67] J.W. Rottman and J.E. Simpson. "Gravity currents produced by instantaneous releases of a heavy fluid in a rectangular channel". en. In: *Journal of Fluid Mechanics* 135 (Oct. 1983). Publisher: Cambridge University Press, pp. 95–110. ISSN: 1469-7645, 0022-1120. DOI: 10.1017/S0022112083002979. URL: https://www.cambridge.org/core/journals/journal-of-fluid-mechanics/article/abs/gravity-currents-produced-by-instantaneous-releases-of-a-heavy-fluid-in-a-rectangular-channel/D2874537091096C7C710F2880077746F.

[68] Jon R. Rotzien et al. "Chapter 6 - Deepwater sedimentary processes". In: *Deepwater Sedimentary Systems*. Ed. by Jon R. Rotzien et al. Elsevier, Jan. 2022, pp. 179–202. ISBN: 978-0-323-91918-0. DOI: 10.1016/B978-0-323-91918-0.00021-9. URL: https://www.sciencedirect.com/science/article/pii/B9780323919180000219.

[69] O.E. Sequeiros et al. "Experimental study on self-accelerating turbidity currents". en. In: *Journal of Geophysical Research: Oceans* 114.C5 (May 2009), 2008JC005149. ISSN: 0148-0227. DOI: 10.1029/2008JC005149. URL: https://agupubs.onlinelibrary.wiley.com/doi/10.1029/2008JC005149.

[70] A. Shakeel et al. "Flocculation of Clay Suspensions by Anionic and Cationic Polyelectrolytes: A Systematic Analysis". en. In: *Minerals* 10.11 (Nov. 2020), p. 999. ISSN: 2075-163X. DOI: 10.3390/min10110999. URL: https://www.mdpi.com/2075-163X/10/11/999.

[71] G. Shanmugam. "Gravity flows: Types, definitions, origins, identification markers, and problems: Gravity lows". en. In: *Journal of The Indian Association of Sedimentologists* 37.2 (Dec. 2020), pp. 61–90. ISSN: 2582-2020, 0970-3268. DOI: 10.51710/jias.v37i2.117. URL: http://journal.indiansedimentologists.com/ojs/index.php/1/article/view/117.

[72] R. Sharma, ed. *Deep-Sea Mining: Resource Potential, Technical and Environmental Considerations*. en. Cham: Springer International Publishing, 2017. ISBN: 978-3-319-52556-3. DOI: 10.1007/978-3-319-52557-0. URL: http://link.springer.com/10.1007/978-3-319-52557-0.

[73] E. Simon-Lledó et al. "Megafaunal variation in the abyssal landscape of the Clarion Clipperton Zone". en. In: *Progress in Oceanography* 170 (Jan. 2019), pp. 119–133. ISSN: 00796611. DOI: 10.1016/j.pocean.2018.11.003. URL: https://linkinghub.elsevier.com/retrieve/pii/S0079661118301824.

[74] E. Simon-Lledó et al. “Ecology of a polymetallic nodule occurrence gradient: Implications for deep-sea mining”. en. In: *Limnology and Oceanography* 64.5 (Sept. 2019), pp. 1883–1894. ISSN: 0024-3590, 1939-5590. DOI: 10.1002/lno.11157. URL: https://aslopubs.onlinelibrary.wiley.com/doi/10.1002/lno.11157.

[75] SimScale. *What is the Boussinesq Approximation? (CFD)*. en-US. Oct. 2023. URL: https://www.simscale.com/docs/simwiki/cfd-computational-fluid-dynamics/what-is-boussinesq-approximation/.

[76] S. Steen. *General Modelling and Scaling Laws*. en. Feb. 2017. URL: https://home.hvl.no/ansatte/gste/ftp/MarinLab_files/Litteratur/NTNU_Scaling_Laws.pdf.

[77] K. Steenhauer, T. Tokyay, and G. Constantinescu. “Dynamics and structure of planar gravity currents propagating down an inclined surface”. en. In: *Physics of Fluids* 29.3 (Mar. 2017), p. 036604. ISSN: 1070-6631, 1089-7666. DOI: 10.1063/1.4979063. URL: https://pubs.aip.org/pof/article/29/3/036604/316325/Dynamics-and-structure-of-planar-gravity-currents.

[78] A.A.B. Vásquez. *Quantifying the dispersion of turbidity currents generated by seafloor mining operations*. en. Tech. rep. Aug. 2020. URL: http://resolver.tudelft.nl/uuid:61d6fefb-d99f-4f9d-aa82-db5b4a6b483d.

[79] M.G. Wells and R.M. Dorrell. “Turbulence Processes Within Turbidity Currents”. In: *Annual Review of Fluid Mechanics* 53.1 (2021). _eprint: https://doi.org/10.1146/annurev-fluid-010719-060309, pp. 59–83. DOI: 10.1146/annurev-fluid-010719-060309. URL: https://doi.org/10.1146/annurev-fluid-010719-060309.

[80] F.M. White. *Fluid mechanics*. en. Eighth edition. New York, NY: McGraw-Hill Education, 2016. ISBN: 978-0-07-339827-3.

[81] Y. Wijmans. *Horizontal negatively buoyant jets in deep sea mining*. en. Tech. rep. Nov. 2021. URL: https://repository.tudelft.nl/islandora/object/uuid%3A0791b3de-1033-4e5f-be64-235b280e30d7.

[82] J. Xie et al. “Turbidity currents propagating down an inclined slope: particle auto-suspension”. en. In: *Journal of Fluid Mechanics* 954 (Jan. 2023), A44. ISSN: 0022-1120, 1469-7645. DOI: 10.1017/jfm.2022.1041. URL: https://www.cambridge.org/core/product/identifier/S0022112022010412/type/journal_article.

A | Calibration Curves

A.1. Cart Velocity Calibration

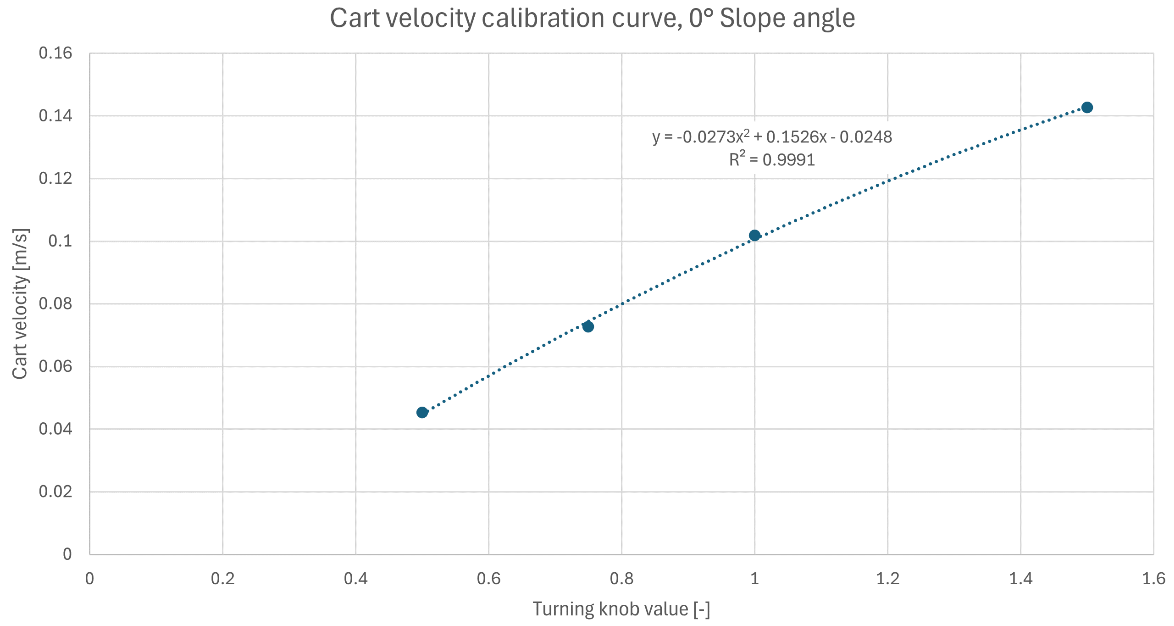

Figure A.1: Cart velocity calibration curve, 0° Slope angle

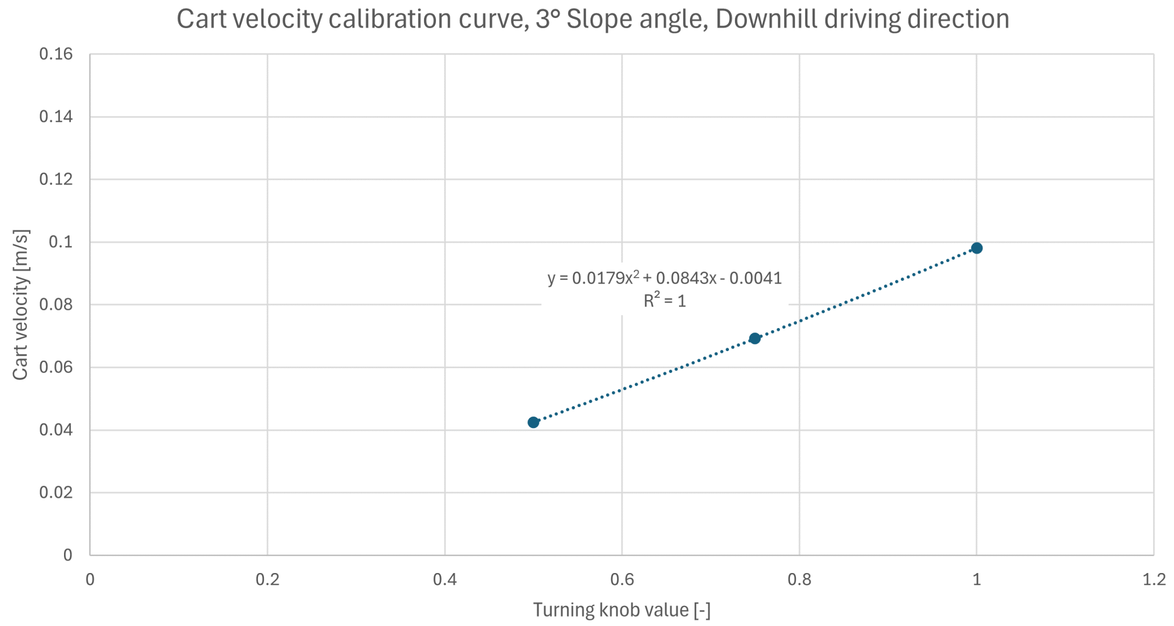

Figure A.2: Cart velocity calibration curve, 3° Slope angle, Downhill driving direction

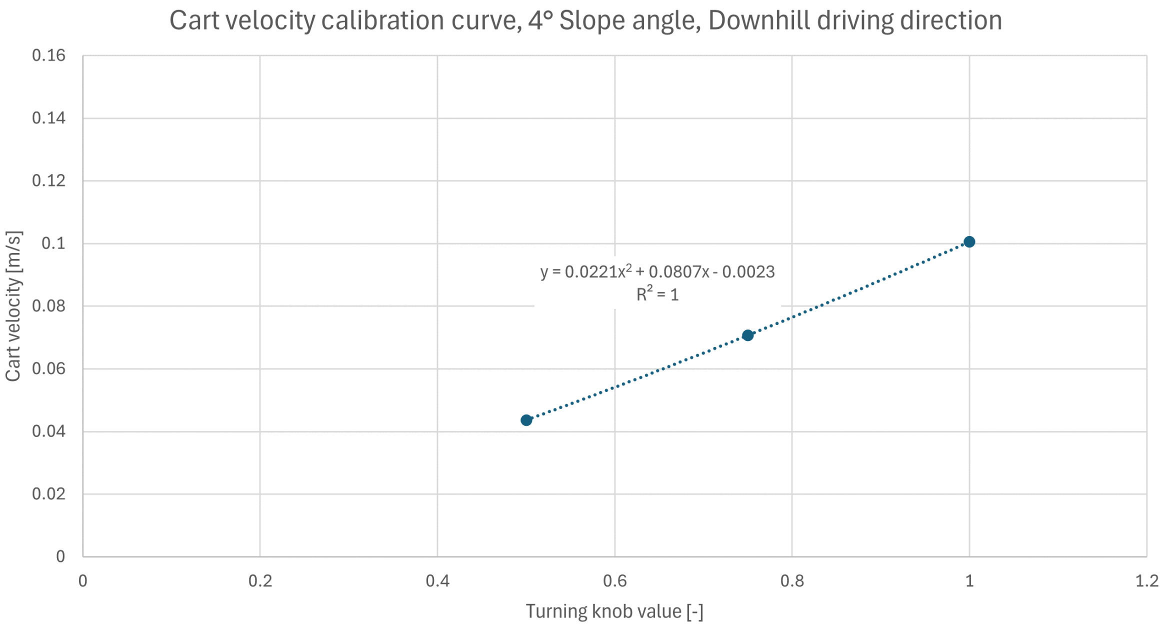

Figure A.3: Cart velocity calibration curve, 4° Slope angle, Downhill driving direction

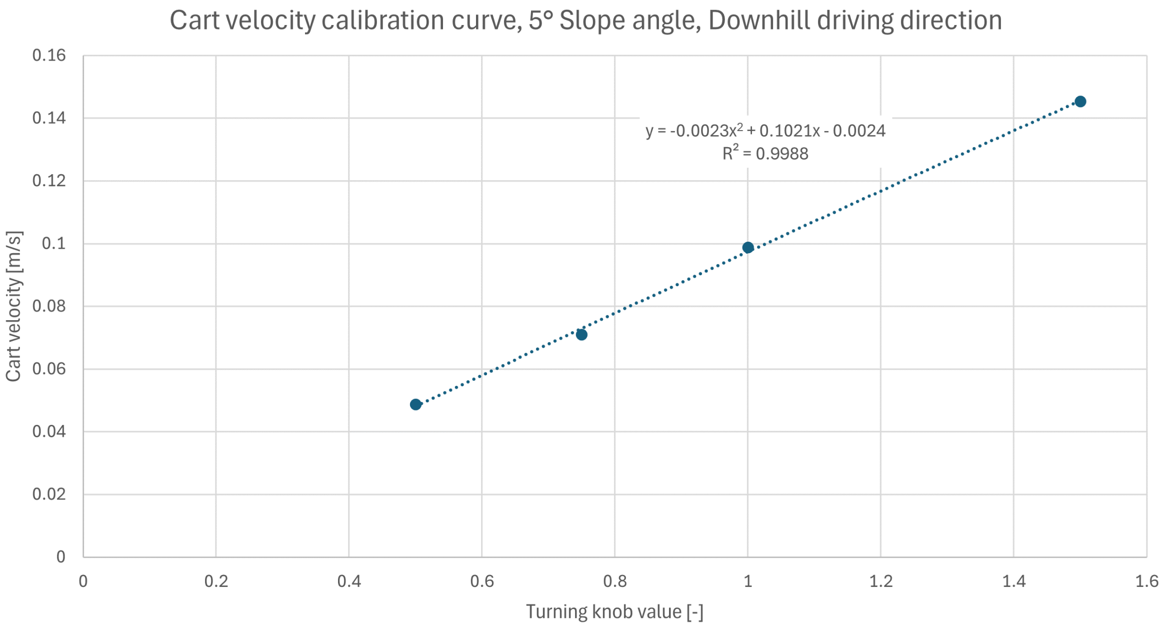

Figure A.4: Cart velocity calibration curve, 5° Slope angle, Downhill driving direction

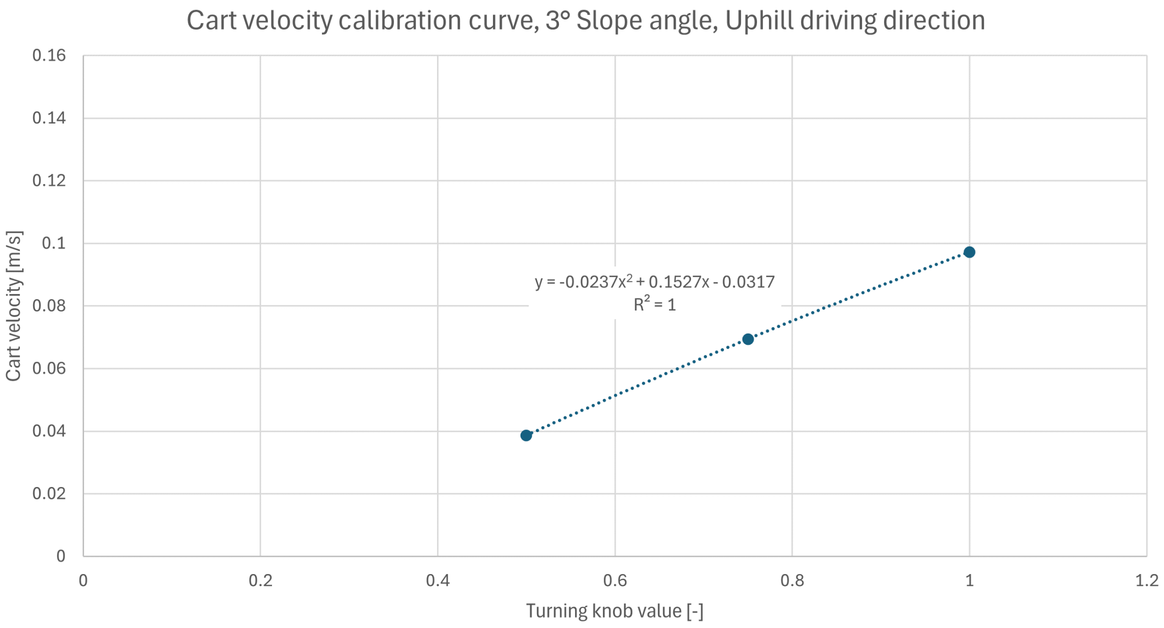

Figure A.5: Cart velocity calibration curve, 3° Slope angle, Uphill driving direction

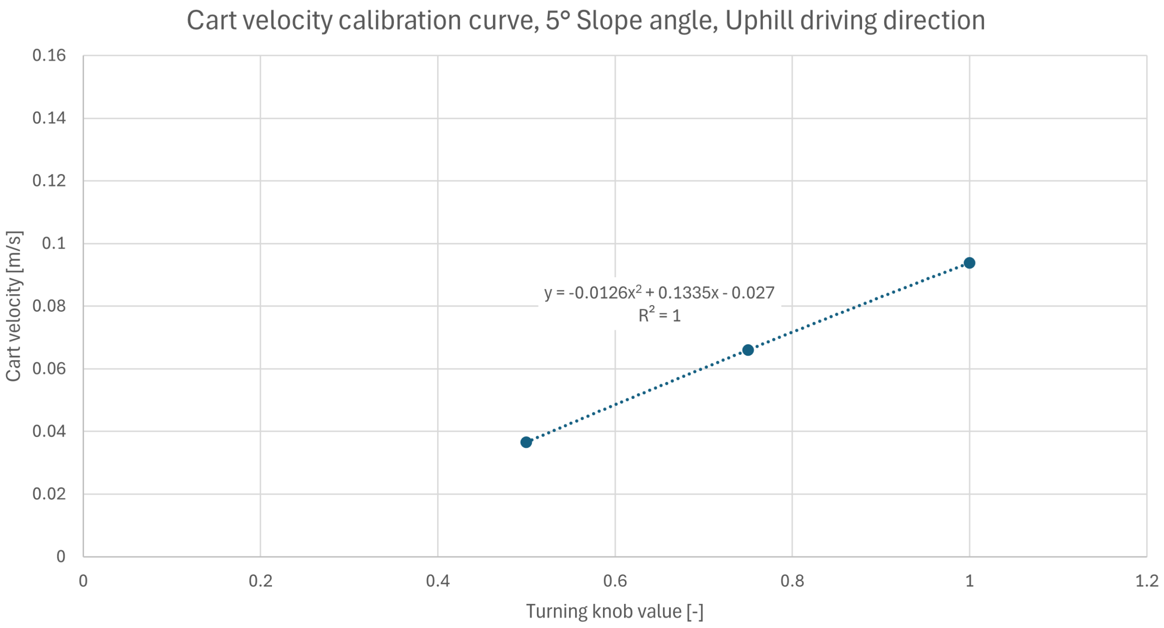

Figure A.6: Cart velocity calibration curve, 5° Slope angle, Uphill driving direction

A.2. ADV Calibration

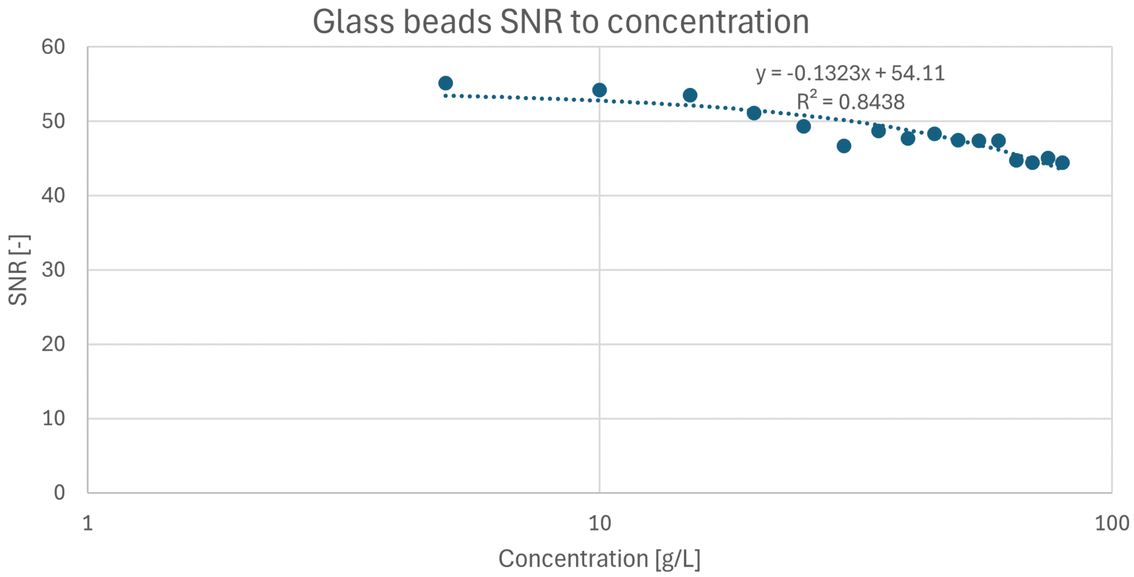

Figure A.7: ADV calibration curve

B | Camera Footage

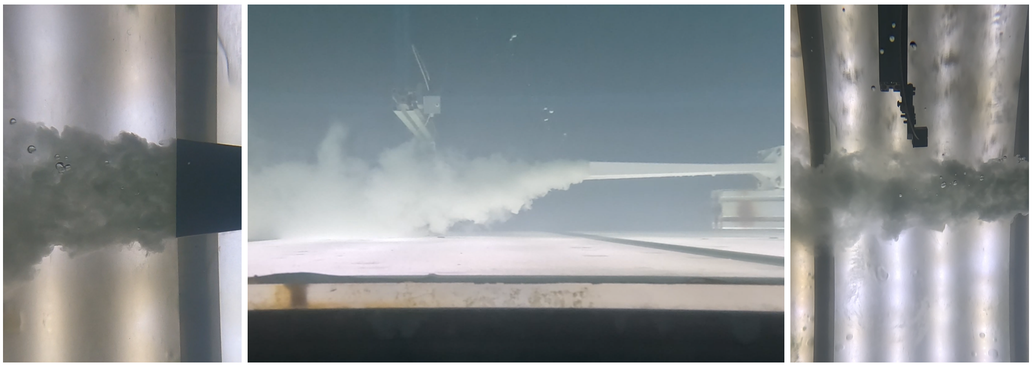
(a) Mounted view **(b)** Side view **(c)** Top view

Figure B.1: Experiment 1 - Snapshots from camera footage


(a) Mounted view **(b)** Side view **(c)** Top view

Figure B.2: Experiment 2 - Snapshots from camera footage

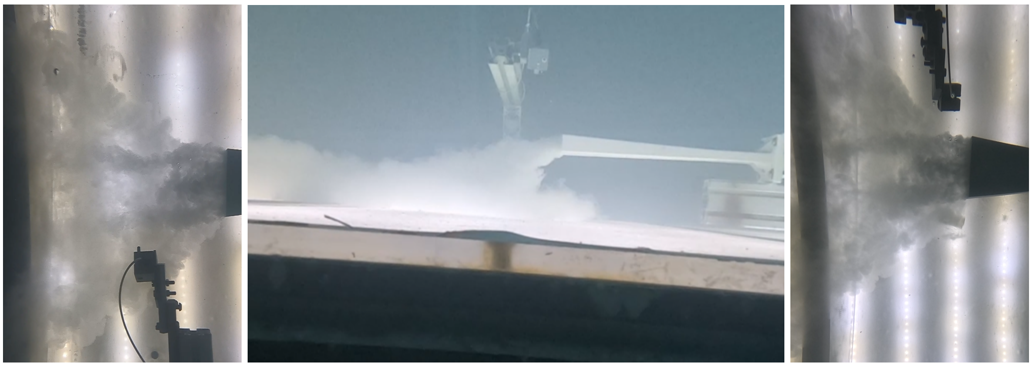
(a) Mounted view **(b)** Side view **(c)** Top view

Figure B.3: Experiment 7 - Snapshots from camera footage

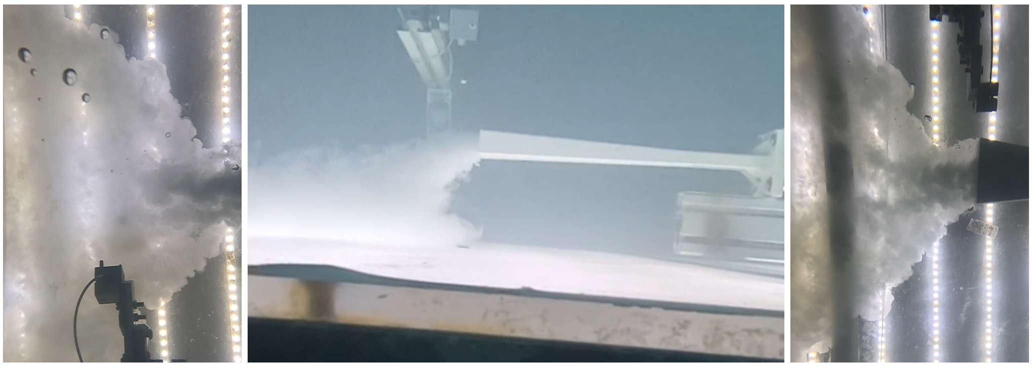

(a) Mounted view **(b)** Side view **(c)** Top view

Figure B.4: Experiment 8 - Snapshots from camera footage

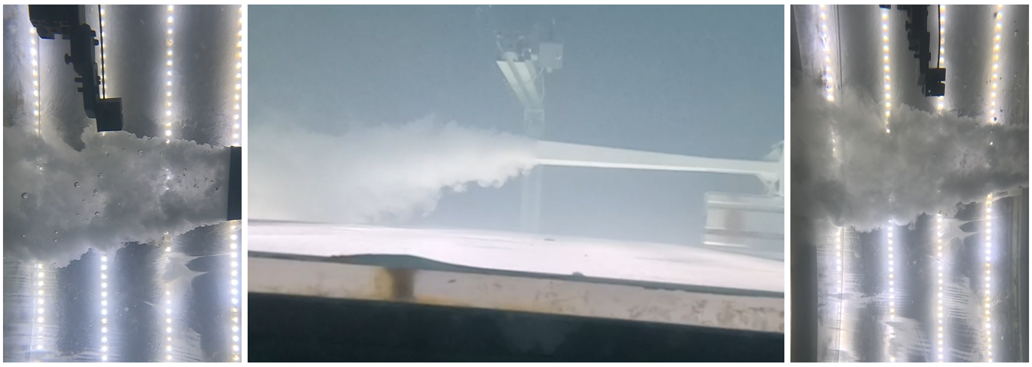

(a) Mounted view **(b)** Side view **(c)** Top view

Figure B.5: Experiment 8.1 - Snapshots from camera footage

(a) Mounted view **(b)** Side view **(c)** Top view

Figure B.6: Experiment 8.2 - Snapshots from camera footage

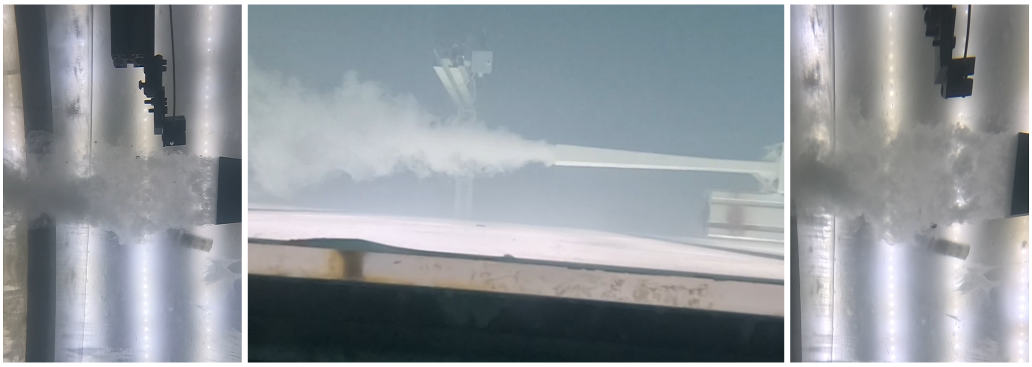

(a) Mounted view **(b)** Side view **(c)** Top view

Figure B.7: Experiment 8.3.1 - Snapshots from camera footage

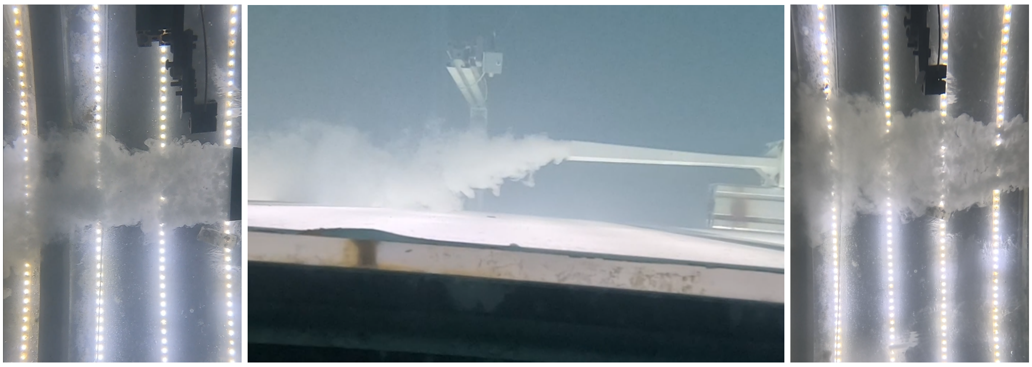

(a) Mounted view **(b)** Side view **(c)** Top view

Figure B.8: Experiment 8.3.2 - Snapshots from camera footage

(a) Mounted view **(b)** Side view **(c)** Top view

Figure B.9: Experiment 9 - Snapshots from camera footage

(a) Mounted view **(b)** Side view **(c)** Top view

Figure B.10: Experiment 10 - Snapshots from camera footage

(a) Mounted view **(b)** Side view **(c)** Top view

Figure B.11: Experiment 15 - Snapshots from camera footage

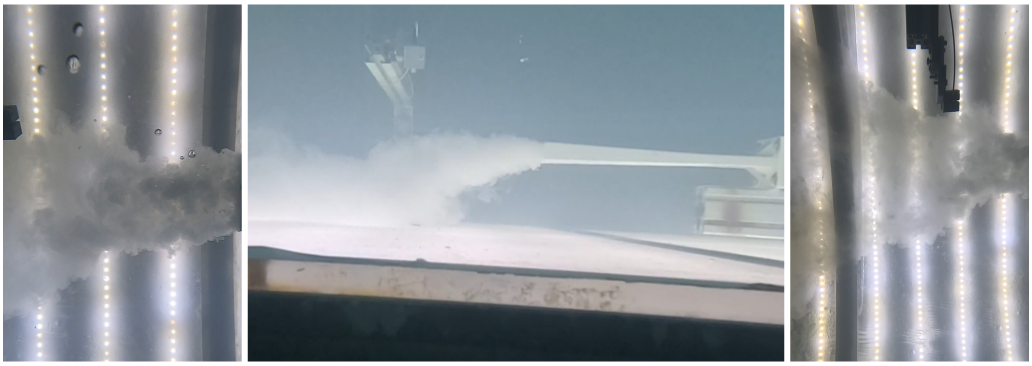

(a) Mounted view **(b)** Side view **(c)** Top view

Figure B.12: Experiment 16 - Snapshots from camera footage

(a) Mounted view **(b)** Side view **(c)** Top view

Figure B.13: Experiment 21 - Snapshots from camera footage

(a) Mounted view **(b)** Side view **(c)** Top view

Figure B.14: Experiment 22 - Snapshots from camera footage

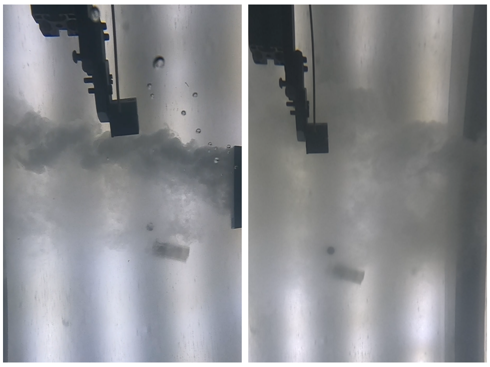

(a) Mounted view **(b)** Top view

Figure B.15: Experiment 23 - Snapshots from camera footage

(a) Mounted view **(b)** Side view **(c)** Top view

Figure B.16: Experiment 24 - Snapshots from camera footage

C | Velocity Profiles

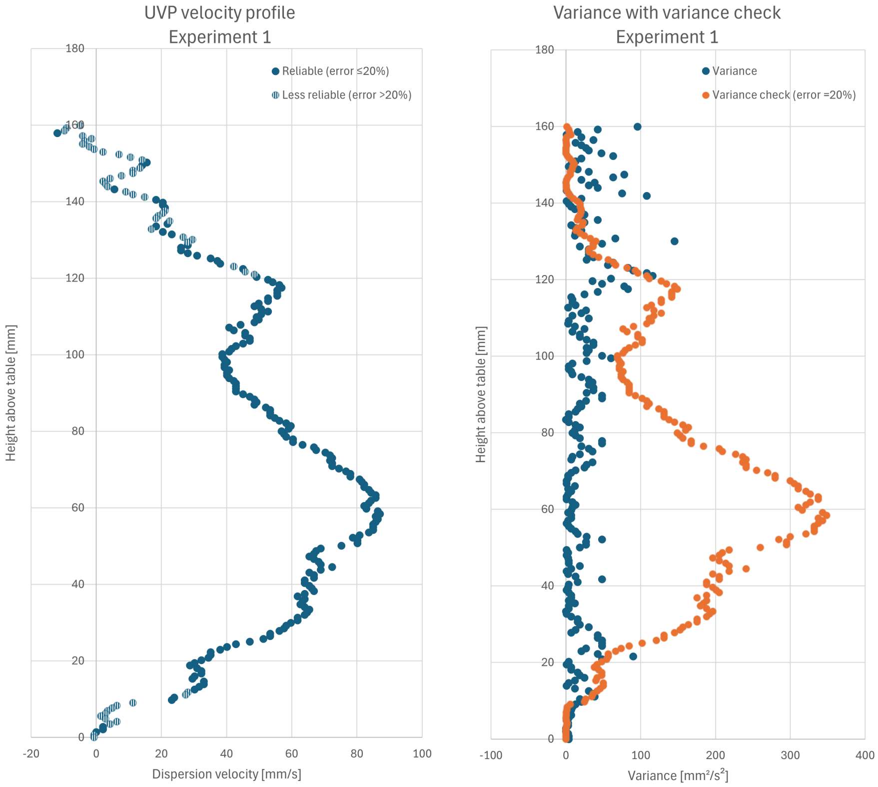

Figure C.1: Experiment 1 - Velocity profile with variance and variance check plot

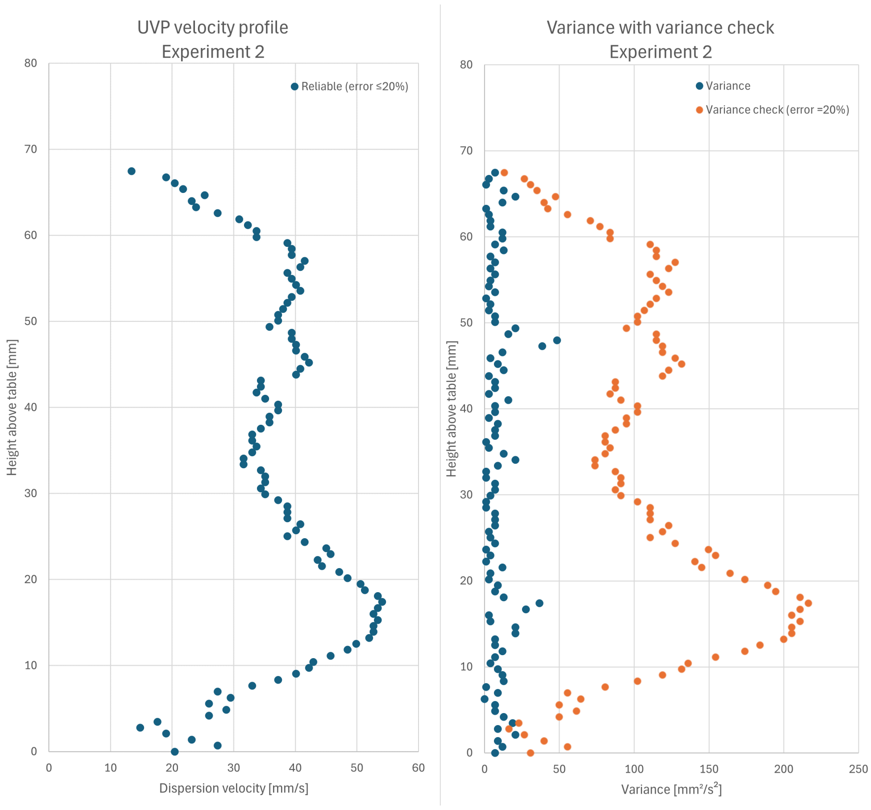

Figure C.2: Experiment 2 - Velocity profile with variance and variance check plot

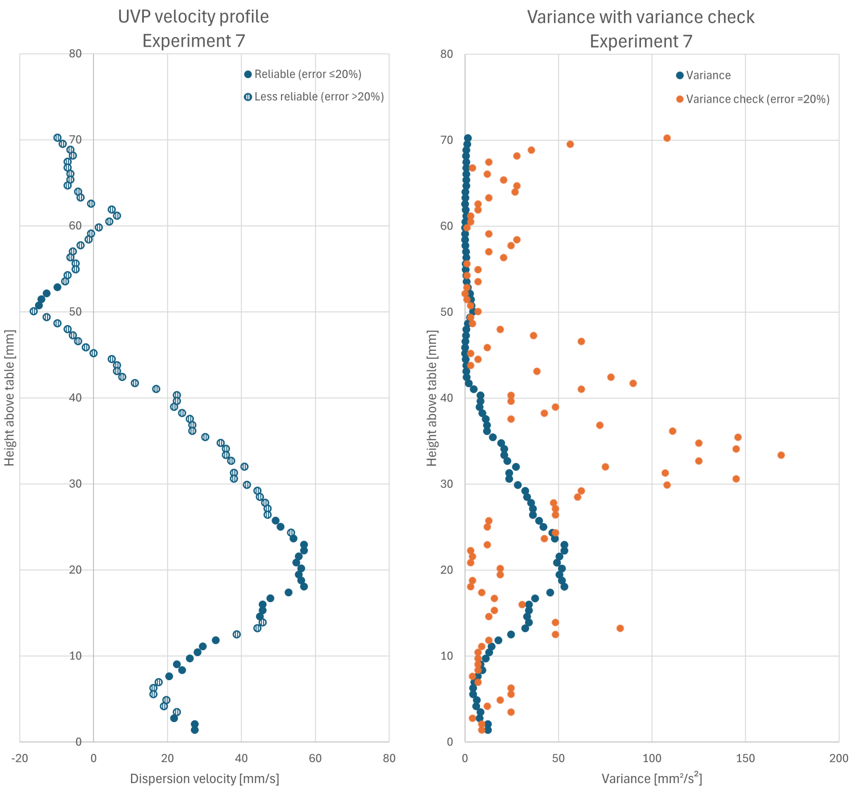

Figure C.3: Experiment 7 - Velocity profile with variance and variance check plot

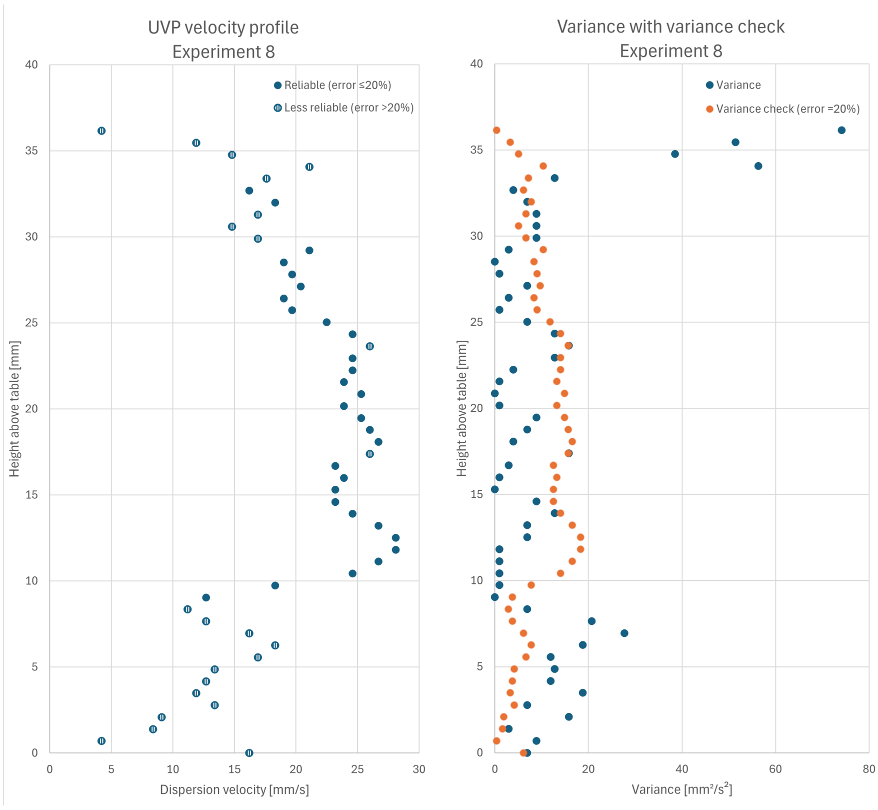

Figure C.4: Experiment 8 - Velocity profile with variance and variance check plot

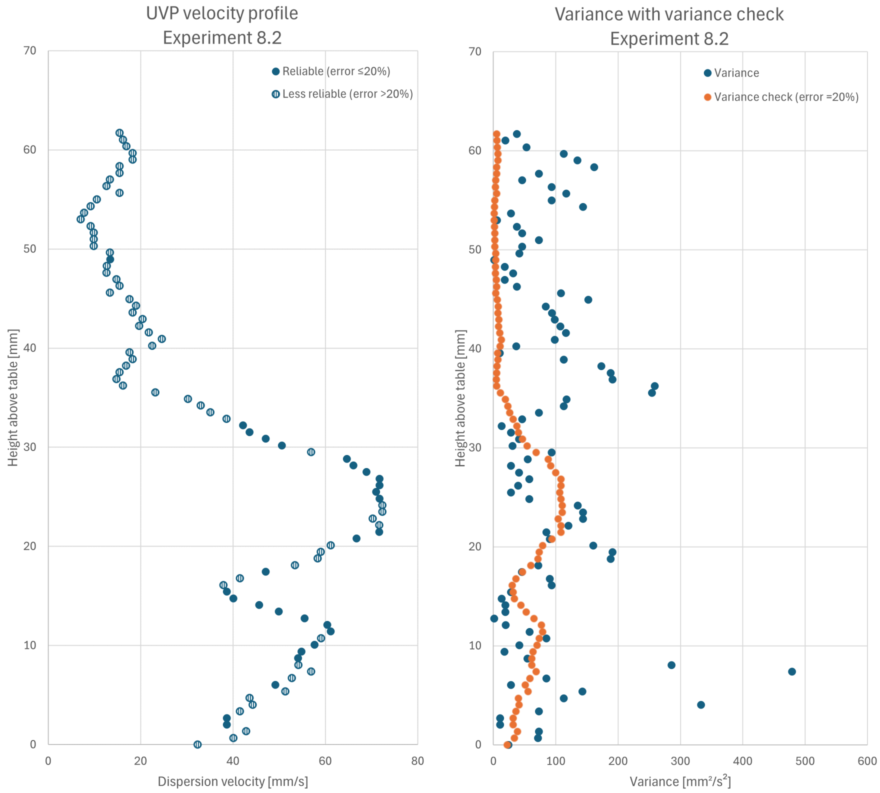

Figure C.5: Experiment 8.2 - Velocity profile with variance and variance check plot

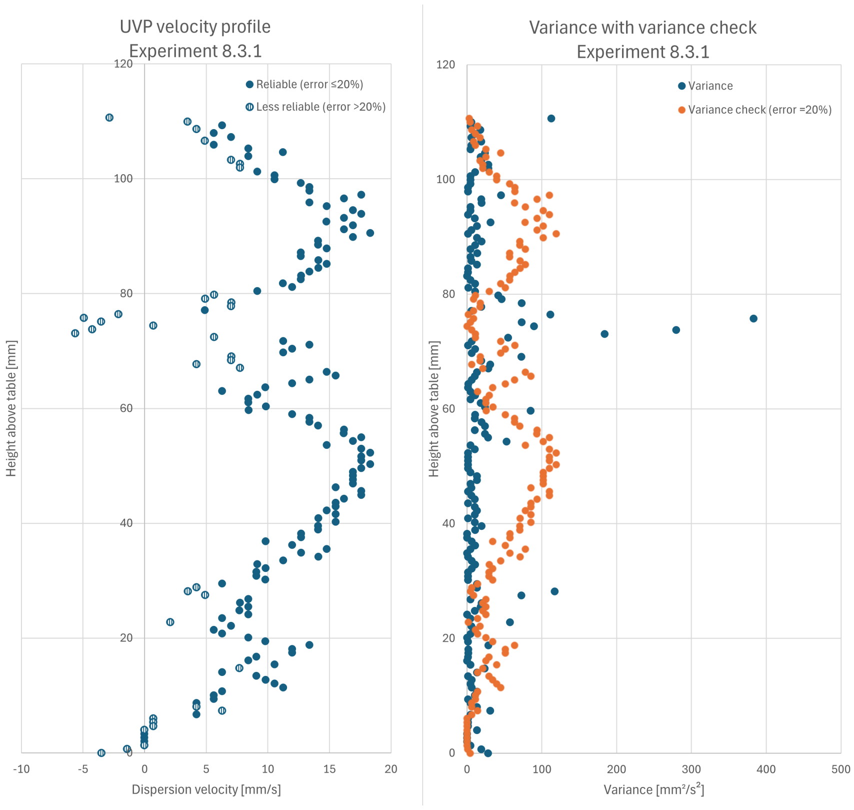

Figure C.6: Experiment 8.3.1 - Velocity profile with variance and variance check plot

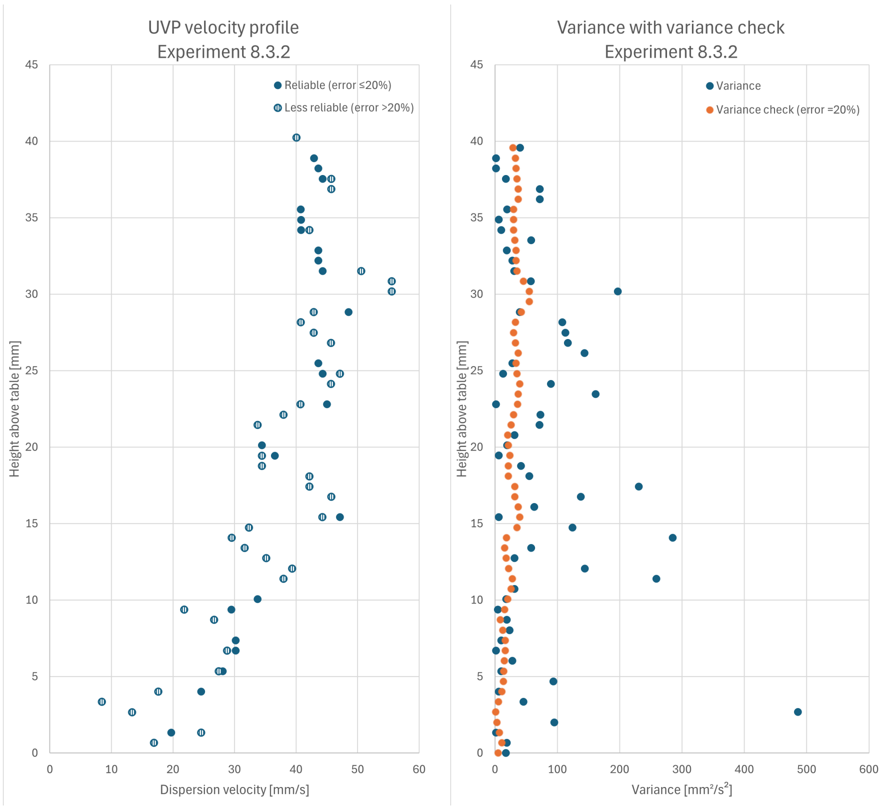

Figure C.7: Experiment 8.3.2 - Velocity profile with variance and variance check plot

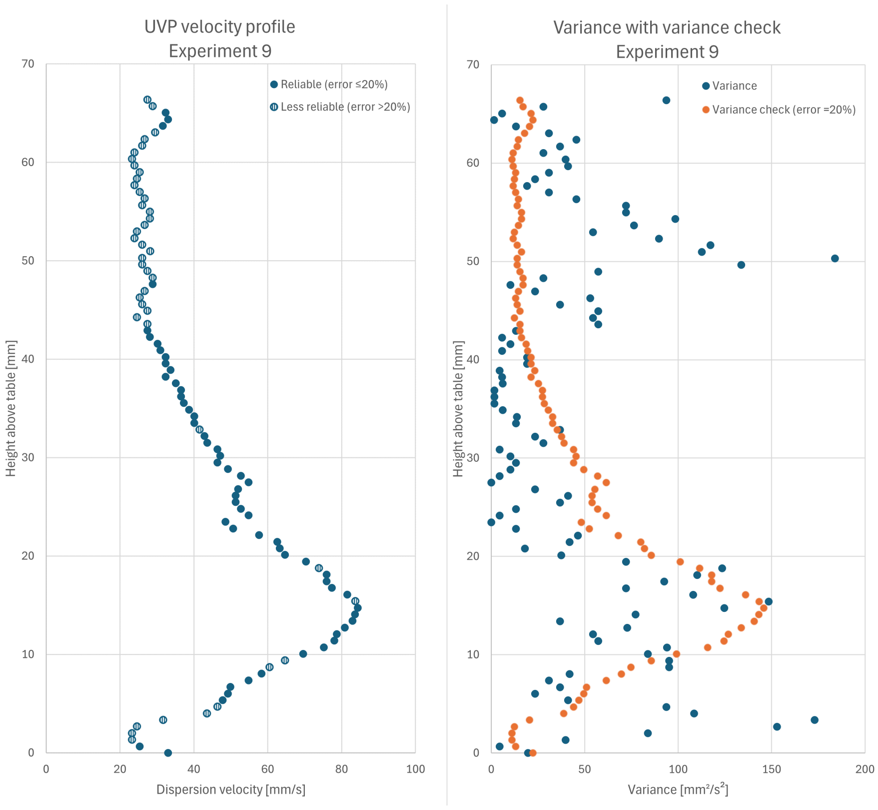

Figure C.8: Experiment 9 - Velocity profile with variance and variance check plot

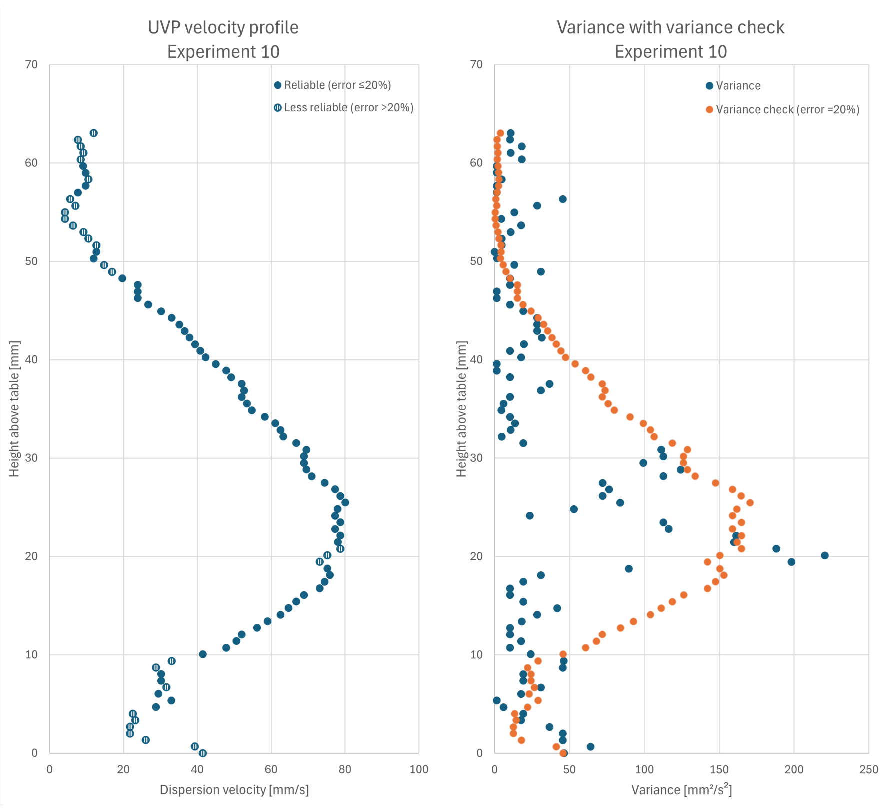

Figure C.9: Experiment 10 - Velocity profile with variance and variance check plot

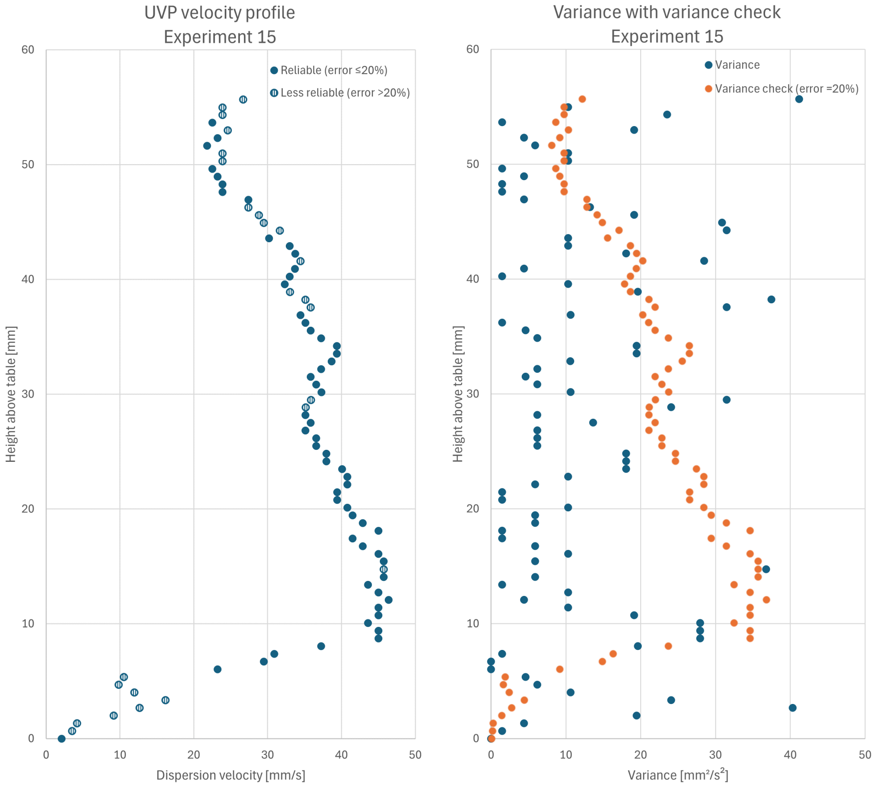

Figure C.10: Experiment 15 - Velocity profile with variance and variance check plot

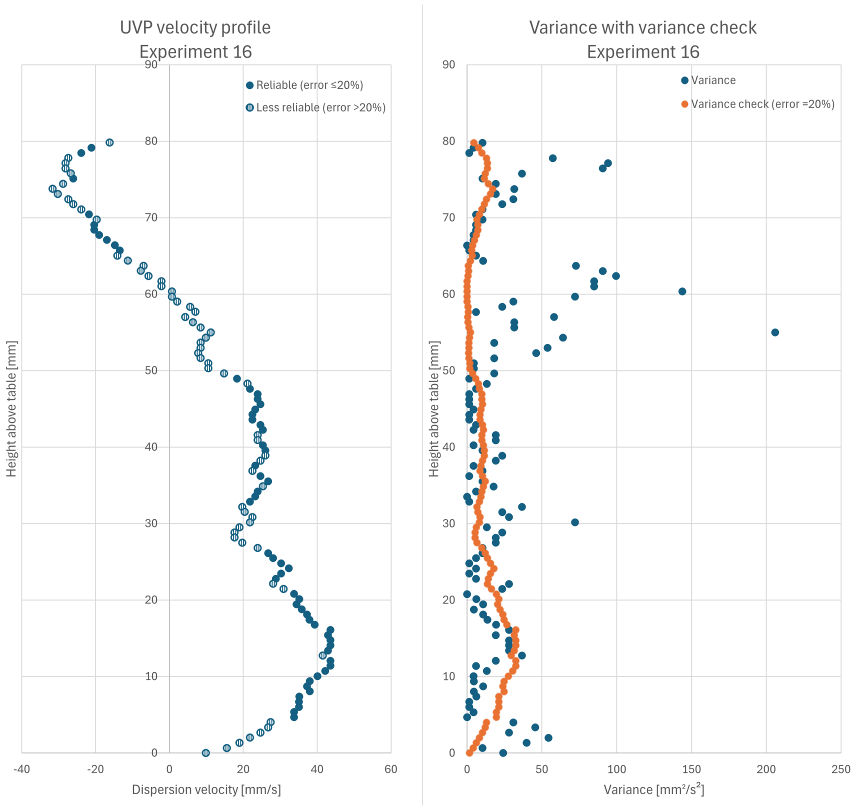

Figure C.11: Experiment 16 - Velocity profile with variance and variance check plot

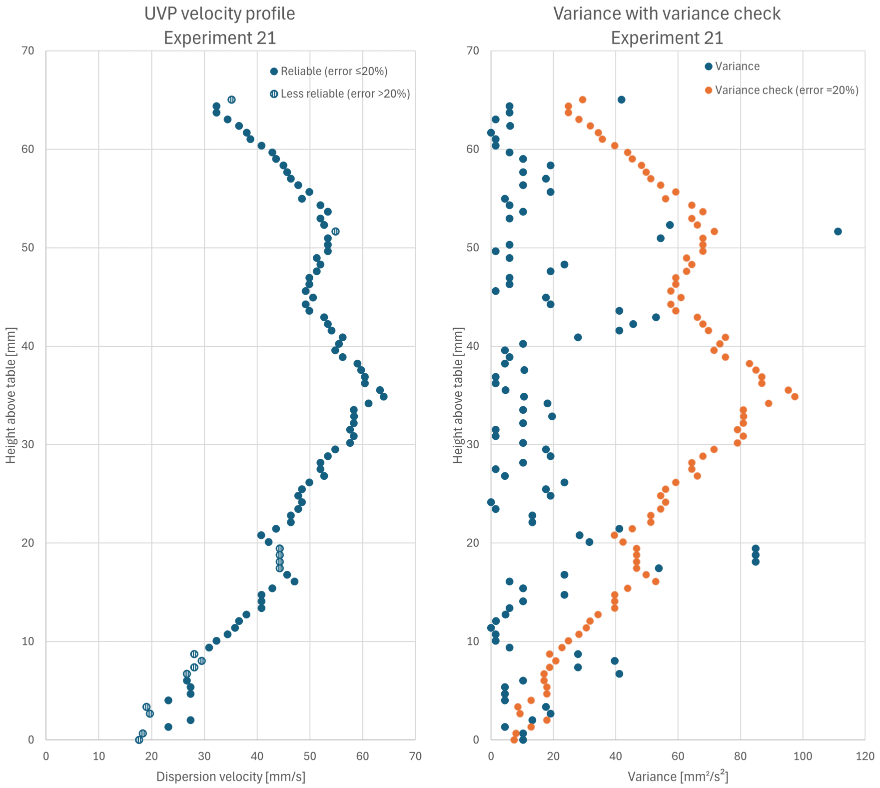

Figure C.12: Experiment 21 - Velocity profile with variance and variance check plot

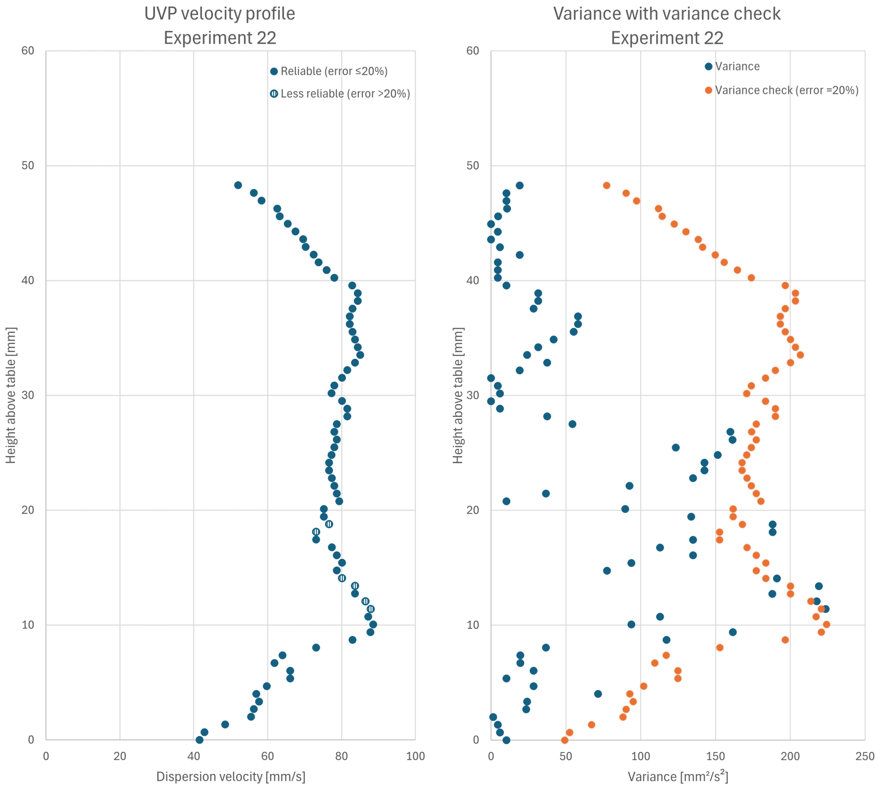

Figure C.13: Experiment 22 - Velocity profile with variance and variance check plot

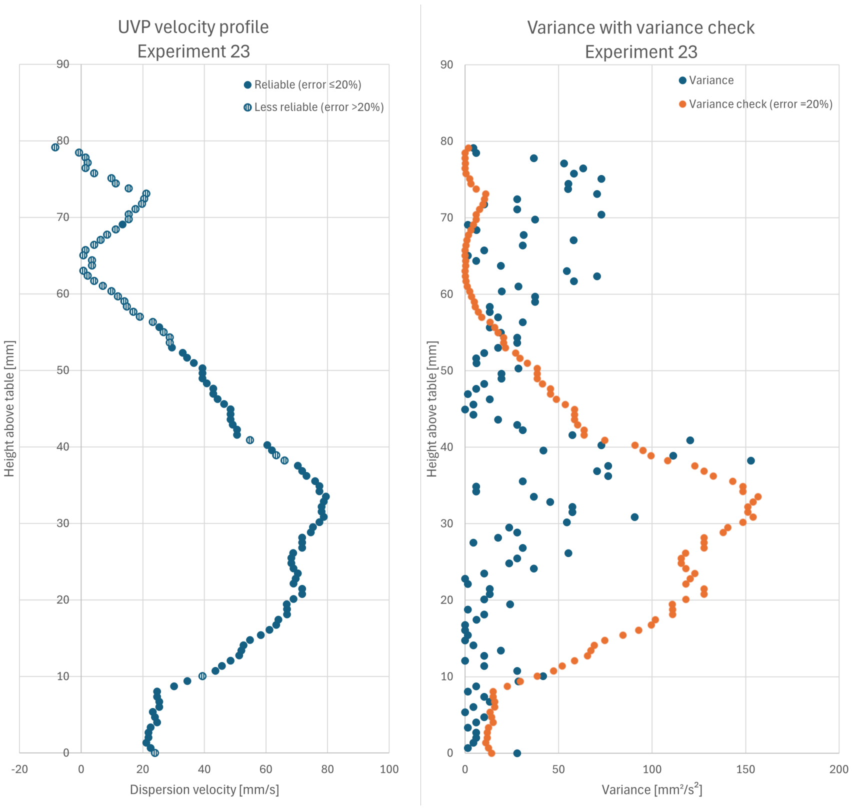

Figure C.14: Experiment 23 - Velocity profile with variance and variance check plot

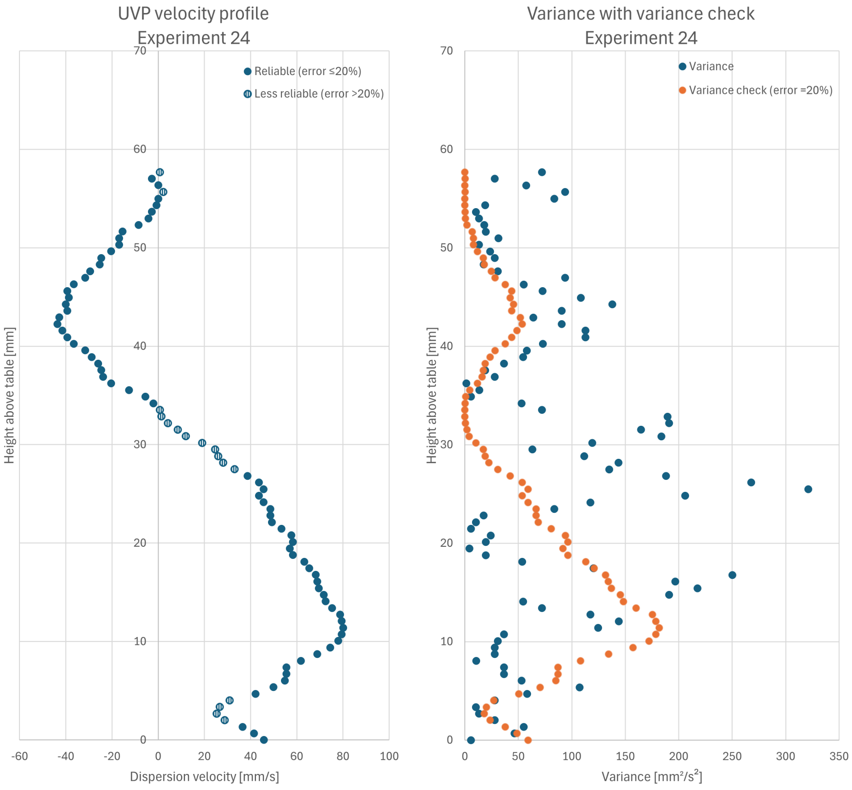

Figure C.15: Experiment 24 - Velocity profile with variance and variance check plot

D | Concentration Measurements

Table D.1: Concentration measurement results from the ADV and Niskin bottle sampling

Experiment	Aimed $[\frac{g}{L}]$	SNR	ADV $[\frac{g}{L}]$	Nisk.s. $[\frac{g}{L}]$	Deviation ADV	Deviation Nisk.s.
1	61.5	48.41	43.05	24.64	-30%	-60%
2	61.5	46.94	54.20	36.99	-12%	-40%
3	24.6	51.64	18.66	10.87	-24%	-56%
4	24.6	50.90	24.25	19.85	-1%	-19%
7	61.5	47.25	51.83	52.26	-16%	-15%
8	61.5	46.01	61.26	68.36	0%	11%
8.1	61.5	46.33	58.80	62.49	-4%	2%
8.2	61.5	44.35	73.78	61.94	20%	-1%
8.3.1	61.5	46.94	54.20	39.29	-12%	-36%
8.3.2	61.5	47.14	52.71	60.37	-14%	-2%
9	61.5	47.04	53.45	46.56	-13%	-24%
10	61.5	43.35	81.31	56.71	32%	-8%
15	61.5	46.86	54.77	40.34	-11%	-34%
16	61.5	46.18	59.95	47.81	-3%	-22%
21	61.5	46.32	58.85	39.99	-4%	-35%
22	61.5	46.65	56.35	57.25	-8%	-7%
23	61.5	45.47	65.31	46.70	6%	-24%
24	61.5	45.39	65.89	54.07	7%	-12%